UNIVERSITY OF STRATHCLYDE
Department of Physics

Design, fabrication and optimization of III-nitride micro light emitting diodes for optical communication

by

Xiangyu He

A thesis presented in fulfilment of the requirements for the degree of Doctor of Philosophy

February 2021

Declaration of Authorship

This thesis is the result of the author's original research. It has been composed by the author and has not been previously submitted for examination which has led to the award of a degree.

Signed: _____

Date: _____

Frontispiece

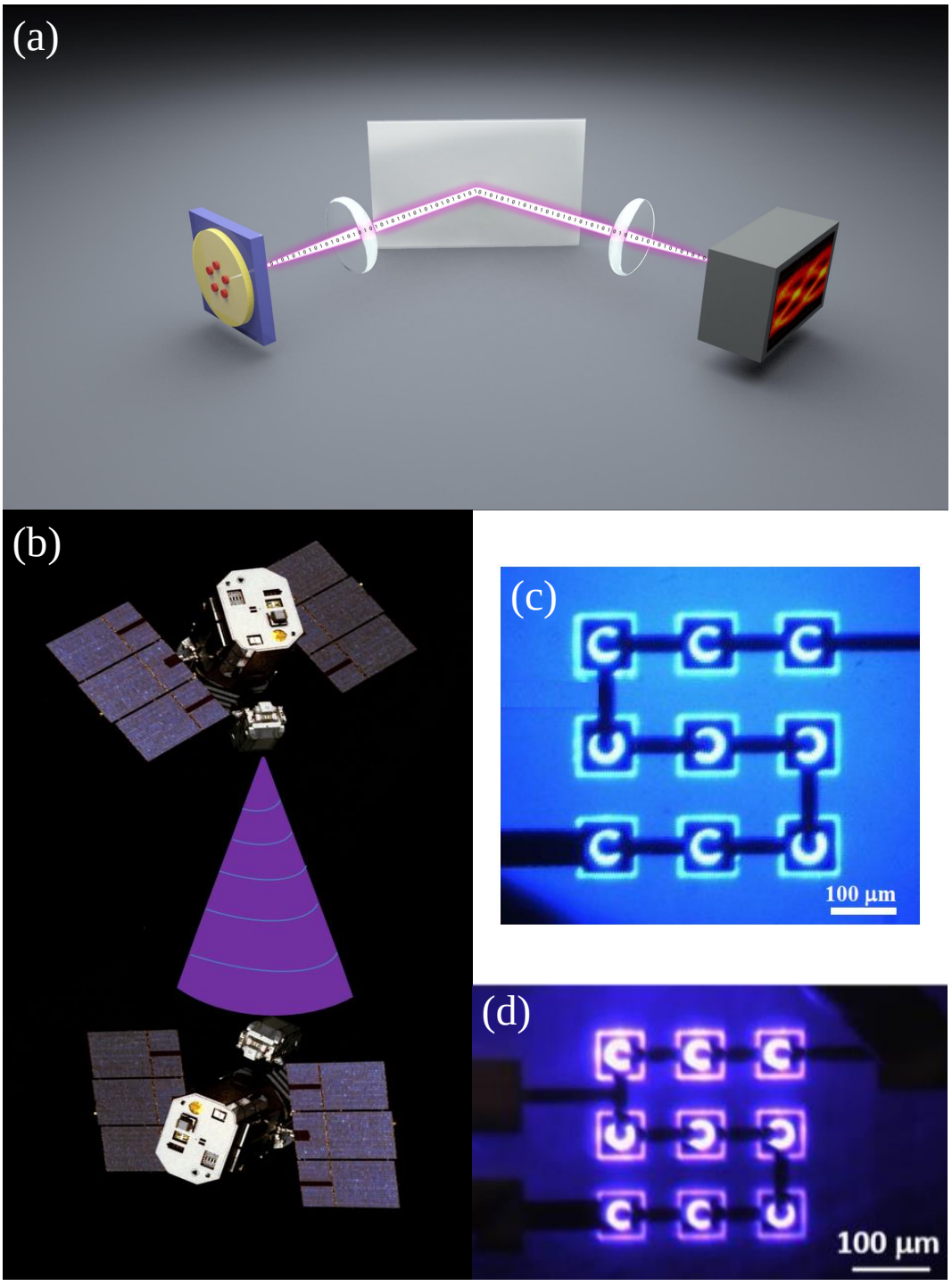

(a) Schematic of non-line-of-sight deep UC communication system; (b) schematic of free space communication system between satellites; (c) optical image of blue series-biased micro-structured light emitting diode; (d) optical image of blue series-biased micro-structured light emitting diode;

Abstract

The work presented in this thesis focuses on the development and optimization of III-nitride micro-structured light emitting diodes (μLEDs) for optical communications in free space. The main body of this work is divided into two parts. The first part is focused on the development and optimization of blue and violet series-biased μLEDs and blue μLEDs arrays with individually addressable n-electrodes for free space visible light communication (VLC). The second part demonstrates the development of deep ultraviolet (UV) μLED and its application in free space deep UV communication.

In this work, a new series-biased μLED is introduced, enabling high optical power without sacrificing too much 6-dB electrical modulation bandwidth. Over 10 Gbps data transmission rates are achieved using such μLEDs in long distance VLC. Furthermore, a new n-type metal-oxide-semiconductor (NMOS) driver controlled μLED array is introduced along with its VLC application. The design and fabrication process of this device are given in detail. The performances of the μLED array with an integrated NMOS driver are presented. Based on the novel III-nitride deep UV μLEDs developed in this work, a record deep UV data transmission rate of 3.36 Gbps is achieved at a bit error rate (BER) of 3.8×10^{-3} under orthogonal frequency division multiplexing (OFDM) modulation schemes.

Acknowledgements

This thesis would have not been completed without the help and advice of many people. First of all, I would like to thank my supervisor, Dr. Erdan Gu, for giving me this opportunity to pursue a PhD at the Institute of Photonics. He has spent lots of valuable time on my experiment design, papers and help with thesis writing. There is not possible I could overcome all the difficulties during my PhD studies without his support. I would thank Prof. Martin Dawson, Dr Ian Watson and Dr Nicolas Laurand for their guidance and encouragement throughout my studies.

Many thanks to Dr. Enyuan Xie for teaching me everything about microfabrication and micro-LEDs, and giving me many support in my PhD studies. I would like to thank Dr. Jonathan McKendry for his advices and help in many measurements. I am also grateful to Mr. Jim Sweeney for keeping the cleanroom working and help in some processes. I also want to thank Dr. Yunzhou Cheng and Dr. Jose Correia Carreira for their help for some measurements I could not do like SEM measurement.

I would like to thank all the colleagues for making a good place to work. I also would like to thank the colleagues at Prof. Harald Haas group from the University of Edinburgh, in particular Dr Mohamed Sufyan Islim, Dr. Rui Bian, and Dr. Chen Chen. They were always very patient in helping and explaining me for the OFDM measurements.

Finally, I would like to express my sincere appreciation to my parents and my girlfriend for their love, support and encouragement all the time. Special thanks to my girlfriend for her support and company in this tough year.

Contents

List of Figures

List of Tables

Abbreviations

AMP	High-power amplifier
APD	Avalanche photodiode
AWG	Arbitrary Waveform Generator
BER	Bit-Error-Ratio
CRI	Colour rendering index
CMOS	Complementary Metal-Oxide-Semiconductor
DAC	Digital-to-Analogue Converter
DC	Direct Current
EBL	Electron blocking layer
E-beam	Electronbeam evaporator
EL	Electroluminescence
EQE	External Quantum Efficiency
ESD	Electrostatic Discharge
FEC	Forward Error Correction
FFT	Fast Fourier Transform
FWHM	Full Width at Half Maximum
ICP	Inductively Coupled Plasma
IFFT	Inverse Fast Fourier Transform
IEEE	Institute of Electrical and Electronics Engineers
IQE	Internal Quantum Efficiency
IR	Infrared
ISI	Intersymbol interference

LED	Light Emitting Diode
LEE	light extraction efficiency
MOCVD	Metal Organic Chemical Vapour Deposition
M-QAM	M-ary Quadrature Amplitude Modulation
MQW	Multiple Quantum Well
NRZ	Non-return-to-zero
NLOS	Non-line-of-sight
NMOS	n-type Metal Oxide Semiconductor
OFDM	Orthogonal Frequency Division Multiplexing
OOK	On-Off Keying
PAM	Pulse amplitude modulation
PCB	Printed Circuit Board
PMOS	p-type Metal Oxide Semiconductor
PRBS	Pseudo-random bit sequence
PSS	Patterned Sapphire Substrate
QAM	Quadrature Amplitude Modulation
QCSE	Quantum Confined Stark Effect
QW	Quantum Well
RF	Radio Frequency
RIE	Reactive Ion Etching
SNR	Signal-to-Noise Ratio
UV	Ultraviolet
VLC	Visible Light Communication
WPE	Wall plug efficiency

To my family

Chapter 1

Introduction

This thesis focuses on the development and application of novel III-nitride micro-structured-light emitting diodes (μLEDs). This chapter gives a general introduction to light emitting diodes (LEDs), especially for those fabricated from III-nitride materials. A brief introduction of the concept of using LEDs for optical communication is described. The motivations of the work presented in the thesis are introduced as well in this chapter. In section 1.1, the historical development of LEDs and their application are summarized. In section 1.2, the basic working principles of LEDs are given, especially for the carrier recombination process in the LED structures. In section 1.3, the III-nitride materials and related growth processes are demonstrated, along with a brief introduction of the III-nitride LEDs. In section 1.4, the background of the LEDs based optical communication is introduced, including visible light communication and deep UV communication. Finally, an outline of this thesis is given in section 1.5.

1.1 Light emitting diodes and its applications

Electroluminescence was first invented by the British experimenter H. J. Round in 1907 [1]. He found that a yellow light was produced when a crystal-metal-point-contact structure fabricated from SiC was touched by a metal electrode. This luminescence phenomenon was explained and reported in 1928 [2]. The researchers proved the light emitted from the device is generated by the passage of an electric current or to an electric field instead of the black-body light emission resulting from heat glow (incandescence). This phenomenon was named electroluminescence. However, with the fast development of the theoretical understanding and semiconductor tools, the researchers shifted their attention and found the III-V compounds were the most suitable materials for modern LEDs in 1950. These novel compounds accelerated the development of LEDs with different emission wavelengths. In 1962, the first infrared (IR) (870-980 nm) LED and lasers based on GaAs were reported [3]. Holonyak and Bevacqua demonstrated the first commercial red LED based on GaAsP in the same year [4]. Moreover, the researchers found that the emission spectra of LEDs were able to extend from the red to green region by changing the relative composition of an alloy of GaAsP [5]. AT&T Bell Labs introduced the LEDs with green emission by using n-doped GaP shortly afterwards [6].

As mentioned above, the emission spectra of LEDs can only be extended from the red to the green region at the time. Thus, many works were concentrated on extending it to blue and ultraviolet (UV) wavelength regions in the late 1960s with SiC and III-nitride material. The blue LEDs based on SiC were commercialized in 1990 [5]. However, the best SiC LEDs with an emitting wavelength of 470 nm (blue) had electrical-to-optical power-conversion efficiency of only 0.03 %. This low value limited the application of blue SiC LEDs. The first GaN based blue metal-insulator-semiconductor diode was introduced by Pankove et al. in 1972 [7]. However, due to the low crystal quality and the inability to produce p-type doping

in GaN, the development of high quality GaN was not successful [8]. As a result, many researchers' work on GaN were virtually ceased at the time [9]. The recession of the development of GaN was ended in 1986. At the time, the crystal quality of a GaN film was significantly improved by the incorporation of an AIN nucleation layer at a low growth temperature before the deposition of the main GaN film [10]. In 1989, the first true p-type doping and p-type conductivity in GaN were demonstrated by using electron-beam irradiation to active Mg acceptors in GaN [11]. In 1994, it was shown that Mg dopants in Mg-doped GaN could also be activated by a high-temperature post-growth annealing [12]. These improvements opened the door to the development of high efficient III-nitride LEDs. A brief introduction of the III-nitride materials and related LEDs will be given in section 1.3.

In the development of high efficiency LEDs, there are two important parameters used to evaluate the performance of LEDs: internal and external quantum efficiency (IQE and EQE). The IQE (η_{int}) is defined as the ratio of the number of photons emitted from the active region per second to the number of electrons injected into LED per second, which can be expressed as [5]:

$$\eta_{int} = \frac{P_{int}/(hv)}{I/e} \tag{1.1}$$

where P_{int} is the optical power emitted from the active region, I is the injection current, h is Planck's constant, v is the emitted light frequency, and e is the elementary charge. In an ideal LED, all photons emitted by the active region will emit into free space. However, in a real LED, not all the photons emitted from the active region can escape from the semiconductor die. This can be caused by the reabsorbed in the substrate of the LED or metal contacts, and/or undergo total internal reflection. The EQE (η_{ext}) gives the ratio of the number of photons emitted into free space per second to the number of electrons injected into LED per second, which can be expressed as [5]:

$$\eta_{ext} = \frac{P/(h\nu)}{I/e} = \eta_{int} \times \eta_{extraction} \tag{1.2}$$

where $\eta_{extraction}$ is the light extraction efficiency (LEE) and P is the optical power emitted into free space. In turn, LEE is the ratio of the number of photons emitted into free space per second to the number of photons created from the active region per second. Figure 1.1 shows the EQE of different commercial nitride and phosphide LEDs. It is clear that the EQE decreases in the green spectral range, where the human eye is the most sensitive. This phenomenon is so-called the green gap.

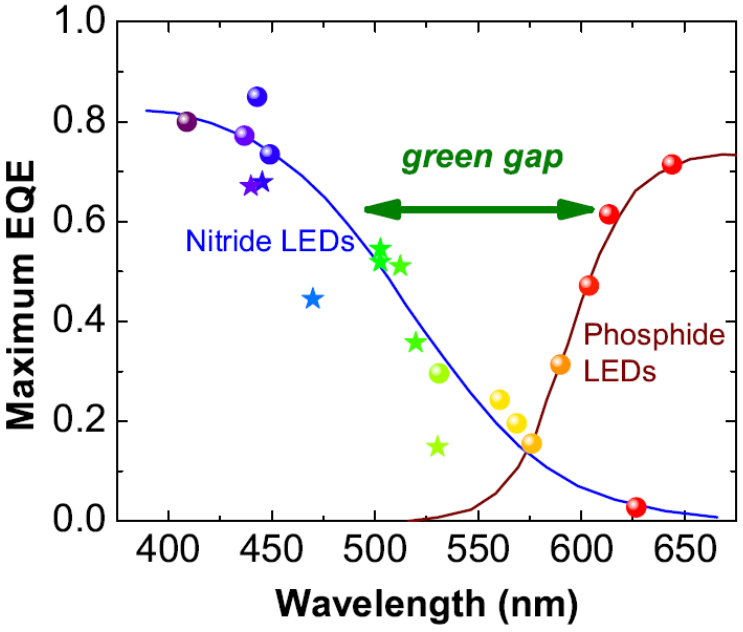

FIGURE 1.1: EQE versus emission wavelength for different commercial nitride and phosphide LEDs. After [13].

FIGURE 1.2: Typical applications of LEDs in our daily life: (a) LED bulbs for indoor illumination [14], (b) car headlights [15], and (c)LED monitor [16].

Nowadays, the applications of high efficiency LEDs can be found everywhere thanks to their low energy consumption, high efficiency, long lifetime, and mechanical robustness. Figure 1.2 demonstrates some typical applications of LEDs in our daily life, which are the LED lamps for indoor illumination, car headlights, and LED monitors. Hence, LEDs are of paramount importance, which was acknowledged in 2014 by the Nobel Prize Committee [17]. For indoor illumination applications, the LED lighting technology is able to generate white light up to 63 % and 90 % more than conventional lighting using fluorescent and incandescent lamps, respectively [18]. 203 lm/W white power LED performance was achieved at present time.[19]. Here, a lumen (lm) is the unit of luminous flux which represents the power as perceived by the human eye. The lm/W is the unit for the luminous efficacy, which is the conversion efficiency from electrical power to luminous flux. In future, if all conventional light sources were replaced by LEDs, around 1000 TW·h/year energy savings would be possible worldwide. This would be a saving of about $100 B/year, but also reduce the carbon emission by about 200 M tons [20].

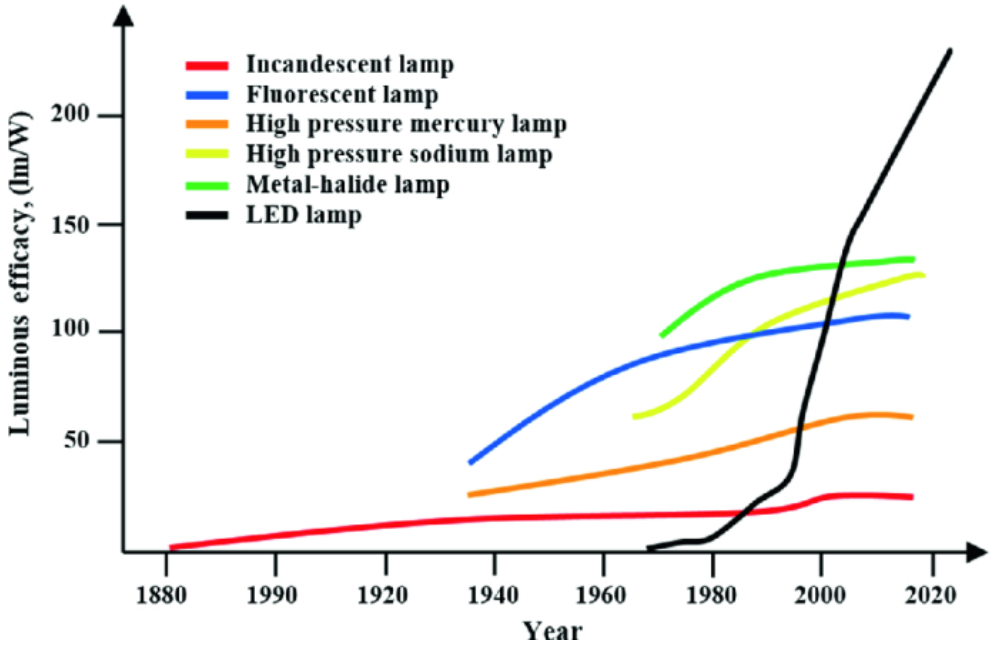

FIGURE 1.3: Time evolution of luminous efficacy performance of different lighting technologies. After [21].

Figure 1.3 presents the time of evolution of luminous efficacy performance of various lighting technologies. The early LED improvement was largely contributed by the increase of EQE due to the improved material systems and better chip designs for light extraction. Recently, the power of LEDs had a rapid improvement. One of the reasons for this improvement was the increase in EQE. Some researchers thought the more recent rapid power improvement for LEDs was due to the increases in the forward current density of LEDs, enabled by the sophisticated LED packaging technology. Figure 1.4 shows the cross section schematic of a typical LED package. The single chip size of the LED (InGaN semiconductor Flip Chip) is usually at between 300×300 μm^2 to a few mm^2. The LED die is mounted on a silicon sub-mount chip with Electrostatic Discharge (ESD) protection, and then sits on the top of a heatsink slug. The LED die is wire bonded to a metal frame and is easily electrically addressed by the outer connectors (cathode and anode leads). In order to maximizing the light output, the LEDs die is encapsulated with silicone and then covered with a plastic lens.

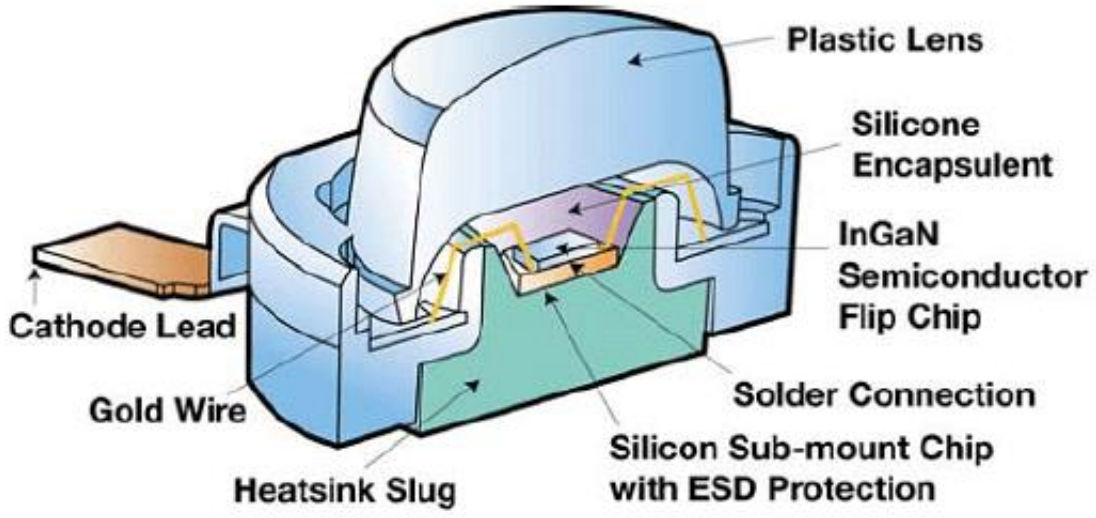

FIGURE 1.4: Schematic of a package high-power LED. After [22].

1.2 Operating principles of light emitting diodes

1.2.1 Introduction to semiconductors

According to the solid-state energy band theory, a semiconductor crystal has an energy band structure that has a valence band and a conduction band. The valence band and conduction band are separated by a forbidden energy region. This region between the valence band and conduction band is called a bandgap. There are two different types of free carriers, electrons, and holes. These free carriers are located at the conduction band and valence band separately. The electrons are at the minimum of the conduction band. The holes are at the maximum of the valence band. Photons are possibly released when these free carriers recombine. Based on their bandgap feature, semiconductors can be divided into two types i.e. direct and indirect bandgap semiconductors. The band structures of direct bandgap and indirect bandgap semiconductors is shown in figure 1.5. The figure also describes the electron transition processes from band to band that would lead to electron-hole recombination. The electron-hole recombination may cause photon

emission. A certain crystal momentum is used to characterize the energy state in the conduction band and the energy state in the valence band. Interactions among electrons and holes are required to satisfy the conservation of energy and crystal momentum. For direct bandgap semiconductors, the top of the valence fits in with the bottom of the conduction band so that there is no change of momentum. For indirect bandgap semiconductors, the top of the valence band occurs at a different value of crystal momentum from the bottom of the conduction band, so that there is a change of momentum and, thus, requires the assistance of a lattice vibration (phonon) to conserve momentum. Consequently, the probability of direct electron transitions is much higher than that of indirect electron transitions. Therefore, the direct bandgap semiconductors are more suitable for fabricating high efficiency LEDs than the indirect bandgap semiconductors [23]. The relationship between the bandgap and the wavelength of photons is given by:

$$E_g = E_C - E_V \approx \frac{hc}{\lambda} \tag{1.3}$$

where E_g is the value of the bandgap. E_C is the energy of the minimum of the conduction band. E_V is the energy of the maximum of the valence band. Moreover, λ is the wavelength of photons that were emitted from the semiconductor, h is Planck's constant, c is the speed of light in a vacuum [6].

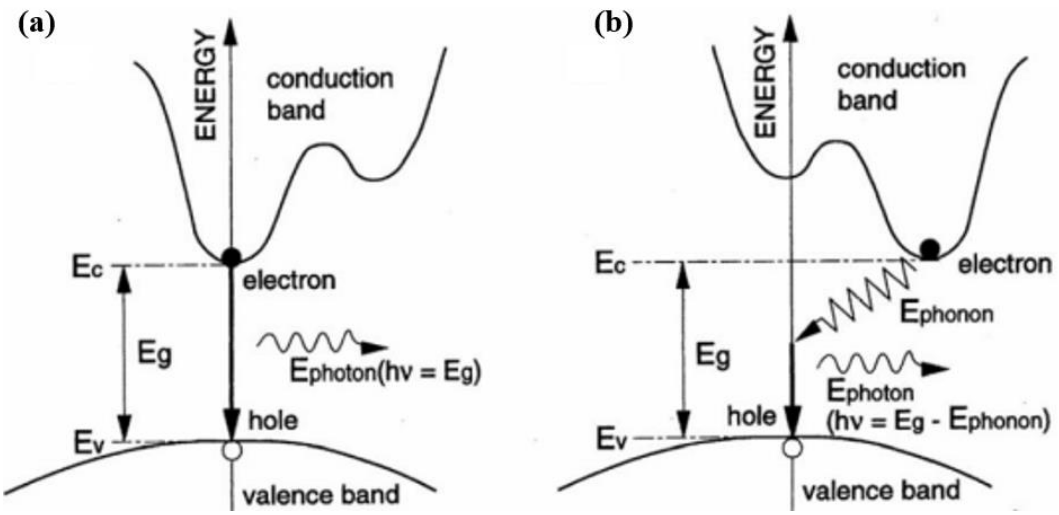

FIGURE 1.5: Band structure of (a) direct and (b) indirect bandgap semiconductors and related electron-hole recombination process. After [24].

For most of semiconductors, the environments for holes moving in the covalent bonds are similar since the structures of diamond and zincblende are similar. Thus, the valence bands of these semiconductors are qualitatively similar [25]. However, for AlGaN alloy, the valence band structure is unusual, which offers unique optical properties [26]. The transitions between the conduction band and topmost valence band of AlGaN determines the optical polarization of its luminescence. The conduction band and heavy hole band dominates the band transition when the topmost valence band is the heavy hole band. It leads to a transverse-electric (TE) dominant emission. However, as Al composition increased, the split-off hole band will move close to the conduction band, and cross over the heavy hole band. As results, the split-off hole band will become the topmost band, and the band transition will be dominated by the conduction band and split-off hole band. In turn, the TE dominated emission transfers to transverse-magnetic (TM) dominated emission. This optical polarization has a considerable impact on the performances of AlGaN based optical devices. For example, for AlGaN based edge

emitting laser diodes, TE polarization is desirable since TE polarized light cannot penetrate deeply into the smaller bandgap p-type region compared with TM polarized light [27].

1.2.2 Intrinsic and extrinsic semiconductors

Based on their properties, semiconductors can be divided into two different types, which are intrinsic and extrinsic semiconductors. A semiconductor that contains a very small amount of impurity atoms and no lattice defects in the crystal is so-called an intrinsic semiconductor. In thermal equilibrium (the steady-state condition at a given temperature without external excitations, there is no individual electron and hole currents flowing across the junctions), the probability that an electronic state with energy E can be occupied by an electron is given by the Fermi-Dirac distribution function:

$$F(E) = \frac{1}{1 + e^{(E-E_F)/kT}} \tag{1.4}$$

where k is the Boltzmann constant, T is the absolute temperature in degrees Kelvin, and E_F is the energy of the Fermi level. The Fermi level is the energy level which has one-half probability to be occupied by an electron. For the intrinsic semiconductors, if the density of states in the conduction and valence bands is the same, the Fermi level must be at the midgap in order to get equal concentrations of electrons and holes. The intrinsic semiconductors are neutrally charged, and their conductivity is relatively low since they have the same number of generated free electrons in the conduction band and free holes in the valence band under external excitation. In order to increase the conductivity, a doping process is introduced. The doping process intentionally induces some impurities into semiconductors. These impurities can be classified as donors and acceptors. Donors can produce free electrons in the conduction band. Acceptors can generate holes in the valence

band. Meanwhile, the doping process is suppressing the minority carrier concentration. The semiconductors doped with donors or acceptors are known as n-type or p-type semiconductors, respectively. For n-type semiconductors, the electrons are majority carriers, while the holes are minority carriers. The Fermi level of it moves closer to the bottom of the conduction band. Inversely, for p-type semiconductors, the holes are majority carriers while the electrons are minority carriers. The Fermi level of it moves closer to the top of the valence band. Furthermore, the Fermi level of an extrinsic semiconductor approaches the intrinsic Fermi level as the temperature increases, and becomes intrinsic when it reaches this level [25]. Figure 1.6 shows the Fermi level for Si as a function of temperature and impurity concentration. The basic structure of an LED is a p-n junction, which consists of p-type and n-type semiconductors [28]. The detailed introduction of the p-n junction will be given in the following subsection.

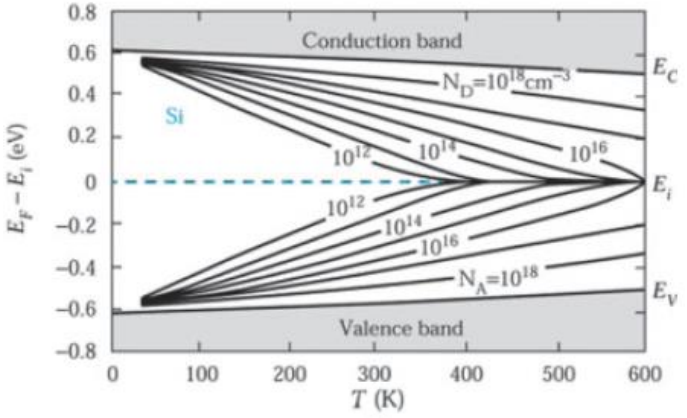

FIGURE 1.6: Fermi level of Si as a function of temperature and impurity concentration.. After [25].

1.2.3 p-n junction

Instead of placing two separate p-type and n-type semiconductors together, a p-n junction is typically created by epitaxial growth technology. This technology allows growing a layer of crystal doped with one type of dopant on top of a layer of crystal doped with another type of dopant. There are two types of p-n junctions,

which are homojunction and heterojunction. A p-n junction consisting of a single crystalline material is so-called p-n homojunction. It has the same bandgap across the whole junction. On the other hand, a p-n junction consisting of different crystalline materials is known as p-n heterojunction, which has different bandgaps across the whole junction. This subsection will give a brief introduction of p-n junction based on a p-n homojunction. The introduction of heterojunction will be given in subsection 1.2.4.

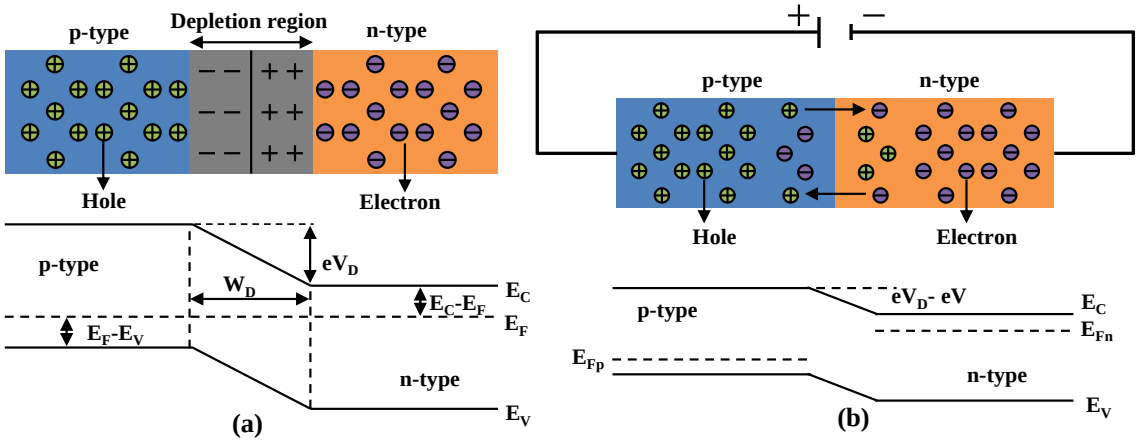

FIGURE 1.7: Schematic of a p-n junction and corresponding energy band diagram under (a) zero and (b) forward bias.

Figure 1.7 shows the simplified geometry of a p-n junction under different bias. As shown, there is a large density gradient for both carriers when the junction is under unbiased condition. Therefore, the electrons in the n-type region diffuse to the p-type region while the holes in the p-type region diffuse to the n-type region. As a result, there is a region which is depleted of any free carriers around the interface between n-type and p-type semiconductors. As figure 1.7 (a) shown, this region is known as the depletion region (W_D), where the free carriers are absent, and the only ionized dopant atoms are left. For example, there are positively charged donors in the n-type region and negatively charged acceptors in the p-type region. A potential across the depletion region created by these charges is known as the diffusion voltage (V_D). V_D is balancing the diffusion of carriers in a thermal equilibrium state. As figure 1.7 (a) shows, the free carriers must overcome

the barrier (eV_D) to reach the regions with the opposite conductivity type. Here e is the elementary charge. Meanwhile, the energy bands of n-type and p-type regions are moving due to the electrical field created by the space charge region in the p-n junction. As a result, the Fermi level moves down with the energy band on n-type region, while the Fermi level moves up with the energy band on p-type region. The energy bands of both regions stop moving when the Fermi levels on both regions are equal. Thus, the p-n junction is in thermal equilibrium.

Figure 1.7 (b) shows the state of p-n junction under the forward-bias condition. As shown, the external potential is mainly dropped across the depletion region when an external bias voltage is applied to the p-n junction. This is due to the high resistance of the depletion region. Therefore, the potential across the depletion region can be changed by applying an external bias voltage. As a result, the carriers will be injected into the depletion regions with the opposite conductivity type, and the current will increase. Meanwhile, as an external voltage is applied to the p-n junction, excess carriers are introduced to the p-n junction. It leads to that the electron and hole concentrations are higher than those in thermal equilibrium state. So, it is not meaningful to use Fermi level E_F in the non-thermal equilibrium state. However, it is still likely that the electron population and hole population are at equilibrium with the energy levels in the conduction band and valence band, respectively. Therefore, the quasi-Fermi levels E_{Fn} and E_{Fp} are introduced to express the electron and hole concentrations in nonequilibrium state [25]. As figure shown, the quasi-Fermi levels E_{Fn} and E_{Fp} under forward bias condition are separated. The different of both quasi-Fermi levels is equal to the external potential eV: E_{Fn} - $E_{Fp} = eV$.

The current-voltage ($I-V$) characteristic of a p-n junction diode with a cross-sectional area A is given by Shockley equation [5]:

$$I = eA\left(\sqrt{\frac{D_p}{\tau_p}}\frac{n_i^2}{N_D} + \sqrt{\frac{D_n}{\tau_n}}\frac{n_i^2}{N_A}\right)\left(e^{\frac{eV}{kT}} - 1\right) \tag{1.5}$$

where k is the Boltzmann constant, T is the temperature in Kelvin, e is the electron elementary charge, n_i is the intrinsic carrier concentration, N_D is the free electron concentration, N_A is the free hole concentration, $D_{n,p}$ are the electron and hole diffusion constants and $\tau_{n,p}$ is the electron and hole minority carrier lifetimes. Since the diode voltage is much large than the thermal voltage (kT/e) under forward bias conditions, the Equation 1.5 can be rewritten as:

$$I = eA\left(\sqrt{\frac{D_p}{\tau_p}}\frac{n_i^2}{N_D} + \sqrt{\frac{D_n}{\tau_n}}\frac{n_i^2}{N_A}\right)\left(e^{\frac{e(V-V_D)}{kT}}\right) \tag{1.6}$$

As Equation 1.6 shown, the current strongly increases when the applied voltage approaches the diffusion voltage. This turn-around point in the diode behaviour is called the threshold voltage (V_{th}), which is given by:

$$V_{th} = V_D = E_g/e \tag{1.7}$$

However, the Equation 1.5 is an ideal diode equation to expect theoretical $I-V$ characteristic of a p-n junction. For $I-V$ characteristic of a p-n junction which is measured experimentally, the equation is given by [5]:

$$I = eA\left(\sqrt{\frac{D_p}{\tau_p}}\frac{n_i^2}{N_D} + \sqrt{\frac{D_n}{\tau_n}}\frac{n_i^2}{N_A}\right)\left(e^{\frac{e(V-IR_s)}{n_{ideal}kT}}\right) \tag{1.8}$$

where R_s is the series resistance, and n_{ideal} is the ideality factor of the diode which changes with applied forward bias. The n_{ideal} is equal to 1 at high applied forward bias, which means that the ideal diffusion current dominates. Meanwhile, the n_{ideal} is equal to 2 at low applied forward bias. It means that the recombination current dominates. Moreover, the n_{ideal} is between 1 and 2 when these currents are comparable. When a forward bias which is higher than the forward bias at $n_{ideal} = 1$ is applied, the current would increase gradually with forward voltage. This is due to the effect of series resistance (R). The drop of IR becomes large

when the applied forward bias is higher than the one at $n_{ideal} = 1$. It leads to a reduction of the bias across the depletion region. In turn, the ideal diffusion current is reduced [25].

Other than $I - V$ characteristic, the capacitance of the p-n junction is also a important parameter since it relates to the modulation bandwidth characteristic. There are two kinds of capacitance in the p-n junction, which are depletion capacitance and diffusion capacitance [25]. The store and release of the electrons and hole in the depletion region are caused by the applied external voltage in the p-n junction. As a result, the density of space charges in the depletion region changes as the external voltage varies. This capacitance effect in the p-n junction is so called depletion capacitance (C_T), which is given by [29]:

$$C_T = 4A\sqrt{\frac{\epsilon_r \epsilon_0 q N_A N_D}{2(N_A + N_D)V_D}} \tag{1.9}$$

where A is the area of the p-n junction, ϵ_r is the relative dielectric constant, ϵ_0 is the absolute dielectric constant, q is the elementary charge, N_D is the donor concentration in n-type region, N_A is the acceptor concentration in p-type region, and V_D is the depletion potential. As equation 1.9 shows, the depletion capacitance is directly proportional to the area of the p-n junction. Meanwhile, it is inversely proportional to the square root of the depletion potential. When the p-n junction is under forward bias, there is another capacitance which named diffusion capacitance (C_D). The diffusion capacitance is caused by the transfer of minority carriers during the forward bias. The minority carriers diffuse from one side of the p-n junction to the other, which result in variation of charge with applied voltage, and then leads to capacitance. The diffusion capacitance is given by [29]:

$$C_D = [Aq^2 \frac{(n_{p0}L_n + p_{n0}L_p)}{k_0 T}] exp(\frac{qV}{k_0 T}) \tag{1.10}$$

where A is the area of the p-n junction, q is the elementary charge, n_{p0} is minority carrier concentration in n-type region, p_{n0} is the minority carrier concentration in p-type region, L_n is the length of the n-type region, L_p is the length of the p-type region, k is the Boltzmann constant, and T is the temperature in Kelvin. As equation 1.10 shows, the diffusion capacitance increases exponentially with increasing forward bias. Therefore, the diffusion capacitance dominates the capacitance of a p-n junction when the forward bias is high enough.

1.2.4 Double heterostructures and quantum wells

Figure 1.8 (a) shows the homojunction under a forward bias. As the figure shows, the minority carriers distribute over a long diffusion distance in the adjacent region before recombination. As a result, the density of minority carriers is relatively low in this region. Therefore, the radiative recombination (one of the electrons and hole recombination types) rate in the p-n homojunction is relatively low. In turn, homojunction is not suitable for a high intensity LED. The details of radiative and non-radiative recombinations will be given in subsection 1.2.5. Recently, all high performance LEDs employ p-n heterojunctions in order to achieve a high radiative recombination rate. A heterojunction is consisting of two different kinds of semiconductors. Thus, the structure of heterojunction devices has one small bandgap active region and one large bandgap barrier region. If the structure of heterojunction devices has two large bandgap barrier regions, it is called double heterostructure [5]. Figure 1.8 (b) shows the effect of heterojunction on carrier distribution. As the figure shows, the carriers are confined in the active region due to the heterostructure. As the heterostructures can confine the carriers to the active region, the diffusion of carriers can be avoided. Thus, the radiative recombination rate in the double heterostructure is significantly higher than the one in the homojunction. This leads to the improvement of the efficiency of LEDs.

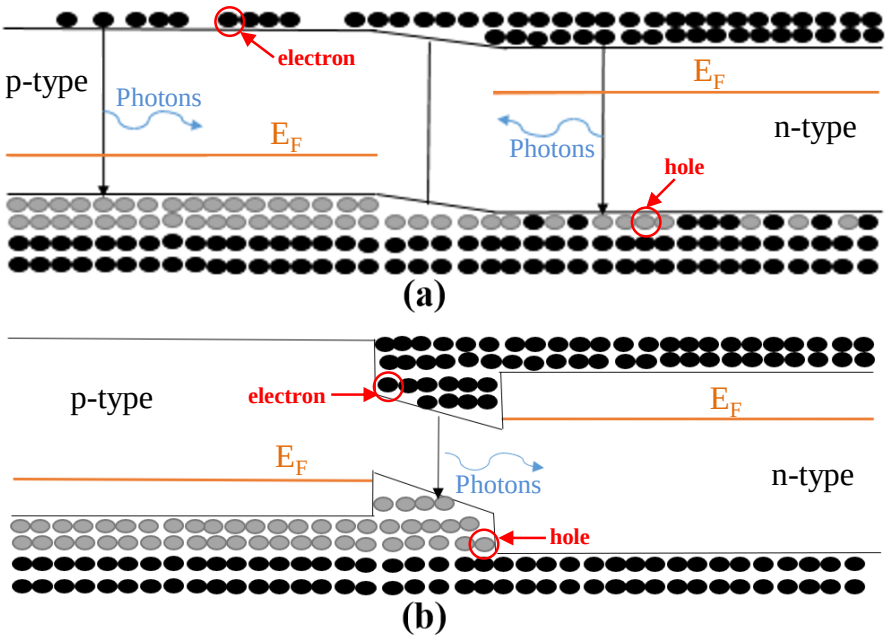

FIGURE 1.8: p-n (a) homojunction and (b) heterojunction under a forward bias. After [5].

Although the heterostructure can confine carriers to the active region, the carriers still can escape due to two reasons, i.e. the low barrier height of the active confinement interface and high temperature, which increases the carrier thermal energy. So, an electron blocking layer is needed. The electron blocking layers are used in many kinds of LEDs in order to reduce electron escape from the active region. The confinement-active interface of the p-type layer has an AlGaN electron blocking layer in order to create a barrier to current flow in the conduction band and valence band [5].

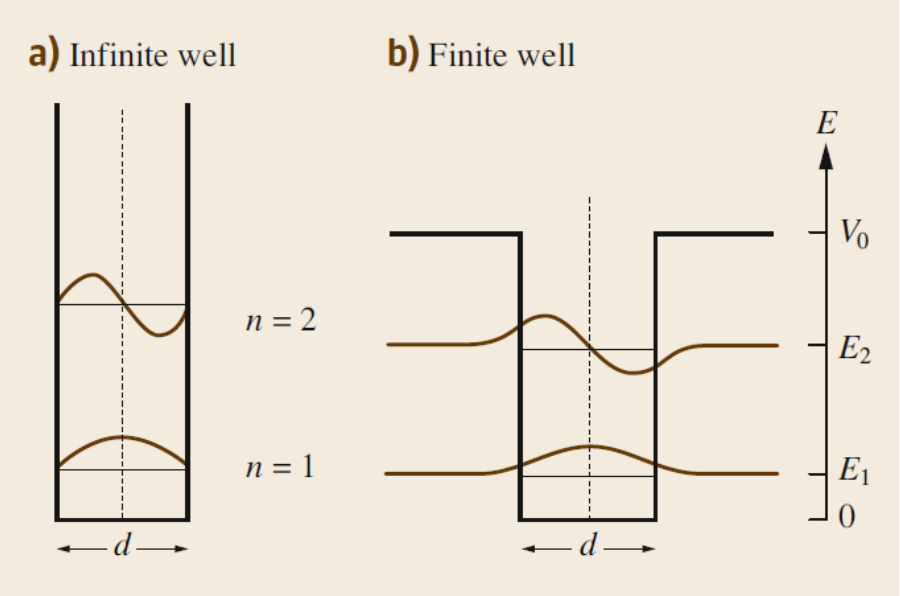

FIGURE 1.9: (a) a perfect quantum well (QW) with infinite barriers; (b) a finite well with barriers height of V_0. After [30].

Quantum size effects take place when the width of the active layer is relatively small and comparable to the de Broglie wavelength for thermal motion [31]. Assuming a thermal energy of $E = kT$:

$$\lambda_{dB} = \frac{h}{p} = \frac{h}{\sqrt{2m^*E}} = \frac{h}{\sqrt{2m^*kT}} \tag{1.11}$$

Where h is the Planck constant, p is the carrier momentum, k is the Boltzmann constant, T is the temperature in Kelvin, and m^* is the effective mass. An electron effective mass of GaN is $0.2m_0$ (m_0 is the electron mass). Thus, the related λ_{dB} is around 17 nm, which means the quantum effects can be observed when the active layer is thinner than 17 nm. This active layer is so called a quantum well. In the quantum well, the carriers are confined to one crystal direction where the carriers can only occupy quantized energy levels with discrete energy values. By solving the Schrödinger equation for the electrons and hole in the potential wells created by the band discontinuities, the electronic states of QWs can be understood [30]. Figure 1.9 shows the quantum wells with different barrier height under non-polarization

effect condition (non-polar system). The more details of polarization effect in III-nitride materials will be discussed in section 1.3.1. The infinite well model is the simplest approach can be used. Classically, any region where the potential exceeds the energy of the particle is forbidden. Thus, it is reasonable to assume the wavefunction must vanish in the region where the potential is infinite. Figure 1.9 (a) shows the schematic of infinite well mode. In this model, the Schrödinger equation in the well is given by [32]:

$$-\frac{\hbar^2}{2m_w^*}\frac{d^2\psi(z)}{dz^2} = E\psi(z) \tag{1.12}$$

Where $\hbar$ is the Dirac constant, m_w^* is the effective mass in the well, and z is the growth direction, E is the energy of the system, and $\psi(z)$ is wavefunction. There is no penetration into the barriers since the potential barriers are infinite. Thus, $\psi(z) = 0$ at the interface. If d is the width of the quantum well, the normalized wave function is given by:

$$\psi(z) = \sqrt{\frac{2}{d}} sink_n z \tag{1.13}$$

Where n is the quantum number (integer ≥ 1), and $k_n = n\pi/d$. Moreover, the energy E_n is given by [5]:

$$E_n = \frac{h^2 n^2}{8m_w^* d^2}; n = 1, 2, 3... \tag{1.14}$$

where h is the Planck constant, n is an integer, m_w^* is the carrier effective mass, and d is the width of QW. As mentioned before, the infinite well mode is very simplified. It provides an understanding of the general effects of quantum confinement. For example, the narrow wells have larger confinement energies, and lighter particles experience larger effects. However, even in quantum mechanics, a particle cannot be in a region of infinite potential. So, in order to be more realistic,

the finite well model is needed [30]. For the finite well mode, the Schrödinger equation in the well is not changed, while the one in the barrier regions is given by:

$$-\frac{\hbar^2}{2m_b^*}\frac{d^2\psi(z)}{dz^2} + V_0\psi(z) = E\psi(z) \tag{1.15}$$

Where V_0 is the potential barrier and m_b^* is the effective mass in the barrier. The wavefunction and particle flux $(1/m^*)d\psi/dz$ have to be continuous to the interface due to the boundary conditions. Therefore, it provides a series of even and odd parity solution which satisfy:

$$tan\frac{kd}{2} = \frac{m_w^*\kappa}{m_b^*k} \tag{1.16}$$

and

$$tan\frac{kd}{2} = -\frac{m_b^*k}{m_w^*\kappa} \tag{1.17}$$

Respectively. k is the wave vector in the well, which is given by:

$$\frac{\hbar^2k^2}{2m_w^*} = E_n \tag{1.18}$$

and κ is the exponential decay constant in the barrier, which is given by:

$$\frac{\hbar^2\kappa^2}{2m_b^*} = V_0 - E_n \tag{1.19}$$

As Figure 1.9 (b) shown, the wave functions of the finite well are approximately sinusoidal inside the well, but decay exponentially in the barriers. The eigenenergies of the finite well are smaller than those of the infinite well. It is caused by

the reduced confinement of the wave functions of the finite well which follows from their spreading into barriers.

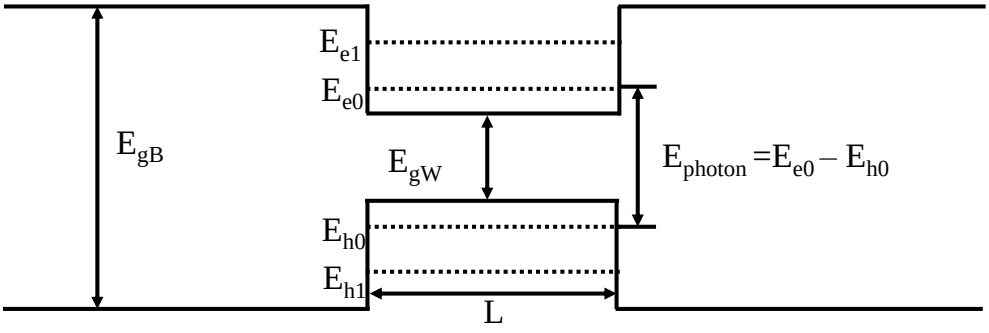

FIGURE 1.10: Band diagram of a QW. After [5].

Figure 1.10 shows the schematic band diagram of a QW structure. As shown, the energy of the emitted photon is determined by the separation of the QW energy levels. For example, the photon has an energy of $E_{e0} - E_{h0}$ in a transition between the QW ground states. Therefore, by optimizing the QW composition and width, the LED emission wavelength can be changed intentionally.

1.2.5 Radiative and non-radiative recombination processes

In a semiconductor, electrons and holes recombine either radiatively or non-radiatively. The radiative recombination is the highly preferable process in LEDs since it produces photons. On the other hand, the non-radiative recombination is the most unwanted process in LEDs since it generates heat. However, the non-radiative recombination process cannot be totally eliminated. Figure 1.11 (a) shows the radiative recombination in semiconductors. The density of electrons and holes are the key factors for the radiative recombination process. Figure 1.11 (b) and (c) show the two kinds of non-radiative recombination processes that are due to crystal defects and Auger recombination, respectively. In real semiconductors, crystal defects include dislocations, traps, contaminants, and etc. The energy levels in the bandgap of the semiconductor could be affected by those defects [23]. However, those energy levels could increase the efficiency of recombination if they are

close enough to the middle of the bandgap [6]. Regarding Auger non-radiative recombination, there are three carriers involved as shown in Figure 1.11(c). The synthetic energy ($\tilde{}Eg$) from the electron-hole recombination is delivered to another electron or hole. There are two ways that the synthetic energy can go. The first one is conduction band when the synthetic energy is affected by electrons. Another one is valence band when the synthetic energy is affected by holes.

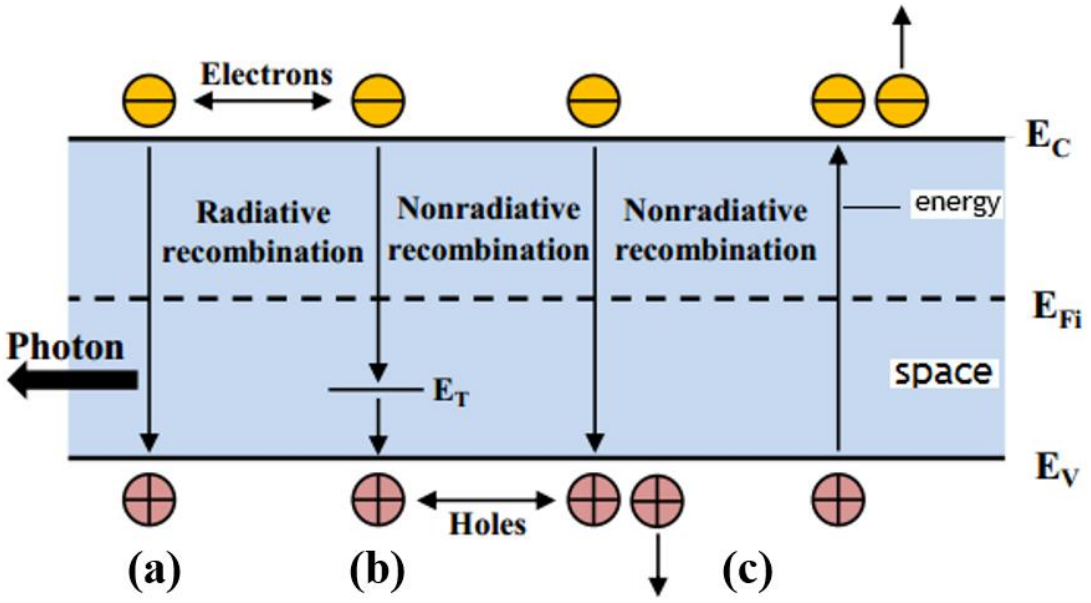

FIGURE 1.11: Diagram of the electron and hole recombination processes: (a) radiative recombination, (b) non-radiative recombination (crystal defect), and (c) non-radiative recombination (Auger recombination); E_{Fi} is the intrinsic Fermi level. E_T is the trap level. After [33].

1.3 III-nitride materials and III-nitride based light emitting diodes

1.3.1 III-nitride materials

III-nitride materials are important semiconductor materials as mentioned in section 1.1. III-nitride based LEDs can generate light efficiently across a wide spectrum, which enables many new applications and revolutionizing the whole lighting industry. The LEDs presented in this thesis with various emission wavelengths are fabricated from LED wafers based on III-nitride materials. Therefore, it is necessary to provide a basic background of III-nitride materials. This subsection will give a brief introduction to the III-nitride materials.

There are three basic binary alloys for III-nitride materials, which are AlN, GaN, and InN. The stable crystal of these materials has a hexagonal wurtzite structure under normal ambient conditions [23]. Under special conditions, these materials may change to the cubic zinc blende phase [34]. Moreover, the wurtzite structure can be maintained during the formation of ternary and quaternary alloys due to the III-nitrides' isomorphous nature. Therefore, the bandgap of these ternary and quaternary alloys can be tuned in a wide range by altering the relative amount of the individual materials. Figure 1.12 presents bandgap energy versus lattice constant of III-nitride materials at room temperature (RT). The bandgaps of these materials range are 0.65 eV for InN, 3.438 eV for GaN and 6.24 eV for AlN. These values have been used for decades. However, it must be mentioned that a new accurate bandgap of AIN is updated lately, which is 6.015 eV [35]. As shown in the figure, the emission wavelength of LEDs made from these III-nitride alloys spans from deep-UV to near-IR. Furthermore, the InGaN ternary alloys have direct bandgaps covering the whole visible spectrum. Thus, the InGaN ternary alloys are the desirable materials for visible light emitting applications. For example, most of high performance violet, blue, and green LEDs are based on InGaN ternary alloys.

However, the radiative efficiency is insufficiently high for the LEDs requiring high indium content, such as red emitting LEDs. It may be caused by the high lattice mismatch between InGaN and GaN. More details will be discussed later.

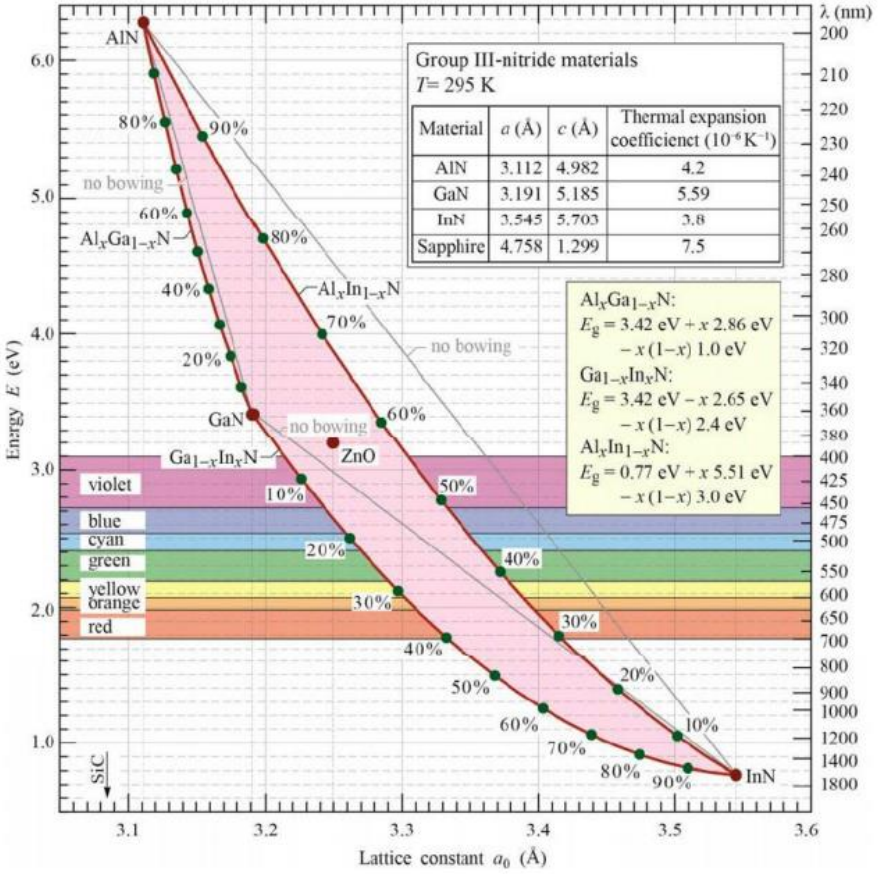

FIGURE 1.12: Bandgap energy versus lattice constant of III-nitride materials at RT. After [36].

All the LED devices reported in this work were fabricated from commercial III-nitride LED wafers with standard epitaxial structures. Figure 1.13 (a) shows a typical epitaxial structure of III-nitride LED wafers. The majority of commercial III-nitride LED wafers are grown epitaxially by metal-organic chemical vapor deposition (MOCVD). In order to form the desired crystal structures, the metal-organic vapors chemically react with each other and then be deposited on the surface of a substrate. However, the growth temperatures for III-nitride materials are relatively high (around 1000 °C) due to the strong chemical bond energy of

themselves. Thus, the choice of substrates is limited by their stability at high temperatures. Sapphire is the most common substrate for growing III-nitride LED wafers. There are some other substrates have also been demonstrated for the growth of III-nitride materials, such as SiC and Si [37, 38]. However, we will focus on III-nitride materials grown on the sapphire substrate in this section since all the LEDs reported in this thesis are fabricated from them. LED wafers are normally grown on *c*-plane (0001) sapphire substrate [39, 40]. However, the sapphire and GaN have a large lattice mismatch, which results in many dislocations in the LED wafers. As a result, the radiative efficiency of this semiconductor is reduced. The more details of dislocations in III-nitrides will be discussed later. In order to solve this issue, there are two necessary methodologies need to be applied. The first method is to introduce patterned sapphire substrates (PSS) [41]. By applying PSS for III-nitride material growth, the dislocation density can be reduced to about 10^7 cm^{-2} [42]. Meanwhile, the PSS can increase the LEE due to the inclined sidewalls, in turn, increase the EQE of III-nitride LEDs [43]. Figure 1.13 (b) shows the scanning electron microscopy micrograph of PSS. In order to further reduce the lattice mismatch between the sapphire and GaN, an AIN or GaN a buffer layer is normally deposited on the sapphire before growing the main epitaxial layers [5]. The strain caused by the lattice mismatch can be relaxed by this buffer layer, in turn, the crystal quality of main LED epitaxial layers can be improved. As a result, the dislocation density in III-nitride LED wafers is significantly reduced. As shown in figure 1.13 (a), an undoped n-type GaN layer is grown on the top of the buffer layer to improve the crystal quality of the above layers. After that, a Si-doped n-type GaN layer is grown as an n-type layer, followed by a GaN/InGaN MQW active region. The emission wavelength of LEDs is mainly dominated by the MQW active region. The desirable emitting wavelength of LEDs can be made by changing the composition of InN and GaN in the InGaN alloy, as discussed above. As mentioned in subsection 1.2.4, in order to prevent the overflow and escape of electrons from the MQW, an EBL is grown on the top of the MQW. The EBL is normally made of Mg-doped AlGaN, which offers a higher bandgap than

GaN. Finally, an Mg-doped GaN layer is grown as a p-type layer.

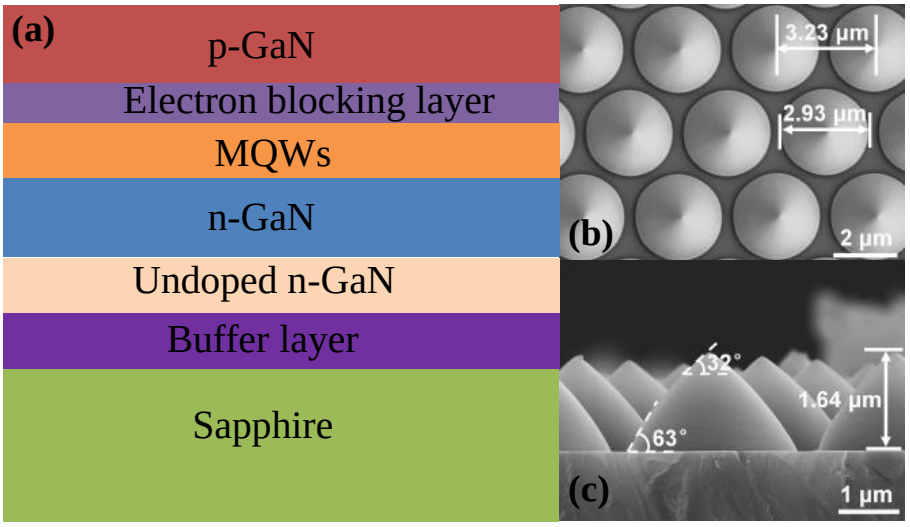

FIGURE 1.13: (a) typical epitaxial structure of III-nitride LED wafer; (b) scanning electron microscopy micrograph of PSS [44]; (c)cross-sectional transmission electron microscopy of PSS [44].

As mentioned above, dislocations will significantly reduce the radiative efficiency since they are non-radiative recombination centers. Therefore, the density of dislocations needs to be low for an III-nitride material to make LED devices with high radiative efficiency. Although the PSS and growth of a buffer layer can reduce the density of dislocation significantly, the typical value of the dislocation density in III-nitride materials grown on the *c*-plane sapphire is still high. However, the LEDs made from such III-nitride materials with high dislocation density show high radiative efficiency. The reasons for this phenomenon are still open to debate. One possible explanation is that the electronic states of the dislocation are outside the bandgap of III-nitride materials instead of inside the forbidden gap (Figure 1.14 (a)). Therefore, non-radiative recombination centers do not effect these energy levels. Another possible explanation is compositional fluctuations. Local potential minima are caused by the compositional fluctuations, which in turn can confine the carriers as a function of an inhomogeneous bandgap. Figure 1.14 (b) shows the carrier confinement resulting from compositional fluctuations. Furthermore, the inhomogeneous bandgap can result in a band-filling effect when

III-nitride LEDs are operating at different currents. As a result, the injected carriers fill the localized potential minima of the QWs before distributing in higher energy states. In other words, the emission wavelength of these LEDs keeps blue-shifting accompanied by a broadening of the full width at half maximum (FWHM) of their emission spectrum.

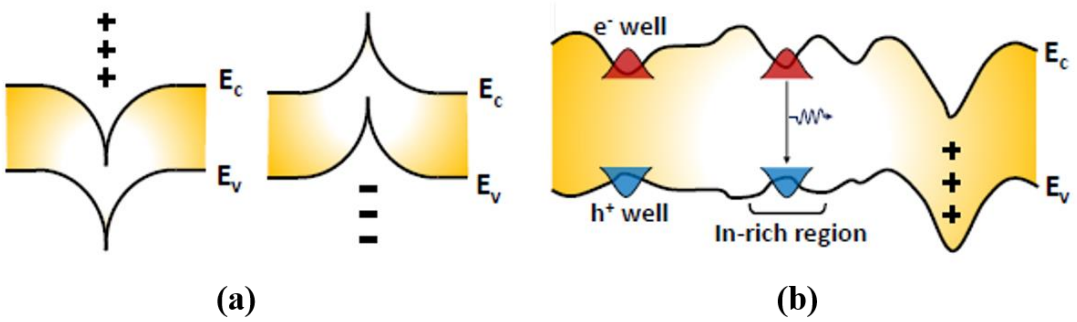

FIGURE 1.14: Band diagram of dislocations: (a) donor states in conduction band and acceptor sates in the valence band, (b) carrier confinement caused by compositional fluctuation. After [5].

Apart from good crystalline quality, the realization of efficient light emitters also depends on the n-type and p-type doping in III-nitride materials. Undoped GaN is always n-type with an electron concentration around 10^{16} cm^{-3}. Such high n-type electron concentration is contributed by the high density of N vacancies and Si and/or oxygen impurities in the GaN layer. These N vacancies and impurities act as shallow donors, which results in the n-type doped GaN layer [45]. The n-type doping in the GaN layer can be intentionally controlled by introducing Si dopants [46]. As mentioned above, MOCVD is the most common tool for the growth of high-quality III-nitride materials. The composition, thickness, and doping of the epitaxial films can be easily controlled by this technique. Therefore, the dopants can be introduced during the growth by adjusting the gas flow rate [45–47]. SiH_4 and Si_2H_6 are the most popular Si doping sources in MOCVD growth [48]. However, it is relatively hard to achieve efficient p-doping in III-nitride materials. The most commonly used acceptor in GaN is Mg. Mg can substitute the Ga atom to form a substitutional acceptor in GaN materials. However, there

are insufficient holes produced by Mg acceptors in the GaN materials due to the Mg being compensated by N vacancies or passivated with H atoms. During the MOCVD growth, an Mg-H complex is formed, which can chemically deactivate the p-type doping. As a result, the acceptors in the Mg-doped GaN layer are not electrically active. In order to solve this problem, a high temperature post-growth thermal annealing process is introduced [49]. The temperatures of this thermal annealing process are normally higher than 600 °C. To prevent additional chemical reaction during the process, an N_2 ambient is required. In the thermal annealing process, the bone of the Mg-H complex is broken, and the H atoms are driven out of GaN. Therefore, thermal annealing is the preferred method to activate the Mg acceptors. However, due to the high activation energy of Mg acceptors (170 meV), the hole concentration of a p-type GaN layer is still relatively low (10^{17} cm^{-3}) [50]. Thus, the percentage of ionized acceptors is relatively small.

As mentioned before, all the III-nitride LED wafers used in this work are grown on *c*-plane sapphire substrates. Therefore, all of them have a hexagonal wurtzite crystal structure. In turn, they are strongly polarized along the *c*-axis due to the non-centrosymmetric nature of the wurtzite structure. The polarization charges are formed and located at each of the two surfaces of a layer, which creates an internal electric field in the wafers. As a result, the optical and electrical properties of these wafers are influenced significantly [5]. There are two types of polarization effects, which are spontaneous polarization effect and piezoelectric polarization effect. Both polarization effects lead to a separate distribution in the positive and negative polarization charges. However, the directions of their internal fields depend on different conditions.

The spontaneous polarization effect is an intrinsic property of the material, and caused by the asymmetry of the atomic bonding in the equilibrium wurtzite crystal structure. Therefore, the growth orientation of the materials is the only factor that determines the direction of the resultant internal electric field (E_{sp}). Figure 1.15 (a) shows the distribution of spontaneous polarization charges and

the direction of the resultant E_{sp} in a GaN film grown on the c-plane sapphire substrate.

The piezoelectric polarization effect is caused by the tensile or compressive strain applied to the material. Tensile strain in III-nitride materials occurs when a material with a smaller lattice constant is grown on top of the material with a larger lattice constant. For example, an AlN layer grows on a relaxed GaN buffer layer. The small lattice constant of AlN leads to a tensile strain on the AlN layer. In contrast, compressive strain in III-nitride material occurs when a material with a larger lattice constant is grown on top of a material with a smaller lattice constant. For example, an InN layer is grown on a relaxed GaN buffer layer. The larger lattice constant of InN leads to a compressive strain on the InN layer. Therefore, the distribution of spontaneous polarization charges and the direction of the resultant E_{pz} are determined by both growth orientation and the strain type. The Figure 1.15 (b) and (c) show the resultant piezoelectric polarization effects for both strains.

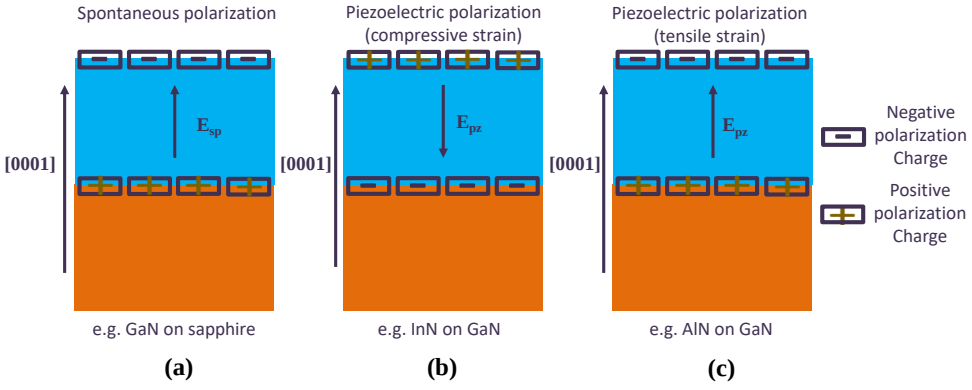

FIGURE 1.15: Schematic of surface charges and direction of the electric field (a) the spontaneous polarization effect, (b) the piezoelectric polarization effect under compressive, and (c) the piezoelectric polarization effect under tensile strain in III-nitride materials. After [33].

The spontaneous polarization effect is relatively weak in III-nitride LED materials. However, the strain-induced piezoelectric polarization effect needs to be considered due to the larger lattice mismatch between GaN and the ternary alloy

materials such as InGaN and AlGaN. Generally, a LED wafer contains a multiple QW (MQW) active region, which consists of at least two different III-nitride materials. The lattice mismatch between these materials would lead to the strong piezoelectric polarization effect. In turn, a larger E_{pz} is occurred in the MQW active region. As a result, the energy band of QW is tilted as Figure 1.16 shown. This behaviour reduces the effective bandgap energy by the amount of $eE_{pz}L_{QW}$. Moreover, this electric field tilts the potential and distorts the wavefuctions as the electrons tend to move to the anode and the holes tend to move to the cathode [30]. It leads to a spatial separation of the electrons and holes to the opposite sides of a QW. Consequently, the efficiency of carrier radiative recombination process is reduced, and a broadening of the Full Width Half Maximum (FWHM) of the emission spectrum can be observed. This phenomenon is referred to as the quantum-confined Stark effect (QCSE) [51].

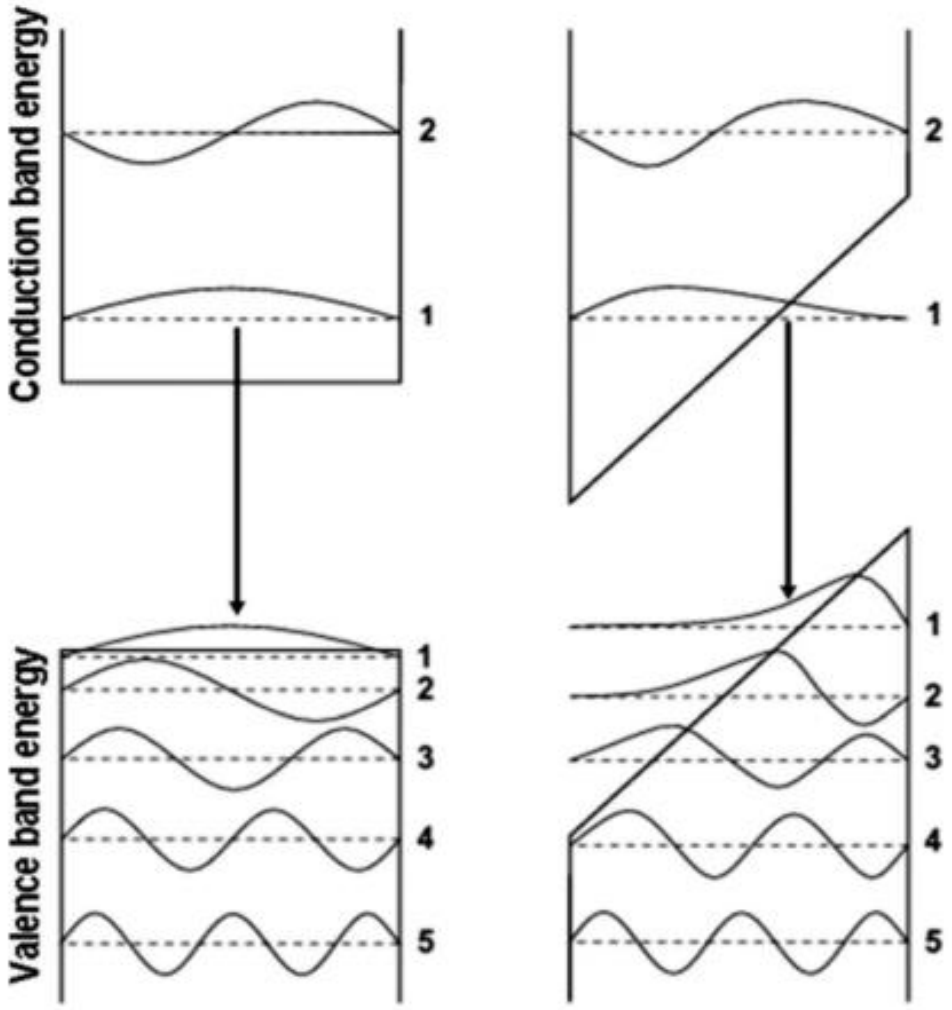

FIGURE 1.16: Electronic band structure of a quantum well structure without QCSE (left) and with QCSE (right). After [51].

As the indium content increases, the lattice mismatch between InGaN and GaN becomes larger. Therefore, in the InGaN QW emitting long wavelength light (yellow to red), the E_{pz} is increased. In turn, low efficiency of yellow to red InGaN LEDs could be expected. Meanwhile this E_{pz} behaviour is also considered as a possible reason for the efficiency droop observed for III-nitride LEDs. Moreover, the polarization charges can be compensated by the injected carriers, when III-nitride LEDs are operating under electrical condition. It leads to a screened E_{pz}, and a flattened energy band. As a result, the emission wavelength of the LEDs is blue-shift and the FWHM of it is narrowing.

There are many ways to suppress or eliminate the influence of the polarization effect in III-nitride materials. One of the common way is to reduce the thickness of QWs to minimize the polarization effect in the QWs, so that the electron and hole separation decreased [5]. The polarization effect in III-nitride materials can be also minimized or removed by the growth of semipolar and nonpolar III-nitride LED structures [52]. Furthermore, the piezoelectric polarization effect can be reduced by introducing the strain relaxation process. It has been proven that the micro-/nano-scale structures can partly or fully relax the strain cased by lattice mismatch between different III-nitride materials [53, 54].

1.3.2 III-nitride light emitting diodes

The first efficient blue LED using III-nitride materials was demonstrated in 1993 by Nakamura et all [55]. Figure 1.17 shows the close-up images of a bare and packaged blue GaN LED. As mentioned in subsection 1.3.1, most III-nitride LED wafers are grown on the sapphire substrate which is electrically insulating. Thus, the n-type and p-type ohmic contacts of the LEDs are generally deposited on layer top sides for operating purposes. Consequently, the n-type layer on the LED wafer needs to be exposed, in turn, part of the LED wafer needs to be etched away. The details of the etching process will be introduced in chapter 2. There are two common configurations of III-nitride LEDs, which are top emitting and flip chip configurations. The top emitting configuration is the most straightforward LED configuration. For such configuration, the light is directly extracted from the top of the p-type material. However, a p-type ohmic contact layer needs to be deposited on the p-type material surface. This layer functions as a current spreading layer which enables a uniform current injection and a low contact resistance for the device operation. Furthermore, for wire bonding purpose, a thick metal pad needs to be deposited on the top of the p-type ohmic contact layer. Due to the light absorption of these metal layers, the optical output power of LEDs with top

emission configuration is greatly reduced. The flip chip configuration is an effective approach to overcome this issue. Compared with top emitting configuration, the light extraction with a flip chip configuration is from the back surface of the sapphire substrate.

Due to the roughness of the surface of the sapphire substrate, the light extraction efficiency of the flip chip LEDs is increased. Moreover, the p-type ohmic contact layer and bonding pad of the flip chip configuration can be thicker, which in turn reduces the contact resistance. These thick metal layers can also act as a reflective mirror, increasing the optical output power of flip chip LEDs. Furthermore, by using a p-type ohmic contact with high reflectivity, the optical output power of LEDs with flip chip configuration can be further improved. The III-nitride micro-LEDs (μLEDs) fabricated in this work are based on flip chip configuration.

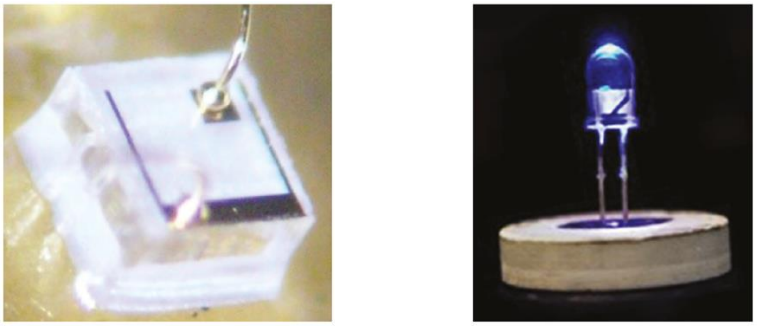

(a) **(b)**

FIGURE 1.17: Close-up images of (a) a bare and (b) packaged blue GaN LED. After [56].

Generally, the conventional broad area LEDs have dimensions over a few millimeters. Due to the large self-heating and high current crowding contributed by the broad area, the achievable maximum driving current density of these LEDs is low. Consequently, the power density of these LEDs is relatively small. Moreover, due to their large emitting area, the RC constant significantly limits the modulation bandwidth of the conventional broad area LEDs. R is the overall series resistance of the driving circuit and the diode. C is the diode capacitance. The RC time constant is the rise and the fall time of the diodes, which are equal. In turn, the

modulation bandwidth of these LEDs is very low (around 20 MHz) [57]. To overcome these problems, μLEDs have been developed. The μLEDs are the LEDs with an emission area of less than 100 μm in each dimension [58]. Compared with a broad area LEDs, μLEDs has a much smaller emission area. Therefore, hundreds of μLEDs can be produced in the same area as a single broad area LED. The first μLED was reported in 2000 by Jin et al [59]. Figure 1.18 (a) and (b) show schematic and scanning electron microscopy micrograph of the disc-shaped μLEDs fabricated in their work. The diameter of these μLEDs is 12 μm. In this work, they found that the quantum efficiency per area of μLEDs is greatly enhanced compared with conventional broad area LEDs. In 2001, a 10 $\times$ 10 blue μLED array was demonstrated by the same group [60]. Figure 1.18 (c) and (d) show the optical image of this individually addressable μLED array and the optical pattern displayed by this array. As shown, each μLED element in this array needs to be connected by its own p-contact pad to enable individually addressing. However, this addressing scheme is relatively hard to achieve for a larger number of μLED elements. To overcome this issue, a matrix addressing scheme has been developed, which was demonstrated in the early work of our group [61].

Due to the better thermal management, less current crowding, and enhanced LEE, μLEDs can sustain higher operating current density and offer higher power density [62–64]. Meanwhile, the modulation bandwidth of μLEDs is limited by the differential carrier lifetime and the *RC* time constant [5]. As section 1.2 mentioned, the diode capacitance is proportional to its area. So, the capacitance of an LED can be reduced by mesa etching. Although reducing the size of an LED would increase its resistance, the RC time constant of it can still be reduced effectively [65]. As a result, the RC time constant of the LED is reduced, and the modulation bandwidth of it increases. Furthermore, the RC time constant of the LED also can be reduced by decreasing the pixel size of it. Meanwhile, it has been proved that the RC time constant has significantly influence to the modulation bandwidth of an LED, when the radius of the pixel of the LED is larger than 20 μm [65]. Therefore, the modulation bandwidth of a single μLED can be

extremely high which is up to 830 MHz at 16 KA/cm^{-2} [66]. Nowadays, μLEDs have been applied to many different applications, such as self-emissive displays and optogenetic. It is also a strong candidate for optical communications, which can solve the problem of limited availability of the radio frequency (RF) spectrum in modern wireless communication system. The details of LED based free space optical communications will be given in the following section.

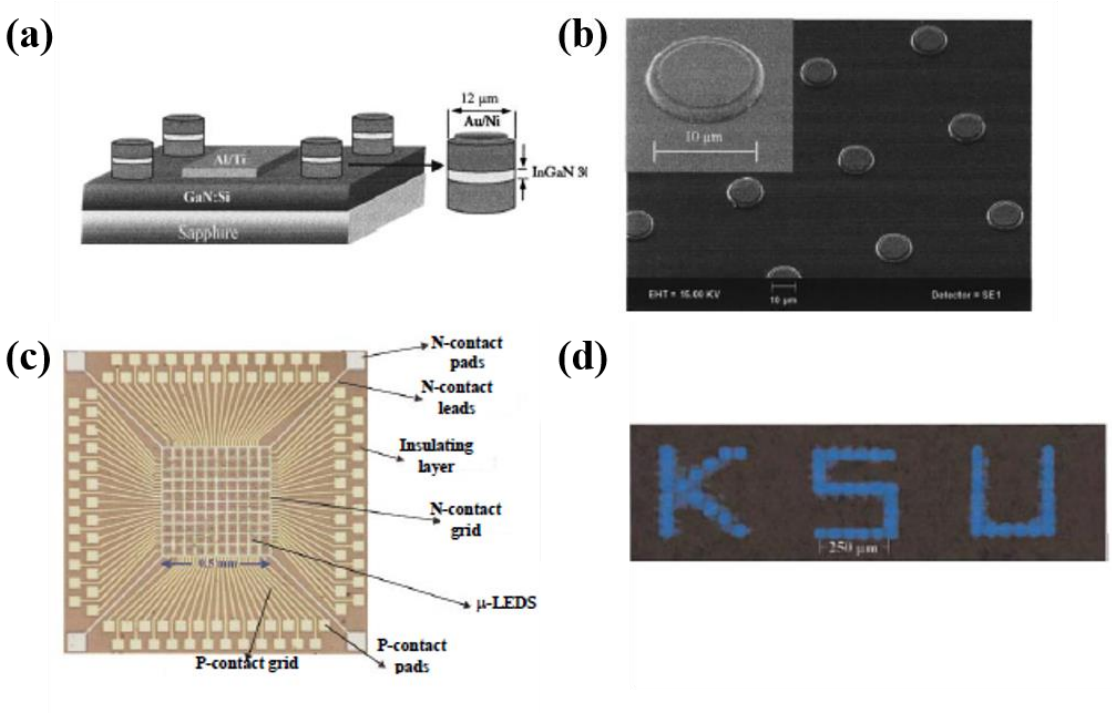

FIGURE 1.18: (a) Schematic of the first μLED, (b) SEM image of the first μLED, (c) optical image of an individually addressable the μLED array, and (d) optical pattern displayed by this μLED array. After [59, 60].

1.4 LED based free space optical communication

1.4.1 LED based visible light communication

Visible light communication (VLC) is a data communication which enabled by modulating visible light emitting devices, using a data source. To establish high speed optical communication link, this technology uses visible sources (emitting

from 375 – 780 nm) to transmit optical signals. The transmitted optical signals are then received by photoreceivers. The main idea for VLC is to use the unlicensed visible wavelength spectrum to overcome the data crowding in RF communication. The details of VLC link establishment and its modulation schemes are presented in chapter 3.

The first VLC system was reported in 1880. At the time, Alexander Graham Bell invented the photophone, which transmitted speech on modulated sunlight over several hundred meters [67]. However, due to the lack of suitable optical transmitters, the development of VLC was extremely slow until early 1990. As mentioned before, in 1990, breakthroughs in III-nitride semiconductor materials were achieved. Compared with other light sources, such as a mercury-xenon lamp and a mercury-argon lamp, III-nitride LEDs offer a larger modulation bandwidth. As a result, the VLC technology based on LEDs is rapidly advancing. In early work, the data transmission rates of commercial broad area LED based VLC were in the range of 100 Mbps [68, 69]. Within more advanced modulation schemes and equalization techniques, the data rate of such a VLC system can achieve a few Gbps [70, 71]. Moreover, with the fast development of semiconductor technologies, the cost of III-nitride LEDs keeps falling while the efficiencies of them keep increasing. It leads to a potential that III-nitride LEDs will become the standard illumination source in the future. Thus, utilizing modulated LED light for both illumination and data communications becomes possible. Such an approach is named Li-Fi. Figure 1.19 shows an illustration of a Li-Fi system. However, it is relatively difficult to achieve high speed (over Gbps) VLC systems due to the low bandwidth of commercial LEDs (generally around 20 MHz). To overcome this issue, μLEDs have been introduced into the VLC system. As mentioned above, μLEDs have extremely high modulation bandwidth compared with commercial LEDs. It makes them a perfect candidate for high-speed VLC applications. More details of μLED and μLED array based VLC systems developed in this work will be given in chapter 4 and 5.

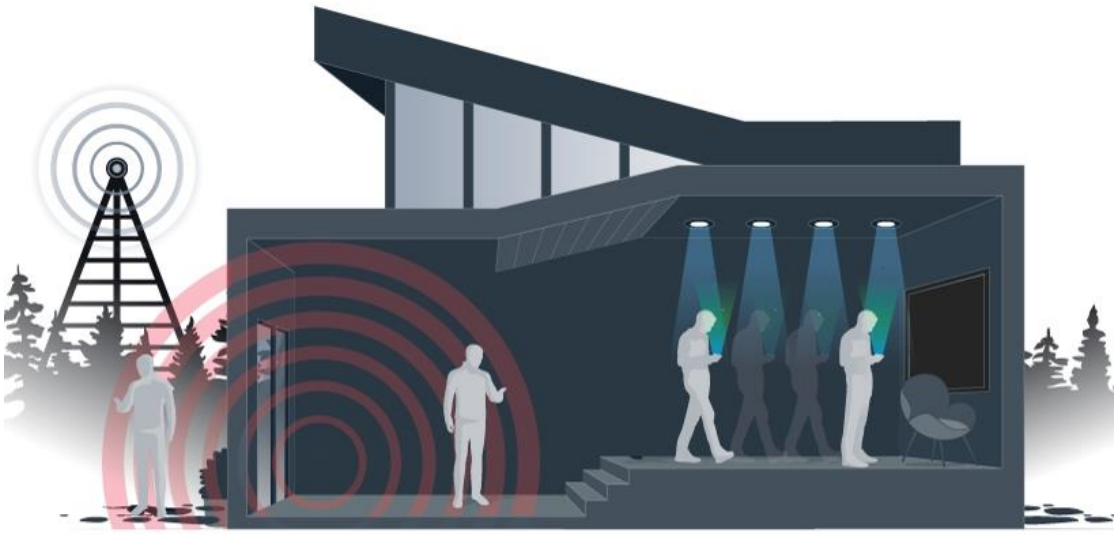

FIGURE 1.19: Illustration of Li-Fi concept. After [72].

1.4.2 LED based deep UV communication

Deep UV communications have gained great interest recently due to several advantages compared with visible light communications. As we knew, the solar radiation has a strong influence on visible light based optical communication links due to the high background noise [73]. However, most of the solar UV radiation especially in the UV-C band between 200 nm and 280 nm is absorbed by the ozone layer in Earth's stratosphere. As a result, deep UV radiation at ground level is negligible [74]. Therefore, the background noise of deep UV optical wireless communications is negligibly low in both indoor and outdoor communication systems. Meanwhile, due to the strong scattering of deep UV light in the air [75], a non-line-of-sight (NLOS) communication link with reduced pointing, acquisition, and tracking requirements, can be constructed by using deep UV light sources [76]. Furthermore, deep UV communication links between satellites would be hardly traceable at ground level due to the strong UV absorption by the ozone layer. Consequently, outer space deep UV communications are highly secure. Recently, due to the fast development of deep UV light sources, filters, and detectors, many research efforts have been made on deep UV communications [77, 78]. Figure 1.20

shows some potential applications of deep UV communications. As shown in figure 1.20 (a), a deep UV communication link can be established between two satellites. Figure 1.20 (b) illustrates an idea of deep UV based NLOS communication links in a city [73].

Recently, semiconductor UV LEDs have been used for deep UV communications [79]. However, the data transmission rate of deep UV communication is still low. In order to achieve deep UV communications with much higher data transmission rates, deep UV μLEDs have been developed and introduced into the deep UV system in this work. More details of deep UV μLEDs and μLED based deep UV systems will be given in chapter 6.

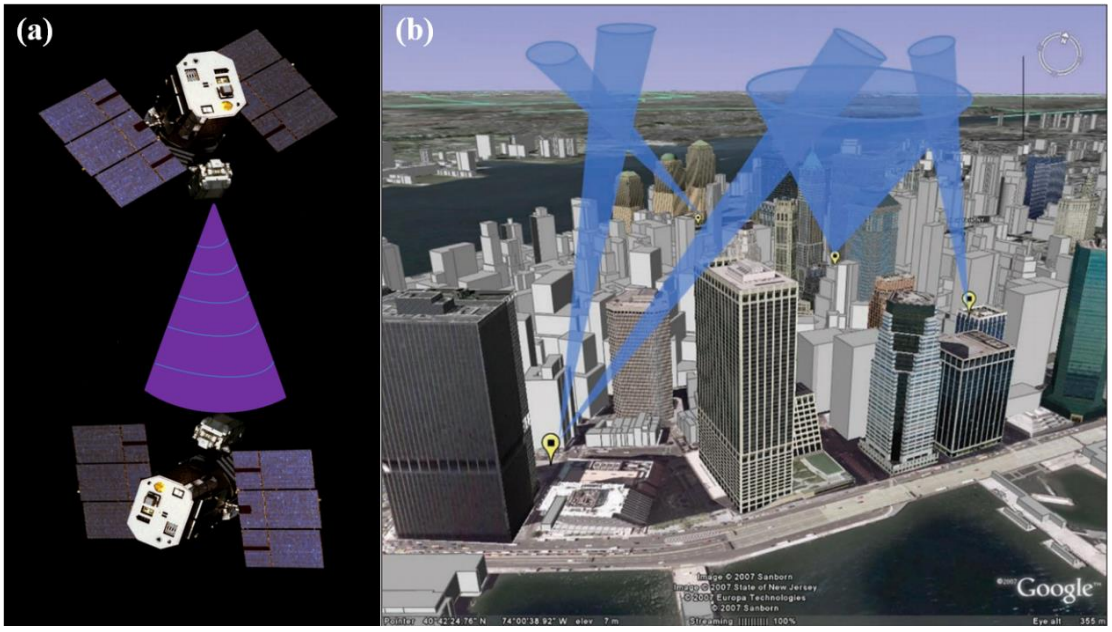

FIGURE 1.20: Examples of deep UV communications used in (a) satellites and (b) city NLOS communication network. After [73].

1.5 Outline of this thesis

In this chapter, a general introduction of III-nitride materials and III-nitride material based LEDs and μLED are given. Moreover, a newly emerging LED based

free space optical communication was also introduced. The fabrication and characterization techniques used in this work to develop μLEDs will be described in chapter 2. Chapter 3 will present the details of free space optical communication systems and modulation schemes. From chapter 4 to chapter 6, the new results achieved from this work will be presented. In particular, the development and application of III-nitride based series-biased μLEDs will be presented in chapter 4. Chapter 5 will demonstrate the development and application of III-nitride based μLED arrays with individually addressable n-electrodes. The development of deep UV μLEDs and their application will be given in chapter 6. Finally, chapter 7 will give the conclusion of this thesis, along with some future work plans.

References

[1] H. J. Round. A Note on Carborundum. Elektron. *World*, 149:308–309, 1907.

[2] O. V. Lossev. CII. Luminous carborundum detector and detection effect and oscillations with crystals. *The London, Edinburgh, and Dublin Philosophical Magazine and Journal of Science*, 6(39):1024–1044, 1928.

[3] R. N. Hall, G. E. Fenner, J. D. Kingsley, T. J. Soltys, and R. O. Carlson. Coherent light emission from GaAs junctions. *Physical Review Letters*, 9(9):366, 1962.

[4] N. Holonyak and S. F. Bevacqua. Coherent (visible) light emission from $Ga(As_{1-x}P_x)$ junctions. *Applied Physics Letters*, 1(4):82–83, 1962.

[5] E. F. Schubert. *Light-Emitting Diodes*. Cambridge University Press, 2006.

[6] R. A. Logan, H. G. White, and W. Wiegmann. Efficient green electroluminescence in nitrogen-doped GaP p-n junctions. *Applied Physics Letters*, 13(4):139–141, 1968.

[7] J. I. Pankove, E. A. Miller, and J. E. Berkeyheiser. GaN blue light-emitting diodes. *Journal of Luminescence*, 5(1):84–86, 1972.

[8] R. B. Jain and H. P. Maruska. How it really happened: The history of p-type doping of gallium nitride. *Physica Status Solidi (a)*, 204(6):1970–1976, 2007.

[9] S. Nakamura and M. R. Krames. History of gallium–nitride-based light-emitting diodes for illumination. *Proceedings of the IEEE*, 101(10):2211–2220, 2013.

[10] H. Amano, N. Sawaki, I. Akasaki, and Y. Toyoda. Metalorganic vapor phase epitaxial growth of a high quality GaN film using an AlN buffer layer. *Applied Physics Letters*, 48(5):353–355, 1986.

[11] H. Amano, M. Kito, K. Hiramatsu, and I. Akasaki. P-type conduction in Mg-doped GaN treated with low-energy electron beam irradiation (LEEBI). *Japanese Journal of Applied Physics*, 28(12A):L2112, 1989.

[12] S. Nakamura, N. Iwasa, and M. Senoh. Method of manufacturing p-type compound semiconductor, April 26 1994. US Patent 5,306,662.

[13] M. der Maur, A. Pecchia, G. Penazzi, W. Rodrigues, and A. Di Carlo. Unraveling the" Green Gap" problem: The role of random alloy fluctuations in InGaN/GaN light emitting diodes. *arXiv preprint*, 2015.

[14] LED bulbs. `https://www.which.co.uk/news/2018/10/nine-amazing-things-you-didnt-know-about-led-light-bulbs/`, Accessed 2021-06-08.

[15] Car headlights. `https://dailycarcare.com/best-led-headlights/`, Accessed 2021-06-08.

[16] LED monitor. `https://www.lg.com/uk/led-monitors`, Accessed 2021-06-08.

[17] Press release: New light to illuminate the world. `https://www.lg.com/uk/led-monitors`, Accessed 2021-06-08.

[18] J. K. Kim and E. F. Schubert. Transcending the replacement paradigm of solid-state lighting. *Optics Express*, 16(26):21835–21842, 2008.

[19] P. M. Pattison, M. Hansen, and J. Y. Tsao. LED lighting efficacy: Status and directions. *Comptes Rendus Physique*, 19(3):134–145, 2018.

[20] R. Haitz, F. Kish, J. Tsao, and J. Nelson. The case for a national research program on semiconductor lighting. *Optoelectronics Industry Development Association*, pages 1–24, 1999.

[21] Tomislav Pavlovic. *The Sun and Photovoltaic Technologies*. Springer Nature, 2019.

[22] S. U. Yuruker, M. Arik, E. Tamdogan, R. Melikov, S. Nizamoglu, D. A. Press, and I. Durak. Thermal and optical performance of eco-friendly silk fibroin proteins as a cavity encapsulation over LED systems. *American Society of Mechanical Engineers*, 56901, 2015.

[23] I. Vurgaftman and J. R. Meyer. Band parameters for nitrogen-containing semiconductors. *Journal of Applied Physics*, pages 3675–3696, 2003.

[24] M. Fukuda. *Optical semiconductor devices*, volume 46. John Wiley & Sons, 1998.

[25] S. M. Sze and M. K. Lee. Semiconductor Devices. Physics and Technology. 2013.

[26] K. B. Nam, J. Li, M. L. Nakarmi, J. Y. Lin, and H. X. Jiang. Unique optical properties of AlGaN alloys and related ultraviolet emitters. *Applied physics letters*, 84(25):5264–5266, 2004.

[27] X. Li, T. Kao, M. Satter, Y. Wei, S. Wang, H. Xie, S. Shen, P. Yoder, A. M. Fischer, F. A. Ponce, T. Detchprohm, and R. D. Dupuis. Demonstration of transverse-magnetic deep-ultraviolet stimulated emission from AlGaN multiple-quantum-well lasers grown on a sapphire substrate. *Applied Physics Letters*, 106(4):041115, 2015.

[28] D. A. Neamen. *Semiconductor physics and devices: basic principles*. New York, NY: McGraw-Hill,, 2012.

[29] E. Liu, B. Zhu, and J. Luo. *Physics of semiconductor (in chinese)*. Electronic Industry Press, 2008.

[30] S. Kasap and P. Capper. *Springer handbook of electronic and photonic materials*. Springer, 2017.

[31] M. Fox. Optical properties of solids, 2002.

[32] M. Fox and R. Ispasoiu. Quantum wells, superlattices, and band-gap engineering. *Springer Handbook of Electronic and Photonic Materials*, pages 1–1, 2017.

[33] E. Xie. *High performance microstructured light emitting diodes: mechanisms and processes*. PhD thesis, University of Strathclyde, 2013.

[34] I. M. Watson. Metal organic vapour phase epitaxy of AlN, GaN, InN and their alloys: A key chemical technology for advanced device applications. *Coordination Chemistry Reviews*, 257(13-14):2120–2141, 2013.

[35] S. N. Alam, V. Z. Zubialevich, B. Ghafary, and P. J. Parbrook. Bandgap and refractive index estimates of InAlN and related nitrides across their full composition ranges. *Scientific Reports*, 10(1):1–9, 2020.

[36] L. Kuchipudi. Modeling and Analysis of Quantum Well Structures in GaNInGaN Light Emitting Diodes, 2014.

[37] F. Hamdani, A. Botchkarev, W. Kim, H. Morkoç, M. Yeadon, J. M. Gibson, S. Tsen, D. J. Smith, D. C. Reynolds, D. C. Look, K Evans, C. W. Litton, W. C. Mitchel, and P. Hemenger. Optical properties of GaN grown on ZnO by reactive molecular beam epitaxy. *Applied Physics Letters*, 70(4):467–469, 1997.

[38] D. Zhao, S. Xu, M. Xie, S. Tong, and H. Yang. Stress and its effect on optical properties of GaN epilayers grown on Si (111), 6H-SiC (0001), and c-plane sapphire. *Applied Physics Letters*, 83(4):677–679, 2003.

[39] S. Chang, Y. Lin, Y. Su, C. Chang, T. Wen, S. Shei, J. Ke, C. Kuo, S. Chen, and C. Liu. Nitride-based LEDs fabricated on patterned sapphire substrates. *Solid-State Electronics*, 47(9):1539–1542, 2003.

[40] D. Zhu, D. J. Wallis, and C. J. Humphreys. Prospects of III-nitride optoelectronics grown on Si. *Reports on Progress in Physics*, 76(10):106501, 2013.

[41] S. Zhou, Z. Lin, H. Wang, T. Qiao, L. Zhong, Y. Lin, W. Wang, W. Yang, and G. Li. Nucleation mechanism for epitaxial growth of GaN on patterned sapphire substrates. *Journal of Alloys and Compounds*, 610:498–505, 2014.

[42] K. Tadatomo. Epitaxy part B. Epitaxial growth of GaN on patterned sapphire substrates. In *III-Nitride Based Light Emitting Diodes and Applications*, pages 59–81. Springer, 2013.

[43] R. P. Green, J. J. D. McKendry, D. Massoubre, E. Gu, D. Dawson, M, and A. E. Kelly. Modulation bandwidth studies of recombination processes in blue and green InGaN quantum well micro-light-emitting diodes. *Applied Physics Letters*, 102(9):091103, 2013.

[44] J. Shen, D. Zhang, F. Zhang, and Y. Gan. AFM characterization of patterned sapphire substrate with dense cone arrays: Image artifacts and tip-cone convolution effect. *Applied Surface Science*, 433:358–366, 2018.

[45] S. C. Jain, M. Willander, J. Narayan, and R. V. Overstraeten. III–nitrides: Growth, characterization, and properties. *Journal of Applied Physics*, 87(3):965–1006, 2000.

[46] S. Nakamura, T. Mukai, and M. Senoh. In situ monitoring and Hall measurements of GaN grown with GaN buffer layers. *Journal of Applied Physics*, 71(11):5543–5549, 1992.

[47] J. Sheu and G. C. Chi. The doping process and dopant characteristics of GaN. *Journal of Physics: Condensed Matter*, 14(22):R657, 2002.

[48] S. Nakamura, T. Mukai, and M. Senoh. Si-and Ge-doped GaN films grown with GaN buffer layers. *Japanese Journal of Applied Physics*, 31(9R):2883, 1992.

[49] S. Nakamura, T. Mukai, M. Senoh, and N. Iwasa. Thermal annealing effects on p-type Mg-doped GaN films. *Japanese Journal of Applied Physics*, 31(2B):L139, 1992.

[50] W. Götz, N. M. Johnson, J. Walker, D. P. Bour, and R. A. Street. Activation of acceptors in Mg-doped GaN grown by metalorganic chemical vapor deposition. *Applied Physics Letters*, 68(5):667–669, 1996.

[51] J. Ryou, P. D. Yoder, J. Liu, Z. Lochner, H. Kim, S. Choi, H. Kim, and R. D. Dupuis. Control of quantum-confined stark effect in InGaN-based quantum wells. *IEEE Journal of Selected Topics in Quantum Electronics*, 15(4):1080–1091, 2009.

[52] M. Kneissl, J. Rass, L. Schade, and U. T. Schwarz. Growth and optical properties of GaN-based non-and semipolar LEDs. *III-Nitride Based Light Emitting Diodes and Applications*, pages 83–119, 2013.

[53] H. Chen, D. Yeh, Y. Lu, C. Chen, C. Huang, T. Tang, C. C. Yang, C. Wu, and C. Chen. Strain relaxation and quantum confinement in InGaN/GaN nanoposts. *Nanotechnology*, 17(5):1454, 2006.

[54] Y. Kawakami, A. Kaneta, L. Su, Y. Zhu, K. Okamoto, M. Funato, A. Kikuchi, and K. Kishino. Optical properties of InGaN/GaN nanopillars fabricated by postgrowth chemically assisted ion beam etching. *Journal of Applied Physics*, 107(2):023522, 2010.

[55] S. Nakamura, T. Mukai, and M. Senoh. Candela-class high-brightness InGaN/AlGaN double-heterostructure blue-light-emitting diodes. *Applied Physics Letters*, 64(13):1687–1689, 1994.

[56] S. Nakamura. Nobel Lecture: Background story of the invention of efficient blue InGaN light emitting diodes. *Reviews of Modern Physics*, 87(4):1139, 2015.

[57] S. Rajbhandari, J. J. D. McKendry, J. Herrnsdorf, H. Chun, G. Faulkner, H. Haas, I. M. Watson, D. O'Brien, and M. D. Dawson. A review of gallium nitride LEDs for multi-gigabit-per-second visible light data communications. *Semiconductor Science and Technology*, 32(2):023001, jan 2017.

[58] T. Wu, C. Sher, Y. Lin, C. Lee, S. Liang, Y. Lu, C. Huang, W. Sung, W. Guo, H. Kuo, and Z. Chen. Mini-LED and micro-LED: promising candidates for the next generation display technology. *Applied Sciences*, 8(9):1557, 2018.

[59] S. Jin, J. Li, J. Li, J.and Lin, and H. Jiang. GaN microdisk light emitting diodes. *Applied Physics Letters*, 76(5):631–633, 2000.

[60] H. Jiang, S. Jin, J. Li, J. Shakya, and J. Lin. III-nitride blue microdisplays. *Applied Physics Letters*, 78(9):1303–1305, 2001.

[61] Z. Gong, H. Zhang, E. Gu, C. Griffin, M. D. Dawson, V. Poher, G. Kennedy, P. M. W. French, and M. A. A. Neil. Matrix-addressable micropixellated InGaN light-emitting diodes with uniform emission and increased light output. *IEEE Transactions on Electron Devices*, 54(10):2650–2658, 2007.

[62] Z. Gong, S. Jin, Y. Chen, J. J. D. Mckendry, D. Massoubre, I. M. Watson, E. Gu, and M. D. Dawson. Size-dependent light output, spectral shift, and self-heating of 400 nm InGaN light-emitting diodes. *Journal of Applied Physics*, 107(1):013103, 2010.

[63] X. Guo and E. F. Schubert. Current crowding and optical saturation effects in GaInN/GaN light-emitting diodes grown on insulating substrates. *Applied Physics Letters*, 78(21):3337–3339, 2001.

[64] H. W. Choi, C. W. Jeon, M. D. Dawson, P. R. Edwards, R. W. Martin, and S. Tripathy. Mechanism of enhanced light output efficiency in InGaN-based microlight emitting diodes. *Journal of Applied Physics*, 93(10):5978–5982, 2003.

[65] C. Lin, C. Tu, Y. Yao, S. Chen, C. Su, H. Chen, Y. Kiang, and C. C. Yang. High Modulation Bandwidth of a Light-Emitting Diode With Surface Plasmon Coupling. *IEEE Transactions on Electron Devices*, 63(10):3989–3995, 2016.

[66] R. X. G. Ferreira, E. Xie, J. J. D. McKendry, S. Rajbhandari, H. Chun, G. Faulkner, S. Watson, A. E. Kelly, E. Gu, R. V. Penty, D. C. Watson, I. M .and O'Brien, and M. D. Dawson. High bandwidth GaN-based micro-LEDs for multi-Gb/s visible light communications. *IEEE Photonics Technology Letters*, 28(19):2023–2026, 2016.

[67] A. G. Bell. On selenium and the photophone. *Electrician*, 5:214–220, 1880.

[68] H. Le Minh, D. O'Brien, G. Faulkner, L. Zeng, K. Lee, D. Jung, Y. Oh, and E. T. Won. 100-Mb/s NRZ Visible Light Communications Using a Postequalized White LED. *IEEE Photonics Technology Letters*, 21(15):1063–1065, 2009.

[69] J. Grubor, S. C. J. Lee, K. Langer, T. Koonen, and J. W. Walewski. Wireless High-Speed Data Transmission with Phosphorescent White-Light LEDs. In *33rd European Conference and Exhibition of Optical Communication - Post-Deadline Papers (published 2008)*, pages 1–2, 2007.

[70] A. H. Azhar and D. O'Brien. Experimental comparisons of optical OFDM approaches in visible light communications. In *2013 IEEE Globecom Workshops (GC Wkshps)*, pages 1076–1080, 2013.

[71] G. Cossu, A. M. Khalid, P. Choudhury, R. Corsini, and E. Ciaramella. 3.4 Gbit/s visible optical wireless transmission based on RGB LED. *Opt. Express*, 20(26):B501–B506, Dec 2012.

[72] Li-Fi illustration. `https://www.themanufacturer.com/articles/future-demand-iot-enabled-li-fi-technology-grow/`, Accessed 2021-06-08.

[73] X. Fernando and H. Farahneh. *Visible Light Communications*. IOP Publishing, 2019.

[74] Z. Xu and B. M. Sadler. Ultraviolet communications: potential and state-of-the-art. *IEEE Communications Magazine*, 46(5):67–73, 2008.

[75] S. Karp, R. M. Gagliardi, S. E. Moran, and L. B. Stotts. *Optical Channels: Fibers, Clouds, Water, and the Atmosphere (Applications of Communications Theory)*. Springer Science and Business Media, 2013.

[76] D. E. Suntein. *A scatter communications link at ultraviolet frequencies*. Massachusetts institute of Technology, 1968.

[77] T. Feng, F. Xiong, Q. Ye, Z. Pan, Z. Dong, and Z. Fang. Non-line-of-sight optical scattering communication based on solar-blind ultraviolet light. In Dominique Chiaroni, Wanyi Gu, Ken ichi Kitayama, and Chang-Soo Park, editors, *Optical Transmission, Switching, and Subsystems V*, volume 6783, pages 1008 – 1014. International Society for Optics and Photonics, SPIE, 2007.

[78] D. Han, Y. Liu, K. Zhang, P. Luo, and M. Zhang. Theoretical and experimental research on diversity reception technology in NLOS UV communication system. *Opt. Express*, 20(14):15833–15842, Jul 2012.

[79] X. Sun, Z. Zhang, A. Chaaban, T. K. Ng, C. Shen, R. Chen, J. Yan, H. Sun, X. Li, J. Wang, J. Li, M. Alouini, and B. S. Ooi. 71-Mbit/s ultraviolet-B LED communication link based on 8-QAM-OFDM modulation. *Optics Express*, 25(19):23267–23274, 2017.

Chapter 2

Fabrication and characterization techniques of micro-structured light emitting diodes

My research works mainly focus on the development of novel III-nitride μLEDs for free-space optical communications. In this chapter, the principles of the techniques used for μLED fabrications and the tools used for μLED characterization are introduced. The first section presents the main steps in the μLED fabrication process, including pattern definition, pattern etching and the formation of metal contacts. These techniques are of paramount importance to the fabrication of III-nitride μLEDs. The following section describes some μLED characterization techniques used in this work.

2.1 Fabrication techniques of microstructured light emitting diodes

In this work, the μLEDs are fabricated from commercially available III-nitride LED wafers grown on c-plane sapphire [1–3]. The detailed introduction of the III-nitride materials has been given in chapter 1. The schematic diagram in figure 2.1 shows the typical fabrication process of the III-nitride μLEDs. The fabrication of the μLEDs is challenging due to its small feature size. In order to achieve the μLEDs, several micro-fabrication techniques have been used. In the following subsections, these techniques will be briefly introduced along with the fabrication challenges.

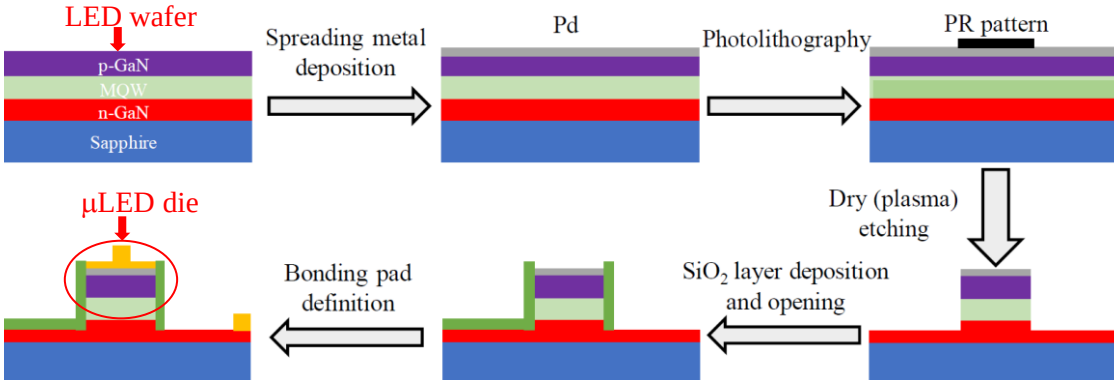

FIGURE 2.1: Schematic of the fabrication process of III-nitride μLEDs

2.1.1 Pattern definition

In the fabrication process of μLEDs, pattern definition is the most crucial step which is achieved by transferring the designed pattern from a photomask to a target sample. Photolithography is a commonly used technique for pattern definition in the modern semiconductor industry. In the following sections, the photolithographic technique used in this work will be introduced in detail.

By using photolithographic technique, the designed patterns are transferred from a photomask to a photosensitive layer spun on a sample through light exposure. Figure 2.2 shows the typical photolithography process. The first step is to spin coat the sample with a photosensitive layer, which normally is a photoresist layer. Then, this photoresist layer is exposed by the light through a photomask. The photomask contains many different designed patterns which consist of clear and opaque regions. For the positive photoresist used in this work, the photoresist layer under clear regions of the mask will be exposed by the light. As a result, there is a property change in the photoresist layer due to the photochemical reaction. In contrast, the photoresist layer under opaque regions will be protected from photochemical reaction during the light exposure [4]. In order to form a desired photoresist pattern, the light exposed sample is then dipped into a suitable developer to remove the unwanted photoresist. There are three steps in the photolithography process, which are spin coating of photoresist, alignment and exposure, and photoresist development. The step of alignment and exposure is the most critical step in photolithography, which determines the success of the designed pattern transferring, the minimum feature size and quality of the transferred photoresist patterns.

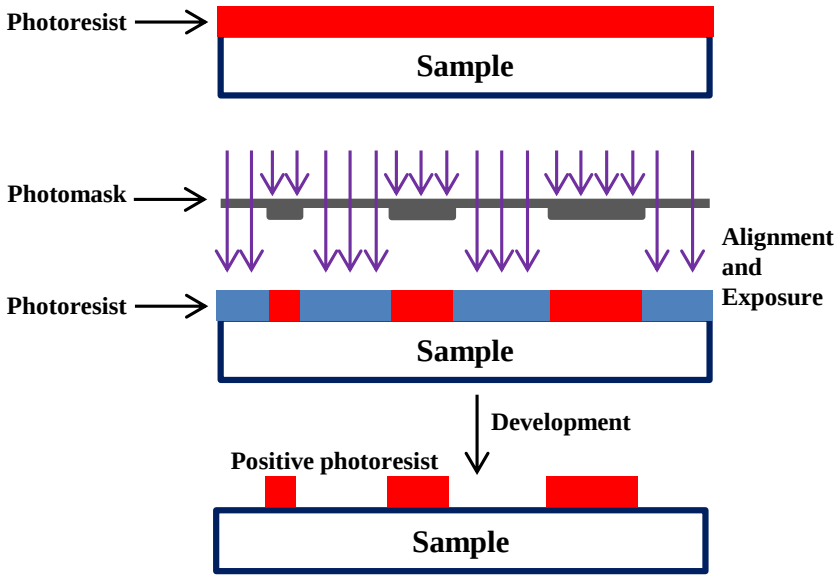

FIGURE 2.2: Classic photolithography process with positive photoresist.

The alignment and exposure in this work was performed by a Karl Suss MA6 Mask Aligner, which consists of three main parts i.e. microscope, alignment stage and lamp housing. Figure 2.3 presents the image of the Karl Suss MA6 Mask Aligner used for the alignment and exposure processes in this work. Before the exposure process, the sample is first aligned with a photomask in the alignment stage under the observation through the microscope. During the alignment, the sample position and orientation can be adjusted by the alignment stage and there is a tiny gap (30 μm) between the sample and the photomask, which allows the sample to move without any damage. In this mask aligner, the model of lamp housing is UV400, which has the emission peaks at 365, 405 and 436 nm. The lamp housing consists of two main parts i.e. a high pressure mercury short-arc lamp and corresponding electrical circuit. Figure 2.4 shows the emission spectrum of the high pressure mercury short-arc lamp, which mainly concentrates on 350 to 450 nm wavelength region. A minimum pattern feature size of 2 μm could be accomplished under the exposure from this multi-wavelength mercury lamp.

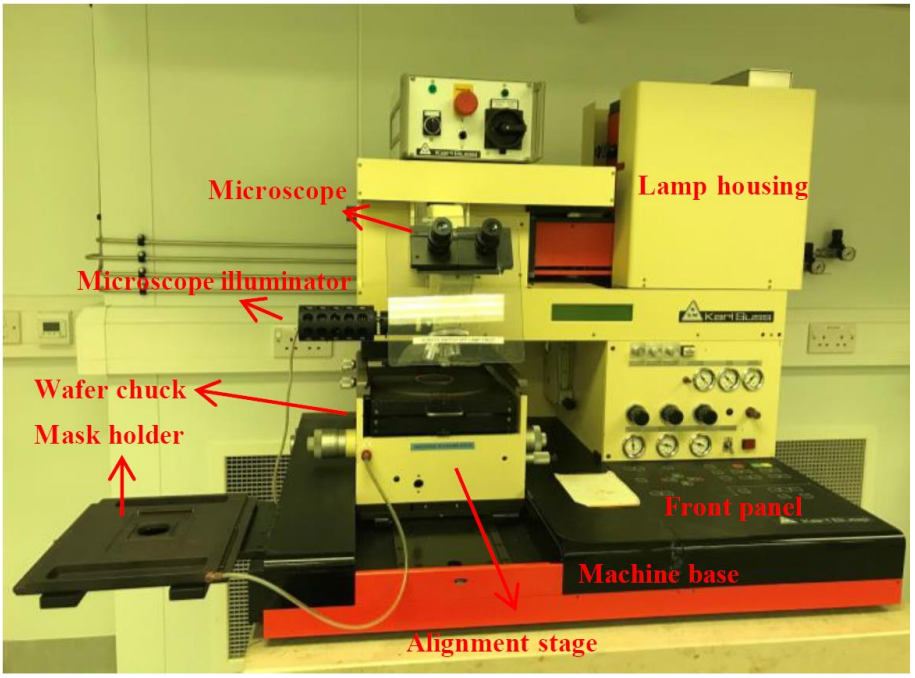

FIGURE 2.3: Image of a Karl Suss MA6 Mask Aligner used in this work.

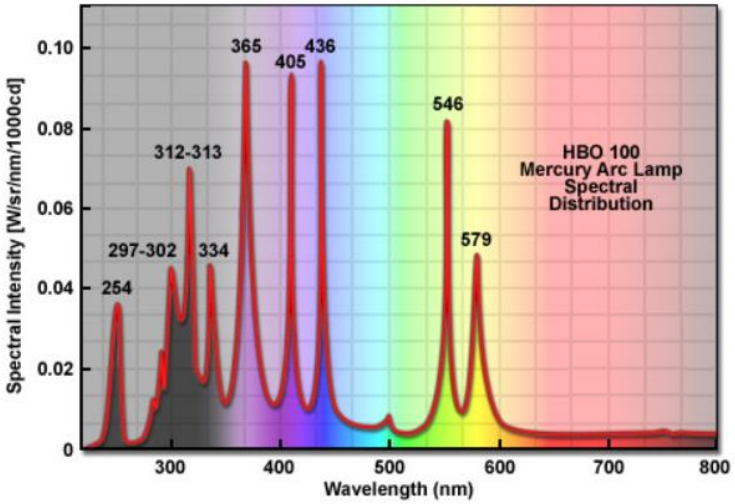

FIGURE 2.4: Emission spectrum of the HBO 100 high pressure mercury short-arc lamp. After [5]

2.1.2 Pattern transfer

After the pattern definition process, the pattern needs to be further transferred to the samples. In order to realize that, a dry (plasma) etching process is applied in this work. The principle of the dry etching process will be introduced in this subsection. The facilities and etching recipes used in this work will be given in detail.

In dry etching process, the exposed material on the sample surface is removed by the gaseous etchants. There are two different etching mechanisms in plasma dry etching, which are physical ion bombardment and pure chemical etching. Figure 2.5 shows the schematics of the two etching mechanisms. As figure 2.5 (a) demonstrates, the energetic ions bombard the exposed area to remove the material from the sample surface. The etching rate of physical ion bombardment is highly depending on the flux and energy of ions. Figure 2.5 (b) shows the reaction of pure chemical etching. In this etching process, the exposed material is etched by the gaseous etchants to form easily-removed volatile byproducts. The etching rate of this process is strongly depended on the chemical reaction that occurs between

the exposed material and the gaseous etchants. Furthermore, the byproducts in the pure chemical etching have to be volatile in order to avoid contaminating the sample. The non-volatile byproducts will deposit on the sample surface, which may influences or interrupts further chemical etching.

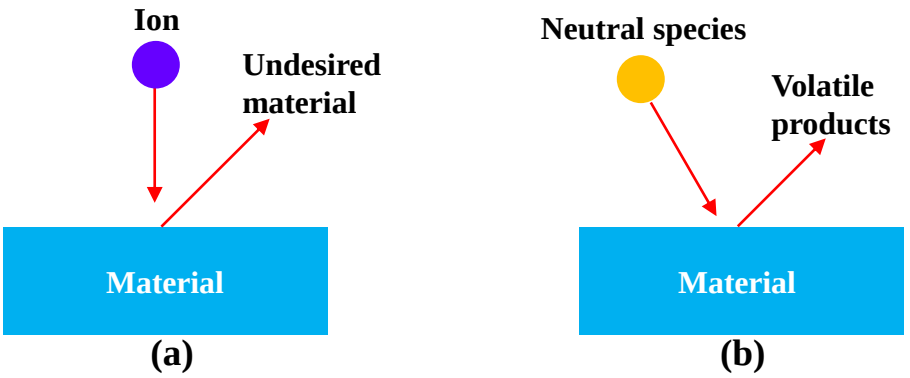

FIGURE 2.5: Schematics of (a) physical ion bombardment; (b) pure chemical etching reaction in dry etching process.

In this work, plasma dry etching is applied for the etching of SiO_2 and GaN-based materials, in order to achieve the small feature size of III-nitride μLEDs. A plasma is an ionized gas created by the voltage and neutral gas under particular reaction conditions [6]. It contains free radicals with highly chemical activity. The chemical reaction rate in the dry etching process can be increased significantly by these ions. As a result, the pure chemical etching is enhanced. Meanwhile, the pure chemical etching can also be accelerated by the physical ion bombardment, which may change the chemical property of the target material [7].

In this work, three plasma etching tools have been used, which are the Reactive Ion Etching (RIE) tool, Inductively Coupled Plasma (ICP) systems and Matrix Plasma asher (Asher). Figure 2.6 (a) shows the image of the RIE system used in this work, and Figure 2.6 (b) presents the schematic diagram of the processing chamber of it. Under a gas pressure between 5 to 150 mTorr, an electromagnetic field at a radio frequency (RF) of 13.56 MHz is applied, which initiates the plasma in the RIE chamber. The density of this plasma is quite low, which is about 1 to 5×10^9 cm^{-3}. The range of ion energy is between 30 to 1000 eV, which is highly

depended on the RF power and processing pressure. The RIE system in this work is mainly used for SiO_2 etching. Table 2.1 gives a SiO_2 etching recipe used in this work. By using this recipe, the SiO_2 etching rate is about 39 nm/min.

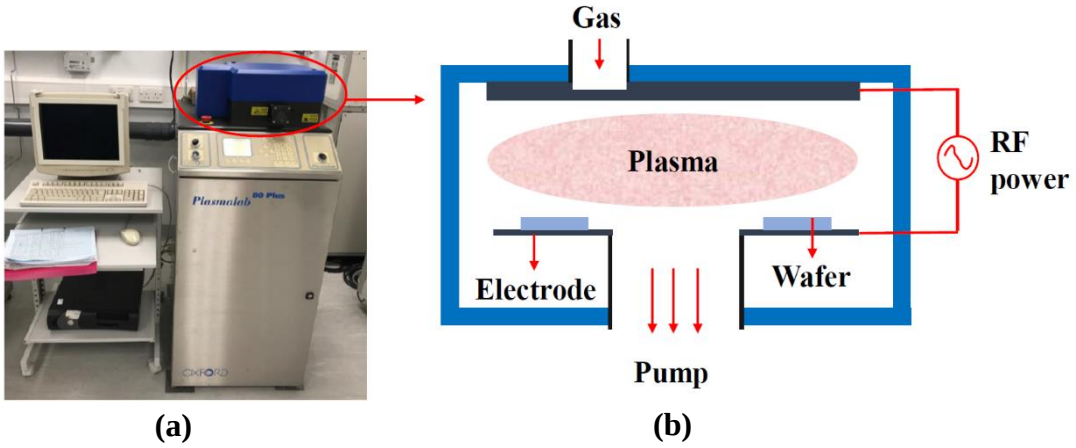

FIGURE 2.6: (a) Image of a RIE system and (b) schematic of its processing chamber.

TABLE 2.1: Etching recipe for SiO_2 in an RIE system.

Pressure (mTorr)	Ar flow (sccm)	CHF_3 flow (sccm)	RF power (W)	Etching rate (nm/min)
66	15	5	200	39

Figure 2.7 shows the image of the ICP system and a schematic diagram of its processing chamber. The ICP system is a kind of upgraded RIE system. It combines the RIE system with an inductively coupled plasma source which incorporates a radial inductive coil design. As a result, a high density (10^{11} - 10^{12} cm^{-3} under a 1 to 100 mTorr processing pressure) plasma can be generated by the radial inductive coil in the system and, in turn, an increased etching rate. In an ICP system, the platen power controls the energy of ions for physical ion bombardment, while the coil power controls the plasma density. The ICP system applied in this work is mainly used for the etching of the III-nitride materials with a specific recipe which is given in Table 2.2. Figure 2.8 shows a sample that has been pattern transformed by the ICP.

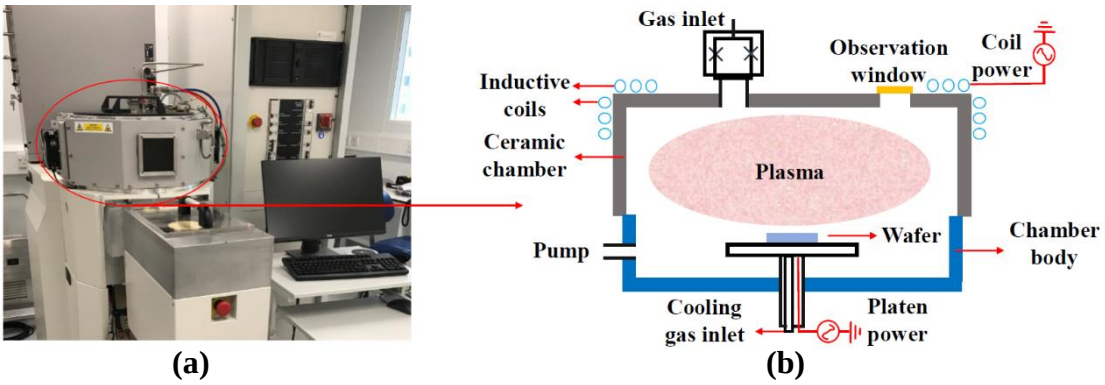

FIGURE 2.7: (a)Image of an ICP system and (b) schematic diagram of its processing chamber.

TABLE 2.2: Etching recipes for GaN-based materials in an ICP system.

Pressure (mTorr)	Ar flow (sccm)	Cl_2 flow (sccm)	Coil power (W)	Platen power (W)	Etching rate (nm/min)
7	10	30	400	200	418

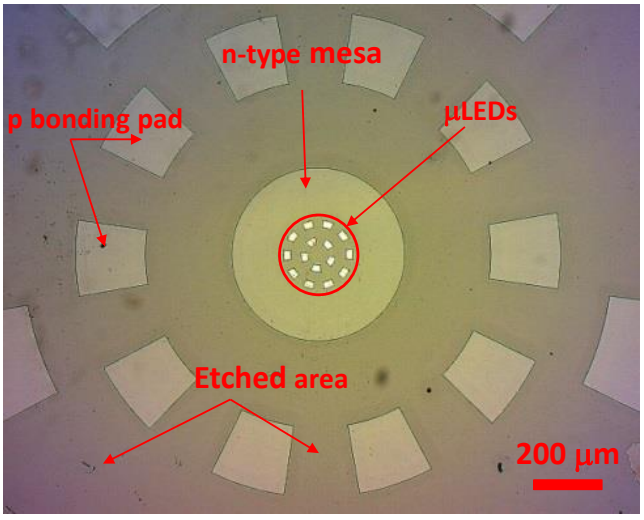

FIGURE 2.8: Image of a sample which has been pattern transformed by the ICP.

Furthermore, in the modern semiconductor industry, there is a kind of dry etching mainly used for removing the organic residual (e.g. photoresist) from an etched wafer, namely plasma ashing. The plasma ashing in this work is performed

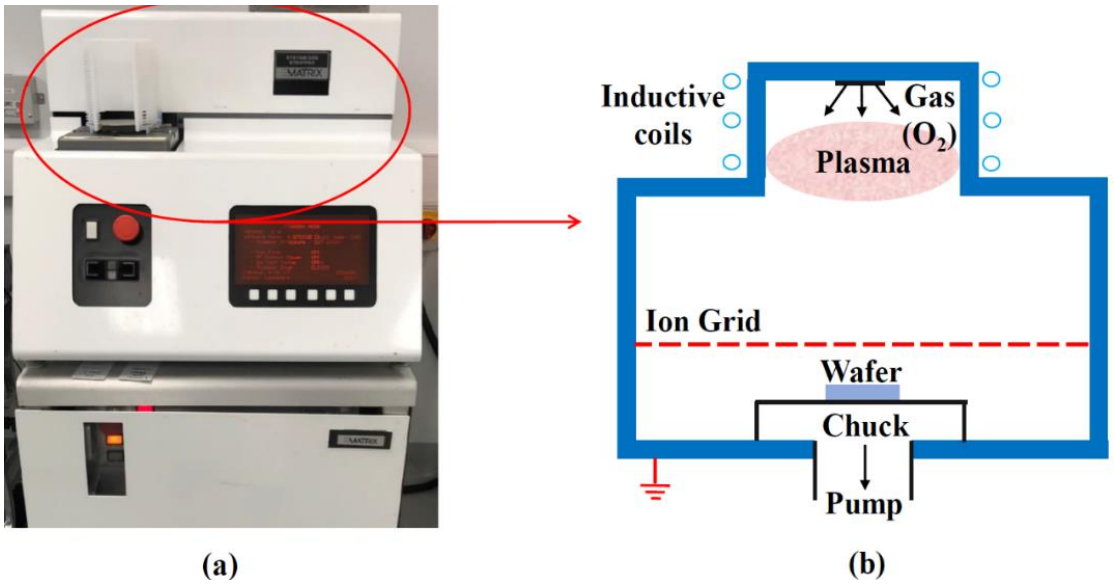

FIGURE 2.9: Image of an Asher system and (b) schematic diagram of its processing chamber.

by a Matrix Plasma asher. Figure 2.9 shows the image of the Asher system and the schematic diagram of its processing chamber. A monatomic oxygen plasma is generated by exposing oxygen gas to high power radio waves under vacuum condition in the chamber. The plasma then reacts with the organic matter under high temperatures. For pure organic materials, the byproducts of this process are carbon oxides and water vapor, which are pumped away by the vacuum pump. If there are inorganic contaminants in the organic materials, they will turn into residues known as ash, then were pumped away by the vacuum pump as well. In this work, depending on the sample conditions. The plasma ashing process is performed under 150 or 250 °C [8].

2.1.3 Formation of metal contacts

The formation of metal contacts for both p- and n-type III-nitride materials is an extremely important step to fabricate a high-quality μLED device. Generally, there are two type of metal contacts for metal-semiconductor contacts, which are

Schottky barrier contact and ohmic contact. Figure 2.10 (a) shows the current-voltage characteristics of these contacts. The Schottky barrier contact is a metal-semiconductor contacts have a large potential barrier height. It means that Schottky contact is a rectifying junction with a high resistance. The ohmic contact is a metal-semiconductor contact have no potential barrier exists between the metal-semiconductor interface. It means that an ideal ohmic contact is a non-rectifying junction with a low resistance [9]. Thus, the current-voltage characteristic of an ideal ohmic contact is linear and symmetric under forward and reverse bias. In theory, the contact resistance of an ohmic contact is much lower than the one of the semiconductor layer, since the voltage drop across it is much small than the one across the semiconductor layer. Therefore, it is essential to form ohmic contacts for III-nitride optoelectronic devices. The creation of ideal ohmic contacts to n-type GaN has been demonstrated [9]. However, it is relatively difficult to achieve an ideal ohmic contact with a low specific contact resistivity. All the contacts to p-type GaN in this work have the characteristics of the Schottky barrier contact and ohmic contact. So, it is named as quasi-ohmic contact. Figure 2.10 (b) shows a current-voltage characteristic of a single violet μLED with quasi-ohmic contact used this work. In order to form the metal-semiconductor contacts, different metals have been deposited on the treated surface of the III-nitride material in this work. Furthermore, in order to reduce the specific contact resistivity, a thermal annealing process is applied on the sample after metal deposition. The follow sections will give a brief introduction about these technologies.

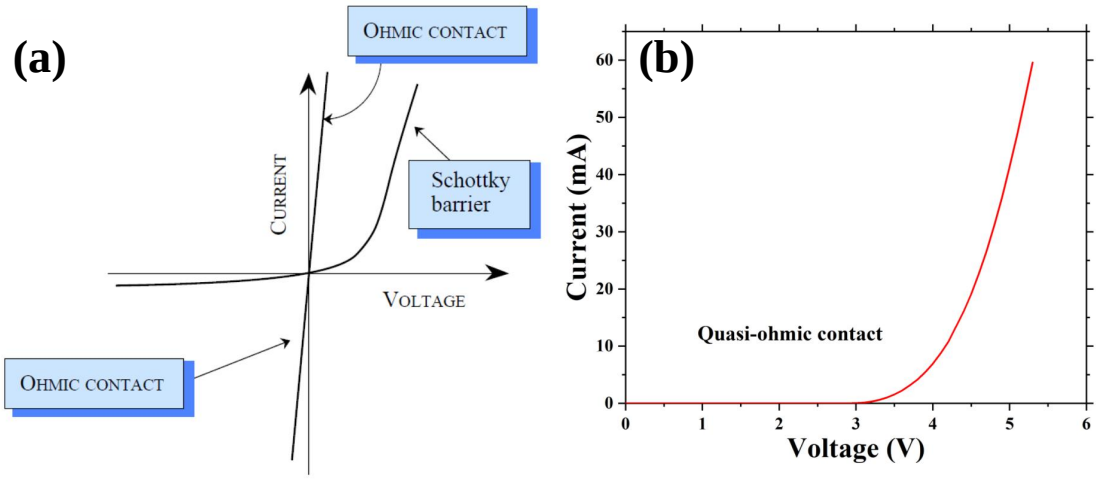

FIGURE 2.10: Schematic of (a) current-voltage characteristic of schottky barrier contact and ohmic contact, (b) measured current-voltage characteristic of a single violet μLED with quasi-ohmic contact. After [10]

Metal deposition

For p-type III-nitride material, a Pd layer with a thickness of 100 nm is used in this work as a p-type metal contact and reflective mirror for LEDs with flip-chip configurations [7]. This Pd layer is deposited in a vacuum chamber by an electron-beam evaporator (E-beam) system. The operating pressure of the E-beam system is below 7.5×10^{-5} Torr so as to achieve a high quality metal layer. The image of the E-beam system and the schematic diagram of its processing chamber are shown in figure 2.11. The pressure in the processing chamber can be detected and monitored by a vacuum monitor. During the system operating, a high electric current heats a tungsten filament, which then emits electrons to the target metal material under the control of a magnetic field. The target metal is heated by the electron beam and melted, and eventually turned into metal vapour. As a result, the surface of the sample is coated by the metal vapour and thus a p-type metal contact is formed. A crystal monitor in the chamber is used to measure the thickness of the deposited metal. During the whole process, the holder (crucible) of the target metal is cooled by cooling water in order to protect it from the high temperature damage.

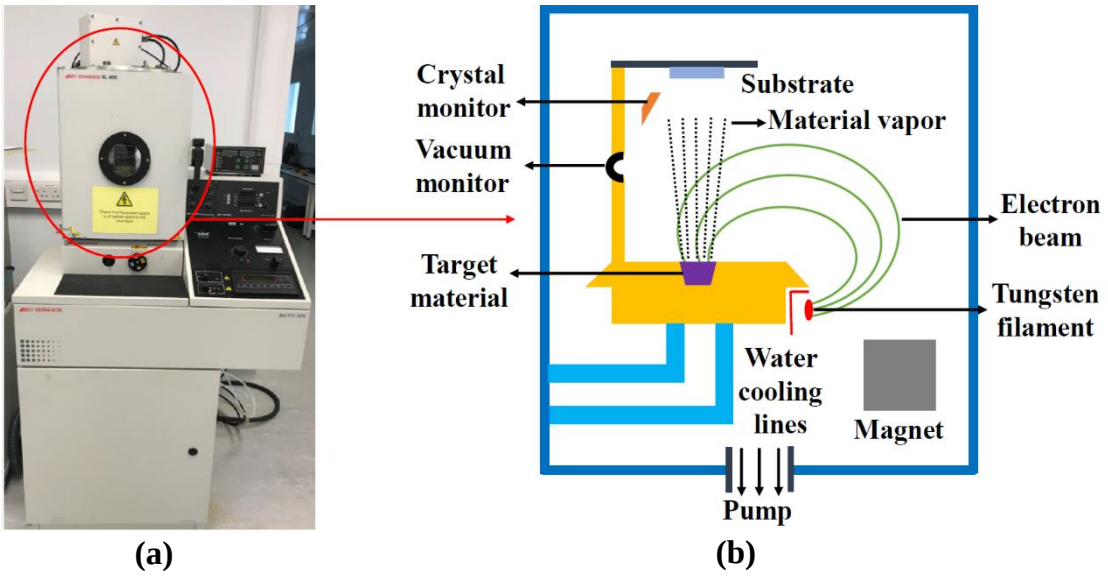

FIGURE 2.11: (a) Image of a E-beam system and (b) schematic diagram of its processing chamber.

For n-type III-nitride material, a Ti/Au bilayer with thickness of 50 nm/300 nm, which acts as the n-type metal contact and an additional reflector, is deposited on the material surface. In this work, this bilayer is deposited by a magnetron sputter system in a high vacuum chamber. The operating pressure in the chamber is under 1×10^{-6} Torr. Figure 2.12 shows the image of the magnetron sputter system and the schematic diagram of its processing chamber. The positively charged Ar ions are produced by the injected Ar gas in the chamber. Then, under a strong electric field, these positively charged Ar ions are accelerated towards the target metal which is mounted on a plate with negatively biased. As a result, the target metal is bombarded by these Ar ions, and then sputtered and deposited to the sample surface to form an n-type contact. Figure 2.13 illustrates an optical image of a sample treated by metal deposition.

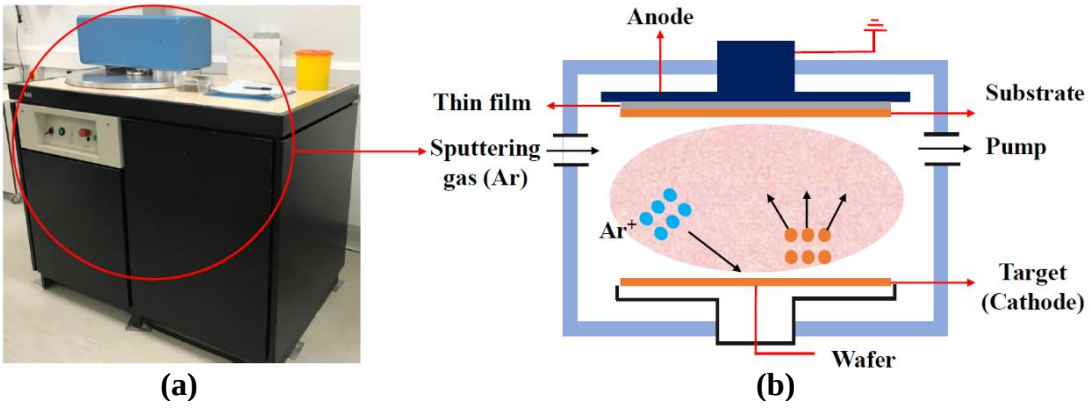

FIGURE 2.12: (a) Image of a magnetron sputter system and (b) schematic diagram of its processing chamber.

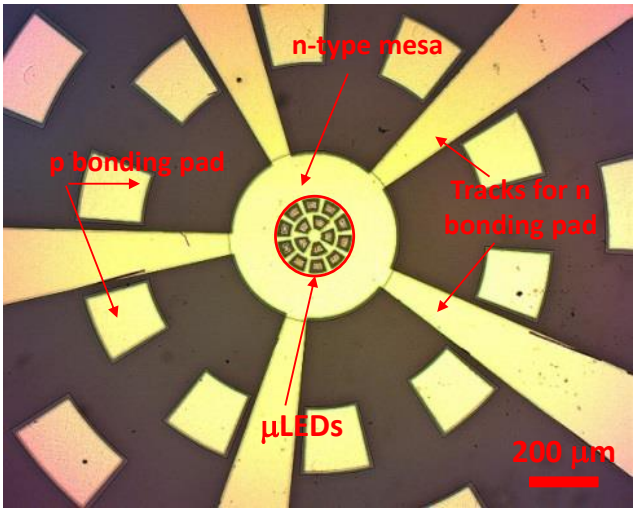

FIGURE 2.13: Image of a sample treated by metal deposition. Ti/Au layers have been deposited on the top of the p bonding pads, n-type mesa and tracks for n bonding pads.

Thermal annealing

In order to form a p-type metal contact with a low specific contact resistivity, a thermal annealing process is introduced into the fabrication process of the III-nitride μLEDs in this work. In the modern semiconductor fabrication, the annealing technology is widely used for many different purposes such as doping activation [11] and contact formation [12]. A rapid thermal anneal (RTA) system is used to performed the thermal annealing in our laboratory. This RTA system can

be operated at 1000 °C steadily. The temperature raising rate is 75 to 200 °C/s. Figure 2.14 shows the image of our RTA system and the schematic diagram of its processing chamber. As shown in the Figure, a vertical array of tungsten-halogen lamp is used to heat the target wafer uniformly. An IR pyrometer is used for monitoring the temperature of the target wafer. A gas inlet line allows the target wafer to be annealed in different ambient such as N_2 and air.

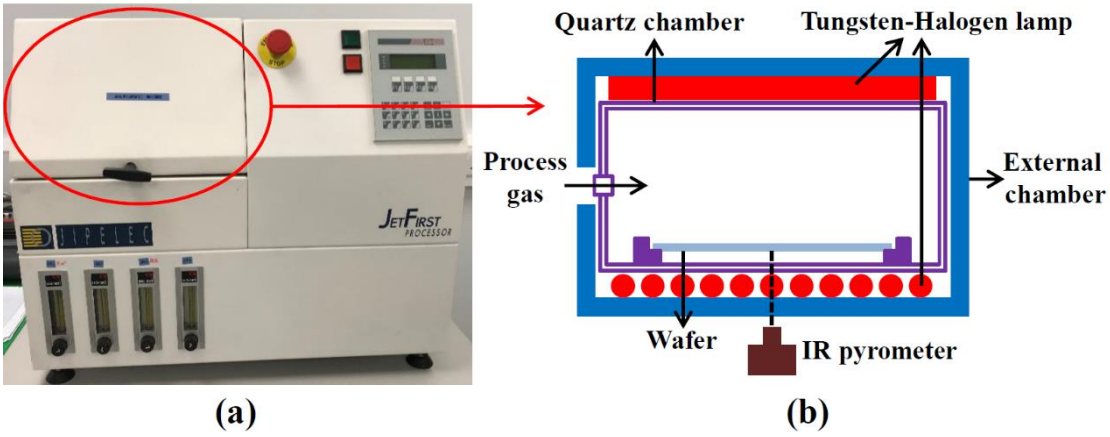

FIGURE 2.14: (a) Image of an RTA system and (b) schematic diagram of its chamber.

Thermal annealing is indispensable to gain a p-type metal contact with low specific contact resistivity for III-nitride LEDs especially for μLEDs due to their small p-type contact area as mentioned in subsection 1.3.2. For example, the Pd layer used in most of out group's works is annealed at 300 °C in a N_2 ambient. During the thermal annealing process, the residual surface oxidation layer on the top of p-type GaN layer will be removed [13]. As a result, the contact between Pd and the p-type GaN layer will be more intimate, in turn, a reduction of specific contact resistivity [14]. Moreover, a variety of Pd gallides will be formed during the thermal annealing due to the reaction between Pd and mobile excess Ga on the GaN surface. It leads to a generation of the acceptor-like Ga vacancies. As a result, the hole concentration will be increased in the near-surface region of the p-type GaN layer, thus, a reduction of specific contact resistivity.[15]

2.2 Characterization techniques of microstructured light emitting diodes

In order to optimize the fabrication process of the μLEDs and explore their applications, some characterization techniques have been used in this work. Among these techniques, the techniques used for the characterizations of electroluminescence (EL) spectrum electrical and optical properties, and modulation bandwidth play important roles. In the following subsections, these techniques will be introduced briefly.

2.2.1 Electroluminescence spectrum characterization

Figure 2.15 shows the setup of the EL spectrum measurement. As mentioned in section 2.1.3, the μLEDs used in this work are in a flip-chip configuration, which means the light emitted from the side of the polished sapphire substrate. Therefore, the EL spectrum of the μLEDs is obtained by collecting the emitted photons from the sapphire side with a fiber coupled spectrometer. The aperture of the fiber is aligned with the center of the light emitter. The spectral data is then processed by Origin software.

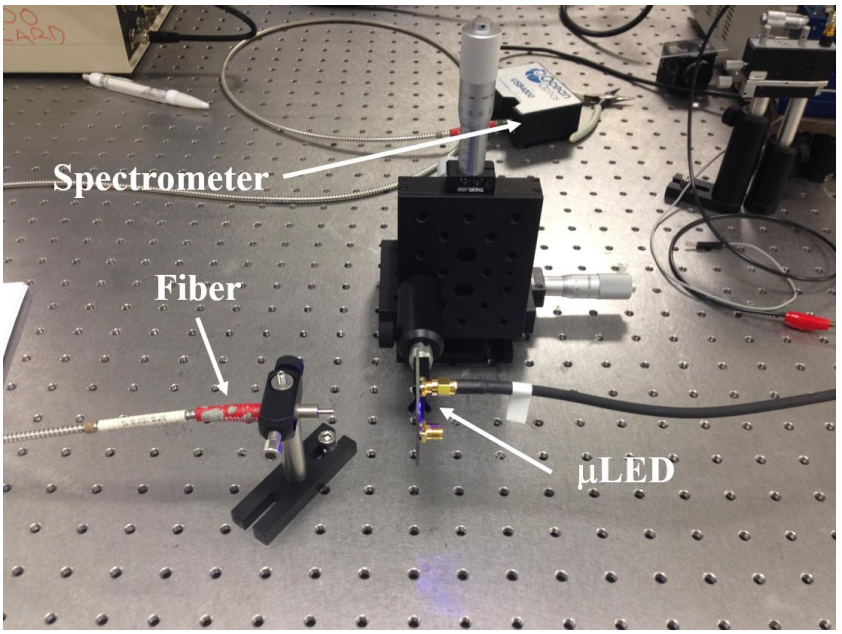

FIGURE 2.15: Image of a setup of the EL spectrum measurement.

2.2.2 Electrical and optical characterization

The main electrical and optical characteristics of μLEDs measured in this work are the current density-voltage (J-V) and optical power-current density (L-J). The fundamental principles of the J-V and L-J characteristics of a μLED are given in section 1.3. As we know, the high operating temperature of an LED could cause the degradation of it, such as the increasing of the p-contact resistance and increasing of hole concentration in p-GaN [16]. Moreover, it has been proven that the radiative and Auger recombination coefficients decrease with increasing temperature. Meanwhile, at higher carrier concentrations, the temperature dependence of radiative and Auger recombination coefficients became weaker [17]. This will lead to the poor performance of the LED. However, due to the small size of the μLEDs and thus the large surface to volume ratio, they have higher heat dissipation capability compared with larger broad-area LEDs. As a result, the μLEDs have lower junction temperatures compared with larger broad-area LEDs. The junction temperature of a 20 μm^2 diameter μLED is similar to the room temperature, while the one of a 1 mm^2 broad-area LED is approaching 100 °C under

nearly the same current density [18, 19]. Therefore, the μLEDs can be driven at very high current densities, which leads to a large output power density. In this work, the fabricated μLEDs can be divided into two kinds, unwire-bonded and wire-bonded μLEDs. The unwire-bonded μLEDs is simply just a bare chip, which the wire-bonded μLEDs is bonded to a desired Printed Circuit Board (PCB) and ready to connect with power source. In order to drive the unwire-bonded μLEDs, a probe station is used to connect them to the power source (YOGOKAWA GS610). A power meter (Thorlabs PM100A) with a photodiode power sensor (S120VC) is used to measure the electrical and optical performances in this work. Figure 2.16 illustrates the image of the power meter used in this work.

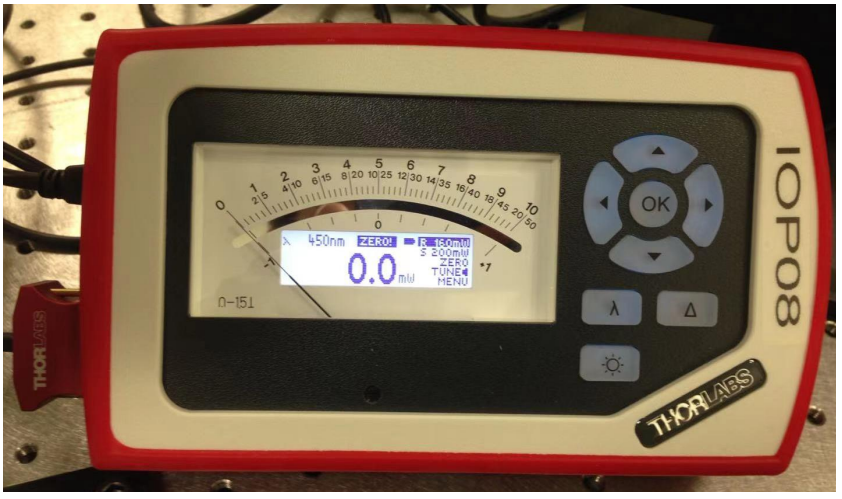

FIGURE 2.16: Image of the power meter used in this work.

2.2.3 Modulation bandwidth characterization

The modulation bandwidth of a μLED is an important parameter to estimate its performance in an optical communication system. It presents how fast this μLED can be modulated to transmit data without the distortion of the signal. The electrical-to-electrical is known as 3-dB electrical modulation bandwidth. It is defined as the frequency at which the power transmitted through the whole system has dropped by half at direct current (DC). Generally, the modulation bandwidth of LEDs, $f_{(3-dB)}$, can be expressed as:

$$f_{(3-dB)} = \sqrt{3}/2\pi\tau \tag{2.1}$$

where τ is the carrier lifetime. To measure the modulation bandwidth in our laboratory, a small-signal modulation, of fixed amplitude (75 kHz to 1 GHz), from an HP8753ES network analyser is combined with a DC bias using a bias-tee and applied to a representative μLED. The light output from the μLED is measured by a high bandwidth photoreceiver, and, meantime, the frequency response is recorded by the network analyser. Figure 2.17 shows a typical μLED frequency response curve measured early by our group. The suddenly drop of the frequency response is because of the digital nature of the CMOS driver used in the work. The unwire-bonded μLEDs is driven through a high-speed probe, and the light out of it is collected by a cage optical system as Figure 4.9 (b) shown. The differences between unwire-bonded and wire-bonded μLEDs are the way to drive them and collect the light out from them.

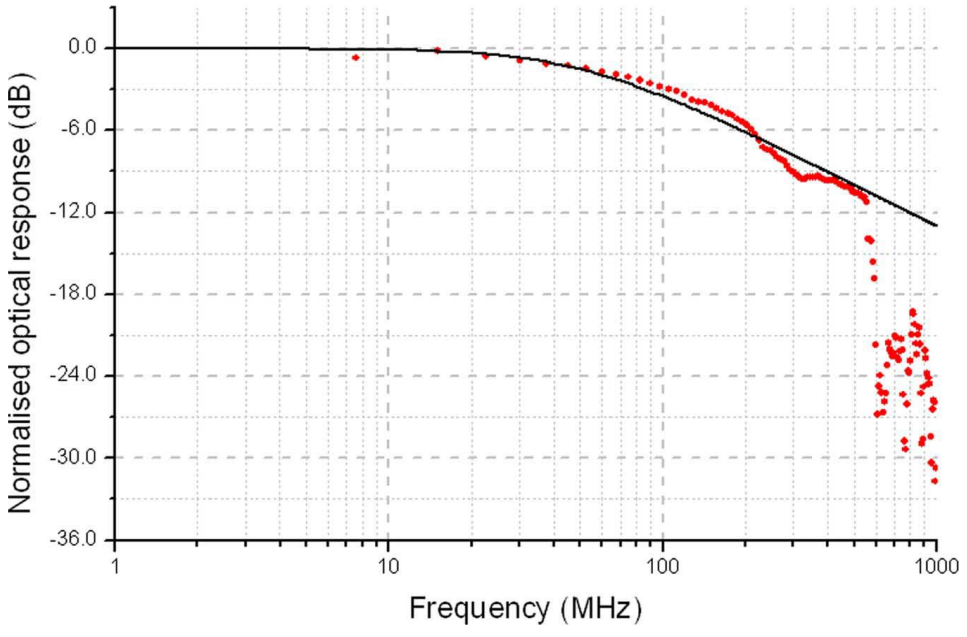

FIGURE 2.17: A typical μLED frequency response curve. The measured data is plotted in red. The black curve is the fitting curve obtained from the measured data. After [20].

2.3 Summary

In summary, this chapter presents the main fabrication processes of the III-nitride μLEDs including pattern definition, pattern transfer, and formation of metal contact. The operating principles of these processes are also presented briefly. These processes are important for fabricating fully functional III-nitride μLEDs. In section 2.2, three techniques used for characterizing μLED are introduced. The techniques to characterize the EL spectrum, electrical and optical properties and modulation bandwidth of μLEDs. These techniques will be used in later chapters.

References

[1] J. J. D. McKendry, R. P. Green, A. E. Kelly, Z. Gong, B. Guilhabert, D. Massoubre, E. Gu, and M. D. Dawson. High-speed visible light communications using individual pixels in a micro light-emitting diode array. *IEEE Photonics Technology Letters*, 22(18):1346–1348, 2010.

[2] J. J. D. McKendry, D. Tsonev, R. Ferreira, S. Videv, A. D. Griffiths, S. Watson, E. Gu, A. E. Kelly, H. Haas, and M. D. Dawson. Gb/s single-LED OFDM-based VLC using violet and UV gallium nitride μLEDs. In *Summer Topicals Meeting Series (SUM), 2015*, pages 175–176. IEEE, 2015.

[3] R. X. G. Ferreira, E. Xie, J. J. D. McKendry, S. Rajbhandari, H. Chun, G. Faulkner, S. Watson, A. E. Kelly, E. Gu, R. V. Penty, I. H. White, D. C. O'Brien, and Dawson. M. D. High bandwidth GaN-based micro-LEDs for multi-Gb/s visible light communications. *IEEE Photonics Technology Letters*, 28(19):2023–2026, 2016.

[4] S. Franssila. *Introduction to microfabrication*. John Wiley & Sons, 2010.

[5] Emission spectrum of the HBO 100 high pressure mercury short-arc lamp. `http://zeiss-campus.magnet.fsu.edu/articles/lightsources/mercuryarc.html`, Accessed 2021-06-08.

[6] S. M. Sze and K. K. Ng. Physics and properties of semiconductors—A review. *Physics of semiconductor devices*, 3, 2006.

[7] E. Xie. *High performance microstructured light emitting diodes: mechanisms and processes*. PhD thesis, University of Strathclyde, 2013.

[8] T. R. Nerurkar. *Design of experiments on a semiconductor plasma ashing process: methods and analysis*. PhD thesis, Massachusetts Institute of Technology, 2016.

[9] T. V Blank and Y. A Gol'Dberg. Mechanisms of current flow in metal-semiconductor ohmic contacts. *Semiconductors*, 41(11):1263–1292, 2007.

[10] Current and voltage of contacts. `https://inderjitsingh87.weebly.com/electronic-devices-2016.html`, Accessed 2021-10-26.

[11] S. J. Pearton, J. C. Zolper, R. J. Shul, and F. Ren. GaN: Processing, defects, and devices. *Journal of Applied Physics*, 86(1):1–78, 1999.

[12] J. K. Sheu, Y. K. Su, G. C. Chi, W. C. Chen, C. Y. Chen, C. N. Huang, J. M. Hong, Y. C. Yu, C. W. Wang, and E. K. Lin. The effect of thermal annealing on the Ni/Au contact of p-type GaN. *Journal of Applied Physics*, 83(6):3172–3175, 1998.

[13] E. Xie, M. Stonehouse, R. Ferreira, J. J. D. McKendry, J. Herrnsdorf, X. He, S. Rajbhandari, H. Chun, A. V. N. Jalajakumari, O. Almer, G. Faulkner, I. M. Watson, E. Gu, R. Henderson, D. C. O'Brien, and Dawson. M. D. Design, fabrication, and application of GaN-based micro-LED arrays with individual addressing by N-electrodes. *IEEE Photonics Journal*, 9(6):1–11, 2017.

[14] C. Kim, J. Jang, J. Shin, J. Choi, J. Seo, W. Kim, J. Park, J. O. Seo, S. Leem, B. H. Seung, K. B. Lee, and Y. J. Park. Temperature-driven crystalline ordering and Ohmic contact formation of PdAu layers on p-type GaN. *Physical Review B*, 64(11):113302, 2001.

[15] T. Massalski and P. R. Subramanian. *Hf (Hafnium) Binary Alloy Phase Diagrams*. ASM international Cleveland, 1990.

[16] E. F. Schubert. *Light-Emitting Diodes*. Cambridge University Press, 2006.

[17] P. Tian, J. J. D. McKendry, J. Herrnsdorf, S. Watson, R. Ferreira, I. M. Watson, E. Gu, A. E. Kelly, and M. D. Dawson. Temperature-dependent efficiency droop of blue InGaN micro-light emitting diodes. *Applied Physics Letters*, 105(17):171107, 2014.

[18] M. Meneghini, A. Tazzoli, G. Mura, G. Meneghesso, and E. Zanoni. A Review on the Physical Mechanisms That Limit the Reliability of GaN-Based LEDs. *IEEE Transactions on Electron Devices*, 57(1):108–118, 2010.

[19] P. Tian, A. Althumali, E. Gu, I. M. Watson, M. D. Dawson, and R. Liu. Aging characteristics of blue InGaN micro-light emitting diodes at an extremely high current density of 3.5 kA cm-2. *Semiconductor Science and Technology*, 31(4):045005, mar 2016.

[20] J. J. D. McKendry, D. Massoubre, S. Zhang, B. R. Rae, R. P. Green, E. Gu, R. K. Henderson, A. E. Kelly, and M. D. Dawson. Visible-Light Communications Using a CMOS-Controlled Micro-Light- Emitting-Diode Array. *Journal of Lightwave Technology*, 30(1):61–67, 2012.

Chapter 3

Free-space optical communication systems and related modulation schemes

The radio frequency (RF) wireless communication technology is facing serious challenges as the demands of communication services are increasing rapidly. In 2020, more than 26 billion networked devices are expected to load into the current RF network [1]. Due to this issue, free-space optical communication that utilizes LEDs for both illumination and data transmission has gained great interest in recent years. Besides huge energy saving on general lighting, free-space optical communication also offers sufficient unlicensed bandwidth in the visible light spectrum and, in turn, a solution to the wireless data traffic congestion caused by the limited availability of radio frequency spectrum [2, 3]. The first LED based free-space optical communication system was reported in 1999 [4]. In a free-space optical communication system, the ways to encode digital data in a waveform are the modulation schemes. There are three conventionally used modulation schemes, which are on-off keying (OOK), pulse amplitude modulation (PAM), and orthogonal frequency division multiplexing (OFDM). In this chapter, the setup of the

LED based free-space optical communication system and these three modulation schemes are introduced.

3.1 Setup of a free-space optical communication system

Figure 3.1 shows (a) Schematic and (b) optical image of a typical free-space LED optical communication system. As the figure shows, a signal is generated by an arbitrary waveform generator (AWG) and amplified by an amplifier. The amplified signal is then combined with a DC bias by using a bias-tee to drive an LED. AWG is an electronic equipment which can generate different types of electrical waveforms. The optics is used to focus the output signal from the LED into a photoreceiver. A digital oscilloscope is used to capture the output signal. The captured signals are processed by the MATLAB®. There are two different kinds of photoreceivers, i.e. P-I-N photodiode (a diode with a wide, undoped intrinsic semiconductor region between a p-type semiconductor and an n-type semiconductor region, known as PIN) detector and avalanche photodiode (APD) detector.

A PIN detector contains a photodiode, which is composed of a p-i-n junction. In the p-i-n junction, a reverse bias (below the breakdown voltage) is applied to increase the depletion layer width, decreasing the junction capacitance and increasing the response time. When a photon with sufficient energy reaches the depletion region of the p-i-n diode, an electron-hole pair is generated, and then creates a photo current via the photoelectric effect corresponding to the unit gain (G=1).

The operating principle of the APD detector is similar to the PIN detector. Both PIN detector and APD detector have the same mechanism for the generating of a photo current. However, compared with the PIN detector, the APD detector has a function to multiply the generated carriers. In order to accomplish this

function, the APD detector is composed by a p-n junction with an additional avalanche layer operating in reverse voltage(below the breakdown voltage). When the electron-hole pair generated in the depletion region under a reverse voltage to the p-n junction, the high electric field increase the kinetic energy of the carrier to collide with the crystal lattice. In turn, new electron-hole pairs are generated via ionisation. Furthermore, these electron-hole pairs will further create additional electron-hole pairs in a chain reaction of ionisation to enable multiplying the photo current at the junction by a large factor. This factor is known as gain, which is proportional to electric field applied. The gain of an APD detector can go up to 100. However, increasing the gain will result in a decrease of the capacitance and a increase of the dark current, which leads to a high noise. Therefore, the APD detector requires precise driving circuitry to compensate the gain factor for changes in temperature and light exposure due to the high non-linear feature of itself.

In this system, the digital data is encoded in a waveform through modulation schemes and then applied on the LED. The waveform was delivered to the receiver through the variations of the emitted light intensity of the LED. Finally, the received waveform is decoded into digital data and compared with the sent data. If there is any bit of the data does not match the sent data, a bit error rate (BER) is generated. The BER is the ratio between the number of unmatched bits and the total transferred bits. The firm rules of acceptable BER in a communication link has been set by Institute of Electrical and Electronics Engineers (IEEE). In order to get a high-quality data transmission, the BER has to be below 3.8×10^{-3} for forward error correction (FEC). FEC is a technique that allows the error-correcting code or channel coding algorithms to partially or totally recover the lost bits at the receiver side by using a 7 % data rate overhead to include redundant information. To estimate the data transmission rate and evaluate an LED as a transmitter of a free-space optical communication system, it is of paramount importance to know Shannon–Hartley theorem [5]. According to Shannon–Hartley

theorem, the maximum data transmission rate over a communication channel, C, can be formulated by:

$$C = B \log_2(1 + S/N) \tag{3.1}$$

where B is the channel bandwidth; S is the average received signal power over the entire bandwidth; N is the average power of the noise and interference; and thus S/N is the signal-to-noise ratio (SNR). The SNR strongly depends on the optical power produced by LEDs. This theorem indicates that, for an LED based free-space optical communication system, the maximum data transmission rate is determined by the 3-dB modulation bandwidth and the optical output power of LEDs. The impedance matching is to design the impedances of source and load to maximize power transfer or minimize signal reflection [6]. It is also quite important to achieve high speed data communication. The mismatching of the impedance will leads to partial reflection of the signal and reduce power gain in the channel [7]. Moreover, the impedance mismatching is also saturating the modulation bandwidth of the LEDs [8], which in turn, reduces the data transmission rate. The impedance of commercial available electrical components is generally 50 Ω. However, it is difficult to match the impedance of a μLED with other components, since the value of the capacitance of a μLED is negative under operation condition [9]. The impedance of a μLED and its effect on the modulation bandwidth of a μLED and μLED based communication system still need further study. In this work, all the modulation bandwidth and data transmission measurements are performed without impedance matching.

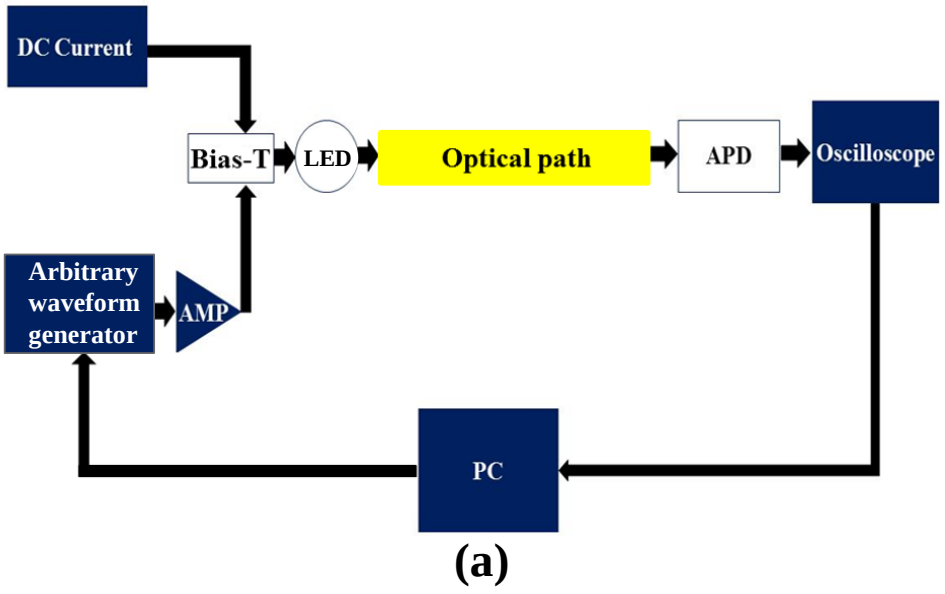

(a)

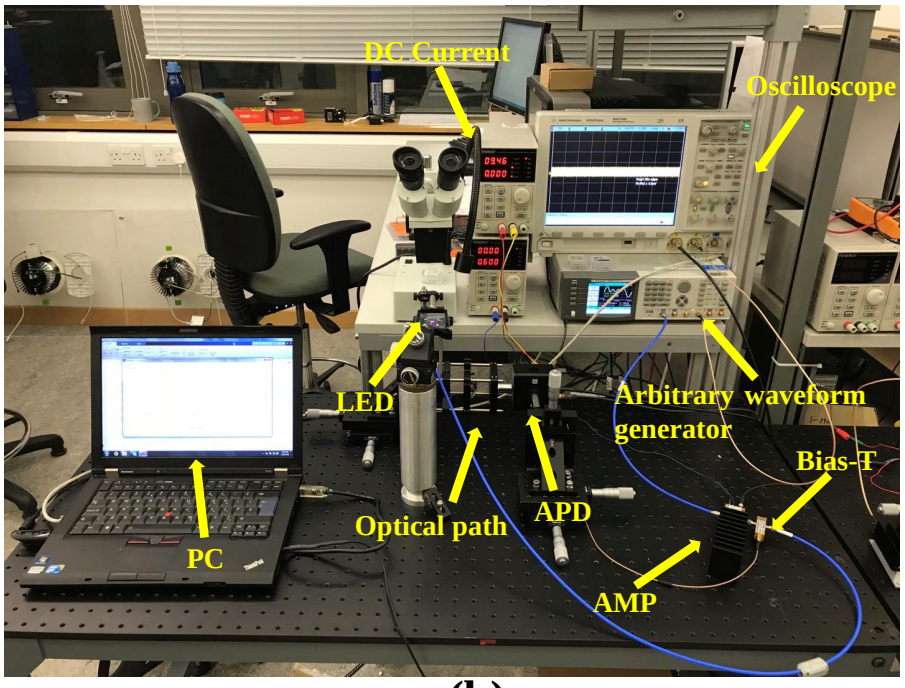

(b)

FIGURE 3.1: (a)Schematic and (b) optical image of a LED based optical communication system.

3.2 Modulation schemes

3.2.1 On-off keying

OOK is the simplest single carrier modulation scheme in the free-space optical communication system [3, 10]. It has been widely used in many communication applications, thanks to the simplicity of its implementation and its ability to present the system performance visually.

For an OOK based optical communication system, the information is first encoded into digital pulses, which only have two different levels. A pulse is presenting as one, which is on state. An absence of the pulse is presenting as zero, which is off state. These digital pulses are then transmitted into light pulses by LEDs, and sent to the receiver. Since the LED is used as a transmitter, a suitable DC-bias needs to be set. The pulse above the DC-bias is considered as a positive pulse, which means an on state. The pulse below the DC-bias is considered as negative pulses, which means an off state. Figure 3.2 shows the basic waveform under OOK modulation scheme.

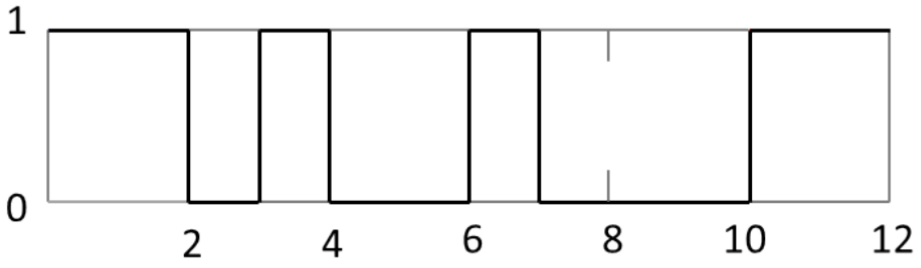

FIGURE 3.2: Basic waveform of a OOK modulation scheme. After [10].

As mentioned above, OOK could present the system performances visually, known as eye diagram. Figure 3.3 demonstrates the eye diagrams of a deep UV μLED operating at different data transmission rates under the OOK modulation

scheme in a free-space optical communication system. The details of the experiment will be given in Chapter 6, section 6.3. In the figure, the open space between the top level and bottom level is defined as the eye. The size of the opening eye decides the quality of the data transmission link. The ideal clear opening eye should look like a square or rectangle. As figure 3.3 shows, the eye is becoming closed when the data transmission rate increases. This means the transmission speed is reaching the limit of the transmitter or the detector used. As a result, the BER is increasing.

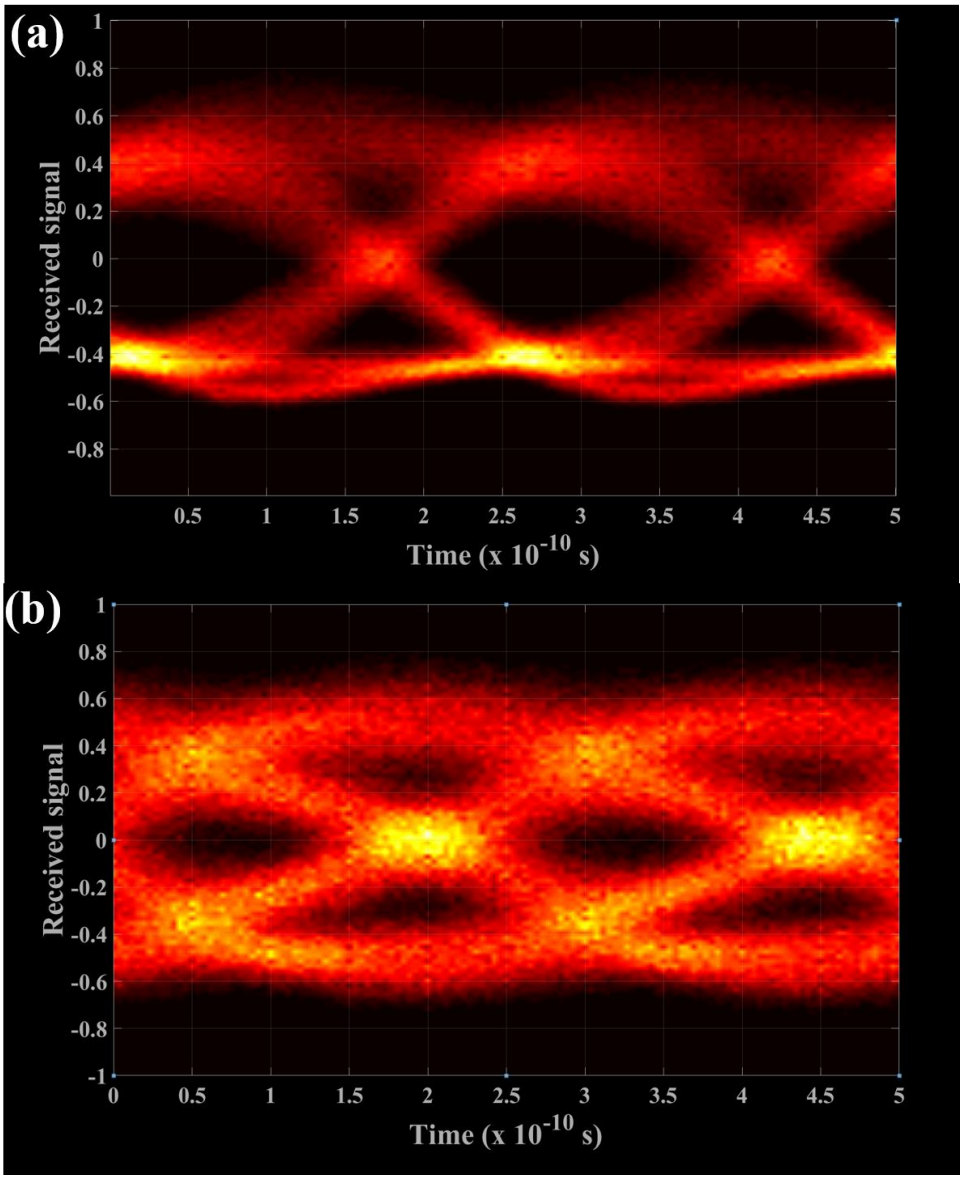

FIGURE 3.3: Eye diagrams at (a) 571 Mbps and (b) 800 Mbps of a deep UV μLED under OOK in a free-space optical communication system. After [11].

3.2.2 Pulse amplitude modulation

PAM is also a single carrier modulation scheme [3, 10]. Its working principle is similar to OOK, which encodes information into the waveform presenting different binary words based on the amplitude change. In a PAM based Free-space optical communication system, the amplitude of the signal can be divided into multiple

levels. Each level contains a unique binary word. Therefore, by exploring the number of levels in PAM, the length of binary words increases. It means that the number of bits sent per unit of time increases. In turn, the data transmission rate increases. The limitation of the number of levels is strongly depended on available SNR in the applied free-space optical communication system. The non-linear optical response from LEDs could cause poor performance of PAM. Moreover, the abnormalities in frequency response also have a huge influence on the performance of PAM. Therefore, in order to get the best performance of the PAM based free-optical communication system, a complex equalizer at the receiver is necessary [3]. Figure 3.4 shows the Basic waveform of a PAM modulation scheme.

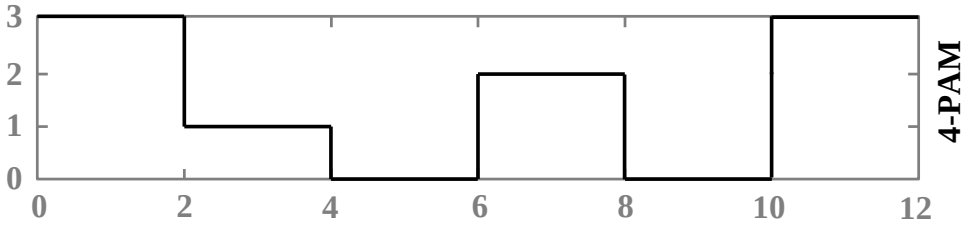

FIGURE 3.4: Basic waveform of a PAM modulation scheme. After [10]

3.2.3 Orthogonal frequency division multiplexing

In a single carrier modulation scheme such as OOK and PAM, the intersymbol interference (ISI) caused by the amplitude and delay distortions from the communication channel can reduce the BER significantly. Moreover, the influence of ISI on BER in single carrier modulation scheme would become more pronounced with the increase of the data transmission rate. Therefore, a computationally complex equalizer, such as feed-forward equalizer, decision feedback equalizer, Volterra non-linear equalizer and machine learning based equalizer, would be needed for high speed communication. Unlike the single tap equalizer, which use previous detected symbol to equalize based on a delay line, these computationally complex equalizers have higher requirements in the design, such as filters [12]. Therefore, a cost effective way to simplify the equalizer is to apply the OFDM scheme with a single

tap equalizer [3, 11]. Unlike the single carrier modulation schemes, OFDM encode information into digital data in the frequency domain instead of the time domain. There are multiple variants of OFDM which have been reported for optical communication. Figure 3.5 (a) presents the schematic of the OFDM communication system used in this work. A pseudo-random bit sequence (PRBS) is generated by the MATLAB®. The signal is then modulated by quadrature amplitude modulation (QAM). QAM is the modulation method which can convey two analog signals or two digital bit sequences by shifting 90 ° of the phase of them and change their amplitudes. Thus, the bit sequence is modulated into M-ary QAM (M-QAM) symbols, where M is the constellation order, which is evaluated from available SNR in the system. After that, an adaptive bit and energy loading technology are applied to load the different constellation sizes on the subcarriers based on the available SNR in the system. The high M-QAM level is loaded into high SNR sub-carriers, while the low M-QAM is loaded into low SNR sub-carriers. This technology significantly increases the efficiency of data transmission. Then, an inverse fast Fourier transformation (IFFT) is used to combine and multiplex these sub-carriers into a serial time domain output. Figure 3.5(b) demonstrates an example of two sub-carriers multiplexing into an OFDM single. In order to shift the negative OFDM samples to positive, there is a DC bias imposed in the system. Finally, the received waveform is decoded by fast Fourier transform, single-tap equalization and QAM demodulation and then the BER and data transmission rate are evaluated.

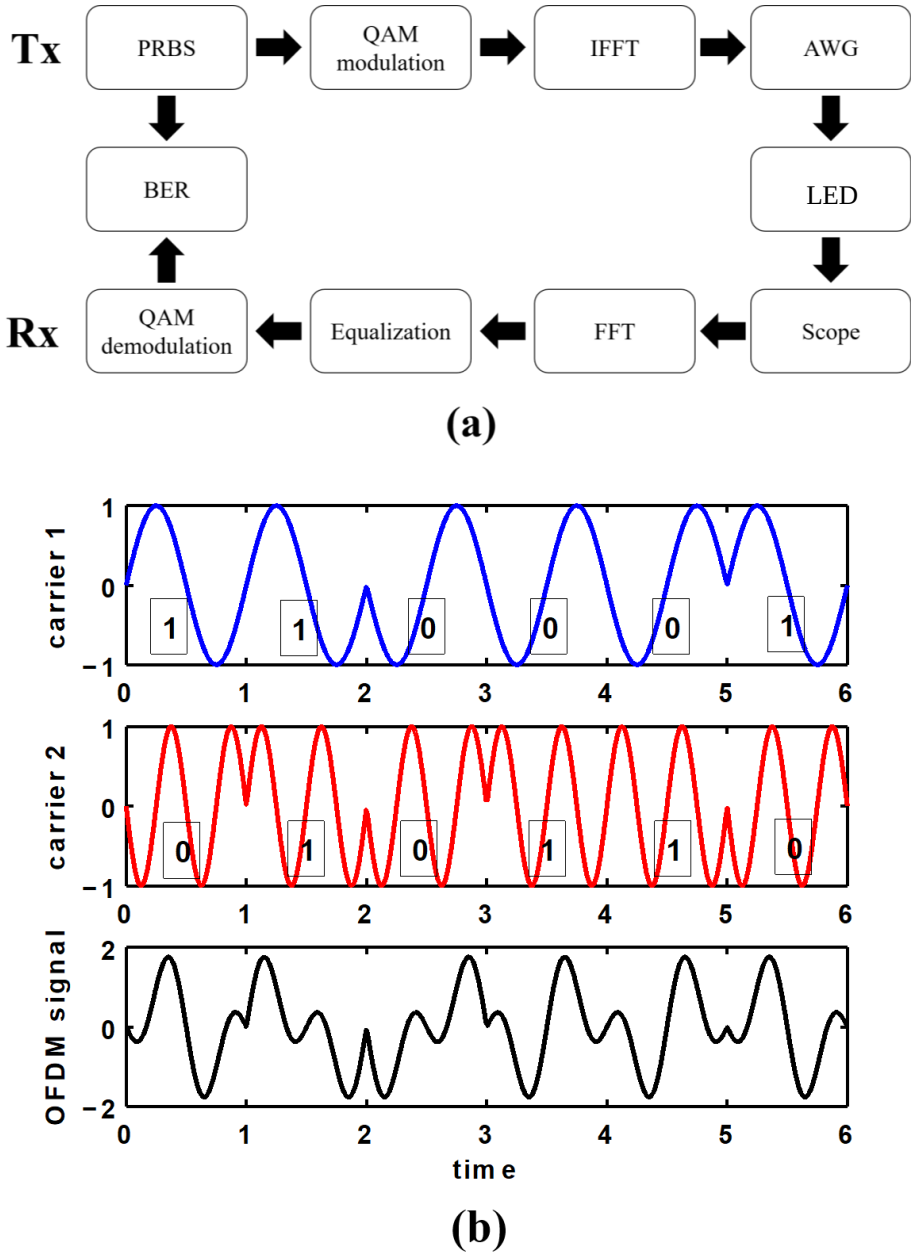

FIGURE 3.5: (a) The schematic of the OFDM transmitter and receiver, and (b) example of two sub-carriers multiplexing into an OFDM signal. After [10].

3.3 Summary

In this chapter, the setup of an LED based free-space optical communication system is introduced in section 3.1. The following sections briefly present the

working principle of three different modulation schemes, including OOK, PAM, and OFDM. Besides the general working principle, the advantages and drawbacks of these modulation schemes are commented. These modulation schemes will be used for μLEDs based free-space optical communications as shown in later chapters.

References

[1] Cisco Visual Networking Index. Cisco Visual Networking Index: The Zettabyte Era—Trends and Analysis. *White Paper*, 2015.

[2] R. X. G. Ferreira, E. Xie, J. J. D. McKendry, S. Rajbhandari, H. Chun, G. Faulkner, S. Watson, A. E. Kelly, E. Gu, R. V. Penty, I. H. White, D. C. O'Brien, and Dawson. M. D. High bandwidth GaN-based micro-LEDs for multi-Gb/s visible light communications. *IEEE Photonics Technology Letters*, 28(19):2023–2026, 2016.

[3] M. S. Islim, R. X. Ferreira, X. He, E. Xie, S. Videv, S. Viola, S. Watson, N. Bamiedakis, R. V. Penty, I. H. White, A. E. Kelly, E. Gu, H. Hass, and M. D. Dawson. Towards 10 Gb/s orthogonal frequency division multiplexing-based visible light communication using a GaN violet micro-LED. *Photonics Research*, 5(2):A35–A43, 2017.

[4] G. Pang, T. Kwan, Chi-Ho Chan, and Hugh Liu. LED traffic light as a communications device. In *Proceedings 199 IEEE/IEEJ/JSAI International Conference on Intelligent Transportation Systems (Cat. No.99TH8383)*, pages 788–793, 1999.

[5] C. E. Shannon and W. Weaver. The mathematical theory of communication, 117 pp. *Urbana: University of Illinois Press*, 1949.

[6] Bai M and Liang H. The analysis of impedance matching problem in RF circuit design. In *2010 International Forum on Information Technology and Applications*, volume 1, pages 350–353. IEEE, 2010.

[7] R. Araneo, S. Celozzi, and G. Lovat. Design of impedance matching couplers for power line communications. In *2009 IEEE International Symposium on Electromagnetic Compatibility*, pages 64–69. IEEE, 2009.

[8] P. Tian, X. Liu, S. Yi, Y. Huang, S. Zhang, X. Zhou, L. Hu, L. Zheng, and R. Liu. High-speed underwater optical wireless communication using a blue GaN-based micro-LED. *Opt. Express*, 25(2):1193–1201, Jan 2017.

[9] W. Yang, S. Zhang, J. J. D. McKendry, J. Herrnsdorf, P. Tian, Z. Gong, Q. Ji, I. M. Watson, E. Gu, M. D. Dawson, L. Feng, C. Wang, and X. Hu. Size-dependent capacitance study on InGaN-based micro-light-emitting diodes. *Journal of Applied Physics*, 116(4):044512, 2014.

[10] S. Rajbhandari, J. J. D. McKendry, J. Herrnsdorf, H. Chun, G. Faulkner, H. Haas, I. M. Watson, D. O'Brien, and M. D. Dawson. A review of gallium nitride LEDs for multi-gigabit-per-second visible light data communications. *Semiconductor Science and Technology*, 32(2):023001, Jan 2017.

[11] X. He, E. Xie, M. S. Islim, A. A. Purwita, J. J. D. McKendry, E. Gu, H. Haas, and M. D. Dawson. 1 Gbps free-space deep-ultraviolet communications based on III-nitride micro-LEDs emitting at 262nm. *Photon. Res.*, 7(7):B41–B47, Jul 2019.

[12] H. Zhou, Y. Li, Y. Liu, L. Yue, C. Gao, W. Li, J. Qiu, H. Guo, X. Hong, Y. Zuo, and J. Wu. Recent advances in equalization technologies for short-reach optical links based on PAM4 modulation: A review. *Applied Sciences*, 9(11):2342, 2019.

Chapter 4

Development and application of series-biased micro-structured light emitting diodes

The work presented in this chapter focuses on the development of series-biased III-nitride μLEDs and their applications in VLC. Our previous research works have demonstrated the VLC systems using a single blue or a violet μLED as a light source for data transmission. However, the optical power of a single μLED is quite low, which limits the performances of the data transmission rate and transmission distance significantly. In order to solve this problem, a new series-biased μLED array is introduced. Such series-biased μLED is able to generate much higher optical power without sacrificing too much modulation bandwidth in comparison with the single μLED. As a result, the data transmission rate and transmission distance of the VLC systems using series-biased μLED light sources increased dramatically.

4.1 Series-biased blue micro-structured light emitting diodes

4.1.1 Single blue μLED based VLC systems

VLC is an attractive technology, which opens up a wider, license-free, visible region of the electromagnetic spectrum for wireless optical communications, the off-the-shelf LEDs can be used as a light source in VLC systems [1]. However, such LEDs only have 10-20 MHz 3-dB electrical modulation bandwidths. As a result, the data transmission rate of the VLC system based on off-the-shelf LEDs is relatively low. It has been shown that even with complex modulation schemes, parallel data transmission and equalization technologies, the maximum data transmission rate of the VLC systems using off-the-shelf LEDs is 1 Gbps [2]. To overcome this issue, novel III-nitride based LEDs are developed and introduced into VLC systems. These new LEDs have dimensions less than 100 by 100 μm^2 and are known as micro-structured LEDs or μLEDs. μLEDs can be operated at higher current densities, enabling significantly higher modulation bandwidth [3]. This makes μLEDs promising candidates for VLC applications. In 2014, by using a single μLED, a VLC data transmission rate of 3 Gbps was achieved [4]. In 2016, a new μLED structure of was demonstrated [3]. Figure 4.1 shows the optical image of such a μLED array consisting of 15 individual trapezoidal shape blue μLEDs. It contains 5 inner and 10 outer μLEDs with 435 μm^2 and 465 μm^2, respectively. For inner μLEDs, it can be driven up to 19.5 kA/cm^2 current density, producing an optical power density of 655 W/cm^2 (2.7 mW). Driven at such a high current density, these blue μLEDs show a very high modulation bandwidth (830 MHz). By using this blue μLED as a light source, VLC data transmission rates of 1.7, 3.4 and 5 Gbps are achieved under OOK, PAM and OFDM modulation schemes, respectively [3]. These were the highest data transmission rates reported at that time.

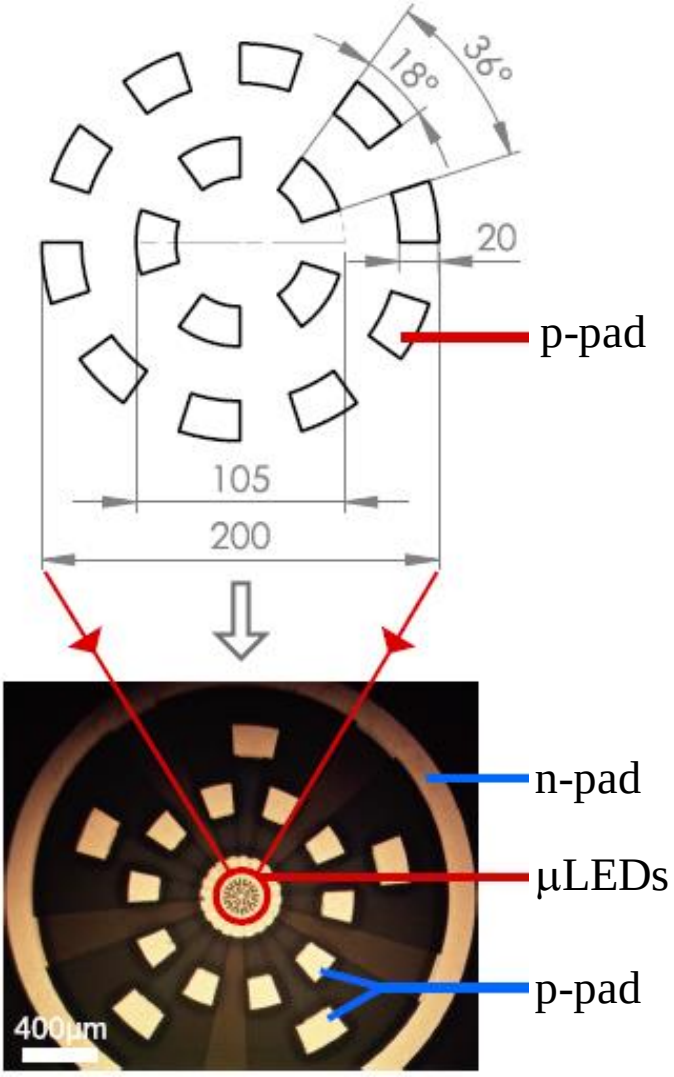

FIGURE 4.1: Schematic of the blue μLED. After [3].

4.1.2 Development of series-biased blue micro-structured light emitting diodes for VLC applications

As mentioned above, the data transmission rate and data transmission distance of a VLC system with a single μLED light source is strongly limited by the low optical power of the single μLED. To the best of our knowledge, the highest reported data transmission rate of a VLC system using a single blue μLED is 5 Gbps under an OFDM modulation scheme [3]. However, the data transmission

distance of that system is only 0.3 m due to the relatively low optical power of the single blue μLED. Thus, the low optical power of the single blue μLED strongly restricts its wider use for long distance communications. It is worth to mentioned that the definitions for long distance on different communication applications are various. For example, the long distance on laser communication application or deep ultraviolet light sources based non-line-off-sight communication application normally means over hundred meters. Here, for μLED based VLC applications in this work, the long distance means over 5 m. In this work, series-biased blue μLED arrays with high modulation bandwidth and high optical power were developed. Based on these new devices, a fast speed free space VLC system for long distance applications is demonstrated. The blue series-biased μLED arrays were fabricated on a commercial blue III-nitride LED wafer. The LED epitaxial structure consists of a 3.4 μm thick undoped GaN buffer layer, a 2.6 μm thick n-typer GaN layer, 11 periods of InGaN/GaN (2.8 nm/13.5 nm) quantum wells, a 30 nm thick p-type AlGaN electron blocking layer and a 160 nm thick p-type GaN layer. The blue series-biased μLED array was fabricated by connecting 9 μLEDs in series and the device is in a flip-chip configuration. The diameter of a single μLED is 20 μm. The center-to-center pitch is 80 μm . Figure 4.2 presents the cross-sectional structure of the series-biased blue μLED array and its optical image. The fabrication process of the series-biased blue μLED array is given as follows. The disk shaped μLEDs are etched first down to n-type GaN layer by Cl_2 based ICP etching. Then, the square shape GaN mesas are further etched down from n-type GaN layer to the sapphire substrate by another ICP etch, in order to fully isolate each μLED. After that, a 100 nm thick Pd metal layer is deposited on the top of the p-type GaN. To form a quasi-ohmic contact on p-type GaN, a thermal annealing in a N_2 ambient at 300 °C is introduced. A bilayer of Ti/Au (50 nm/200 nm) is then deposited on GaN mesas as an n-type contact. After that, a 300 nm thick SiO_2 layer is deposited as an insulation layer and then the SiO_2 layer on the top of each μLED and the designed area of the GaN mesas is removed by using RIE as mentioned in section 2.1.2. Finally, another Ti/Au bilayer is deposited to connect each μLED

with a series connection configuration. For further characterizations and VLC measurements, the fabricated series-biased blue μLED array is wire-bonded to a printed circuit board. All the device characterizations and measurements are performed without any thermal management.

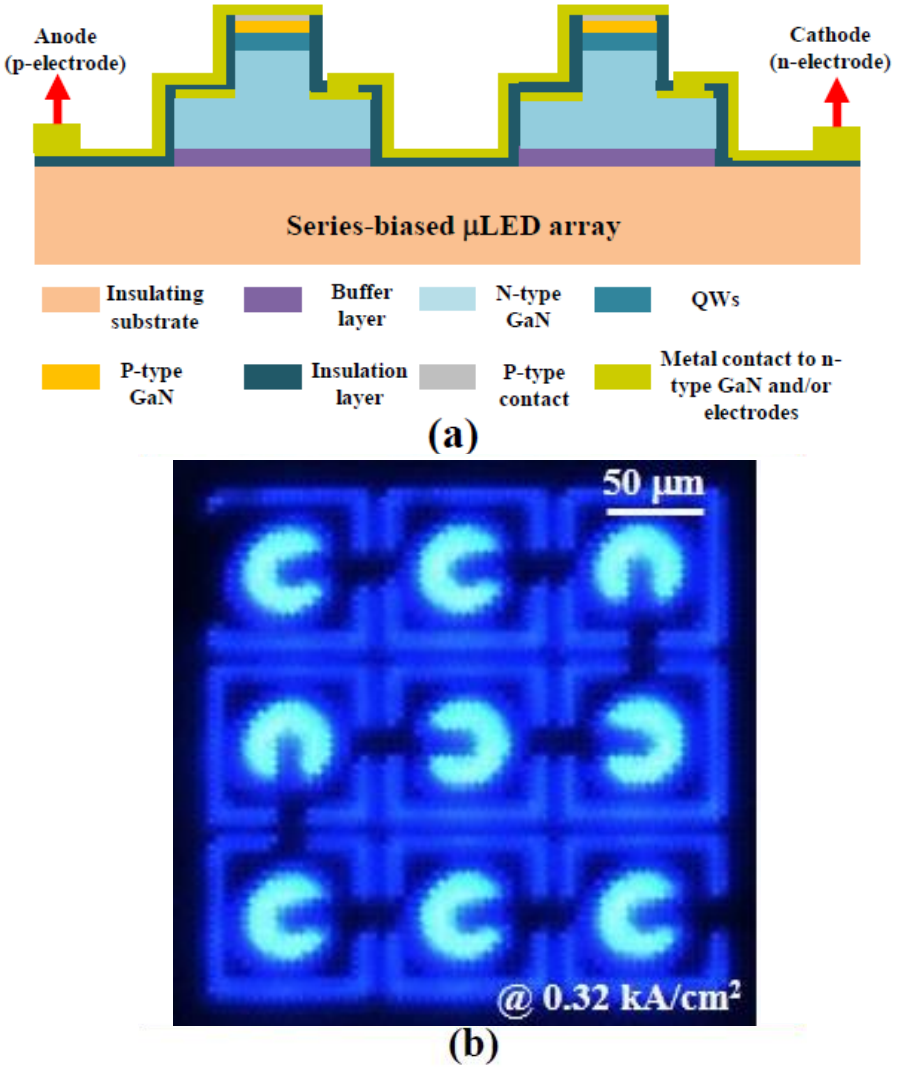

FIGURE 4.2: Cross-sectional structure and (b) optical image of the operating series-biased blue μLED array. After [5].

The current density versus voltage (J-V) and optical power versus current density (L-J) characteristics of the series-biased blue μLED array were measured following the method described in section 2.2.2. The 6-dB electrical modulation bandwidths were measured following the similar method described in section 2.2.3.

The *J-V* and *L-J* characteristics of the series-biased blue μLED array are presented in figure 4.3 (a). A turn-on voltage of 27.5 V at 0.32 kA/cm^2 (1 mA) is observed in figure 4.3 (a). The measured series resistance of the array is 165 Ω. Thus, the turn-on voltage and series resistance of each μLED are 3.1 V and 18 Ω, respectively. The maximum optical power produced by this array is over 10 mW at 11.15 kA/cm^2 current density. Since the array could be driven under such a high current density, it is expected that the modulation bandwidth of the array is also high. Figure 4.3 (b) shows the measured 6-dB electrical modulation bandwidth versus current density. It can be seen that the maximum 6-dB electrical modulation bandwidth of the array is in excess of 980 MHz at 11.15 kA/cm^2 current density. Compared with the performance of the single blue μLED mentioned in section 4.1.1, this series-biased blue μLED array provides not only higher optical power, but also higher modulation bandwidth under the same operating current density. As section 1.3 mentioned, the modulation bandwidth of μLEDs is limited by the differential carrier lifetime and the *RC* time constant [6]. Compared with the configuration of the single blue μLED, the series connection configuration reduces the total capacitance of the μLED array. However, it also increases the overall resistances of the μLED array. Therefore, in order to explain why the series-biased blue μLED array has higher modulation bandwidth under the same operating current density compared with the one of the single blue μLED, the *RC* time constants of both μLEDs may need to be further studied.

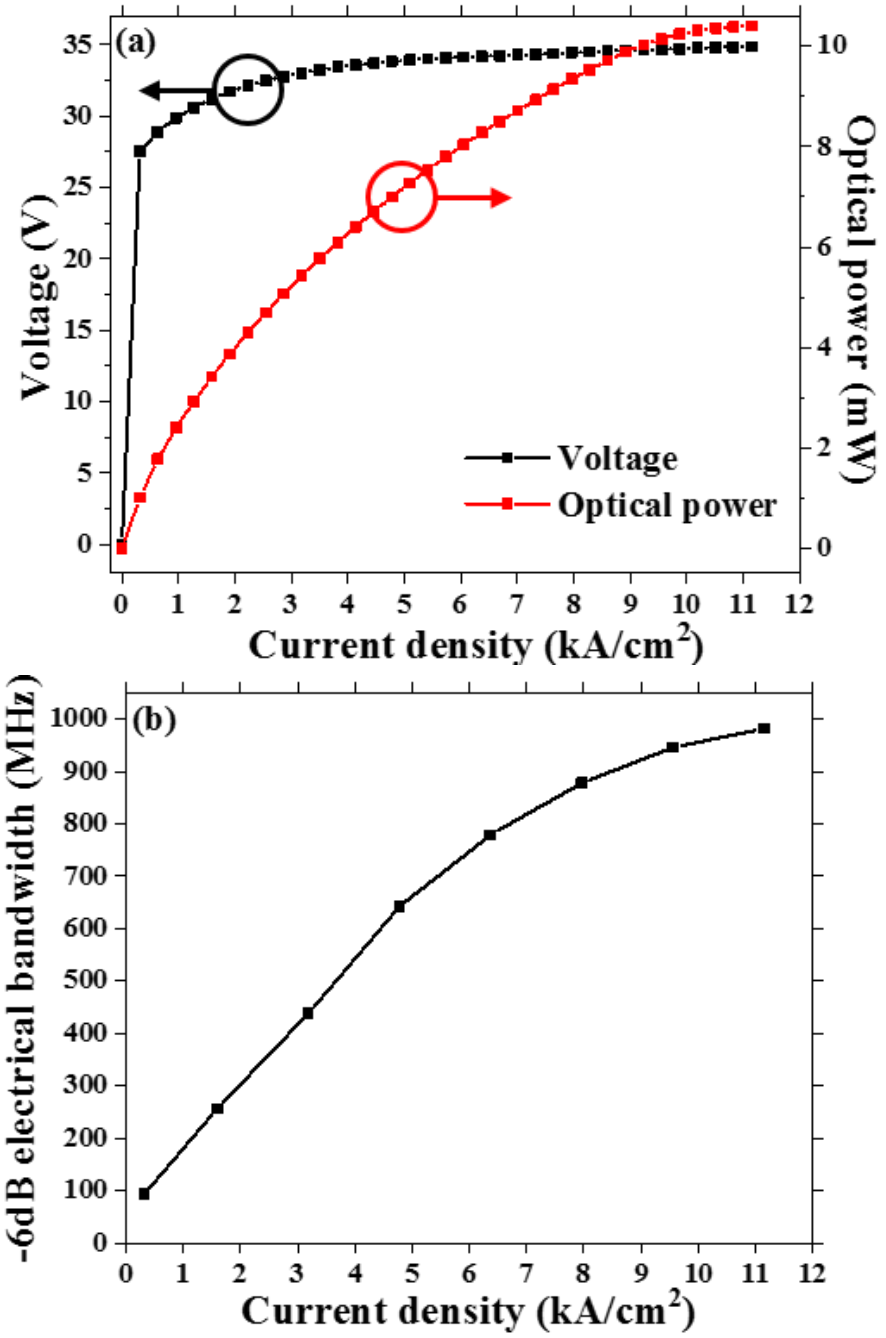

FIGURE 4.3: (a) *J*-*V* and *L*-*J*, and (b) 6-dB electrical modulation bandwidth versus current density of the series-biased blue μLED arrays. After [5].

With improved performances, the series-biased μLED array offers many benefits to the VLC data transmission rate and data transmission distance. Figure 4.4 shows a schematic diagram of the free-space VLC system used in this work. The data transmission distance of the VLC system can be varied and the system

assumes an OFDM modulation scheme. The inserts in the figure are the optical images of the transmitter and receiver modules. To characterize the distance dependent performance of the VLC system, the distance between the series-biased blue μLED array and photoreceiver was set as 0.3, 2, 5, and 10 m respectively. The VLC system performance was measured by the same method described in section 3.1. A high-power amplifier (AMP) SHF S126A is used in this system. The bias-T used is Tektronix PSPL5575A. An aspheric condenser lens (TX. Optics; Thorlabs ACL 4532A) was used to collimate the light emitted from the μLED array. We used another aspheric condenser lens (RX. Optics; Thorlabs ACL 4532A for 0.3 and 2 m distances, Thorlabs ACL 7560 for 5 and 10 m distances) to focus the light onto a fast-speed photoreceiver (Femto HSPR-X-I-1G4-SI). A digital oscilloscope (Kesysight DSA90804B) was employed to collect and display the output signals from the photoreceiver. To achieve optimized system performances, the modulation signal depth, V_{PP}, and the DC-bias current density, J_{DC}, are set as 8.17 V and 8.12 kA/cm^2, respectively.

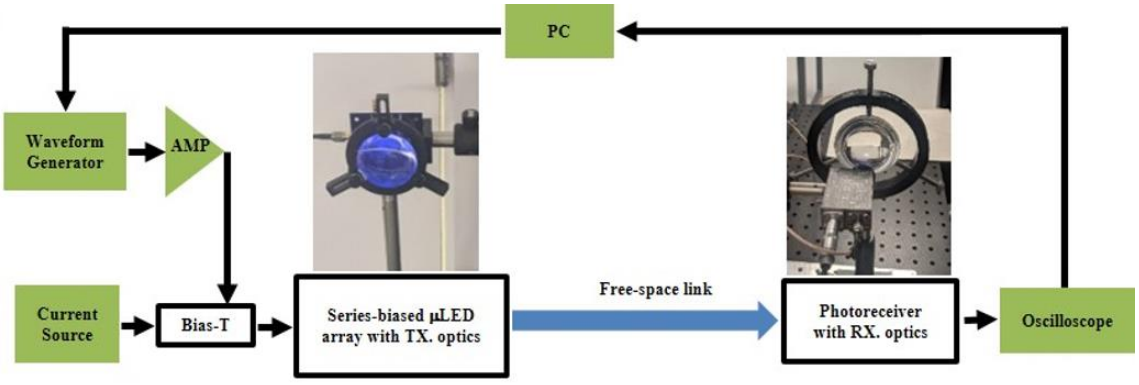

FIGURE 4.4: Schematic diagram of the setup used in this work for free-space VLC systems. After [5].

The first VLC measurement was performed at a 0.3 m free-space data transmission distance. Figure 4.5 (a) demonstrates the measured SNR versus the bandwidth of the system. A 2.3 GHz bandwidth is observed with the SNR higher than 5dB in the figure. With such a large bandwidth, substantial channels could be used for bit loadings in the OFDM modulation scheme to approach the limitation

of data capacity. In particular, OFDM subcarriers up to 2.2 GHz can be used to load a modulation order of 4 quadrature or higher amplitude modulation. Therefore, a highspeed VLC system is achieved. Figure 4.5 (b) presents the measured data transmission rates versus BER of the VLC system at a 0.3 m free space data transmission distance. As shown in the figure, a 11.74 Gbps data transmission rate is achieved at the FEC level of 3.8×10^{-3}, which is 50% higher than the one measured in section 5.1. There are two factors making such improvement. One is the impressive SNR performance of the system, contributed by the high optical power and high modulation bandwidth of the series-biased μLED array. Another factor is the VLC system has a much improved light collection efficiency due to the small pixel pitch of the μLED array and appropriate diameters of the employed aspheric condenser lenses in the setup. Moreover, it is considered that the performance of the VLC system is limited by the bandwidth (1.4 GHz) of the photoreceiver used. Therefore, an even higher data transmission rate can be expected by employing a high bandwidth photoreceiver.

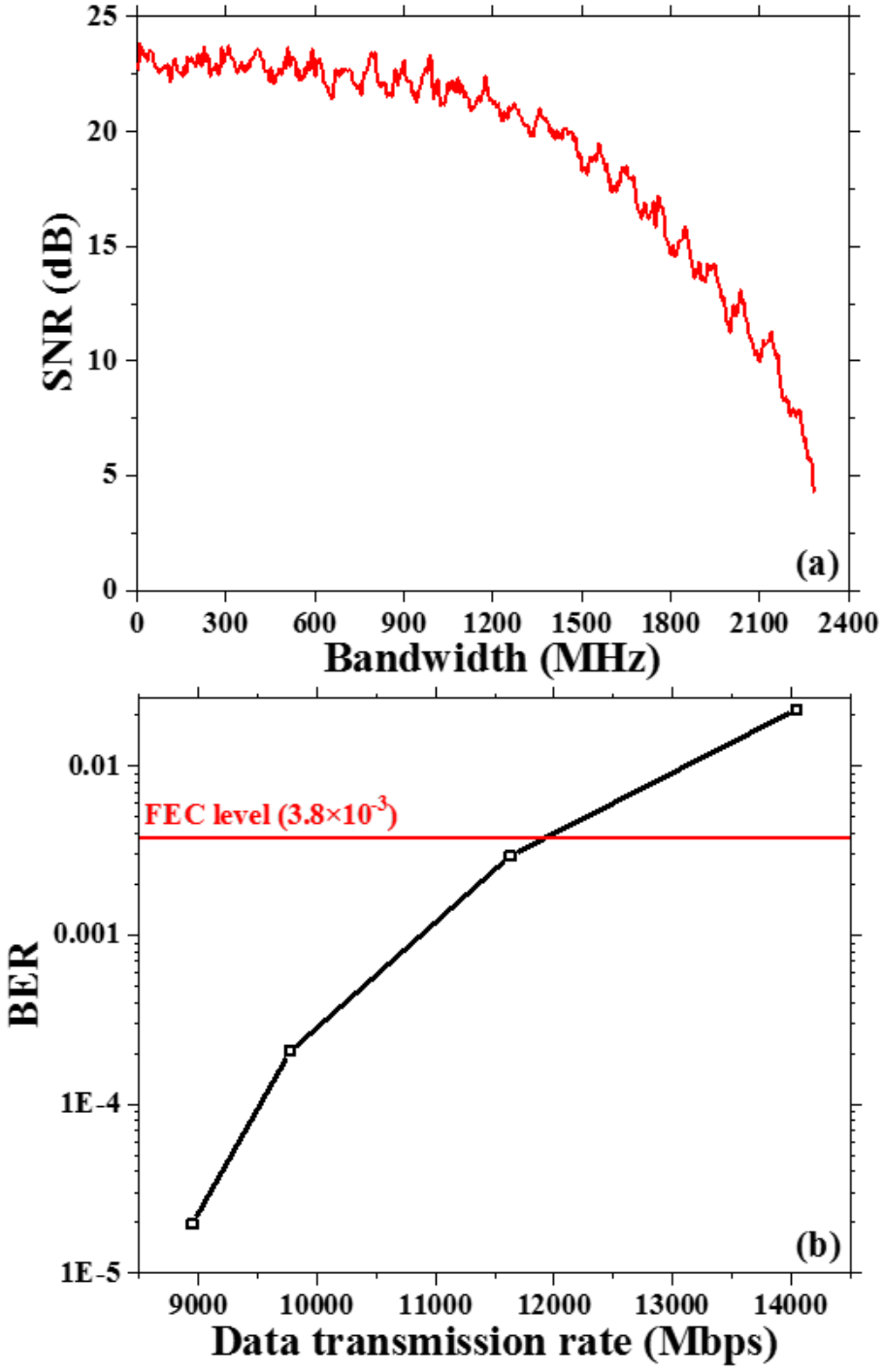

FIGURE 4.5: (a) SNR against bandwidth and (b) BER versus data transmission rate of the VLC system with a series-biased blue μLED array light source. After [5].

In order to study the distance dependent performance, the data transmission rate of the VLC system was further measured at 2, 5, and 10 m transmission

distances respectively. Figure 4.6 presents the achieved data transmission rates at the FEC level at different transmission distances. It can be seen that at 2, 5, and 10m, 11.72, 10.11, and 6.58 Gbps data transmission rates are achieved, respectively. To the best of our knowledge, these are the highest data transmission rates of a μLED based VLC system. Therefore, this work demonstrates that the series-biased μLED array is a suitable light source for the high speed and long distance VLC communications. The received optical powers at these distances are also measured and shown in figure 4.6. Clearly, the data transmission rate reduced as received optical power decreased. Thus, the one of main factors which determines the VLC performance is the received optical power. It could be expected that the SNR is dropped when the received optical power is decreased at long distances. This results in a limitation on the channel utilization in the OFDM scheme. Thus, the data transmission rate is decreased.

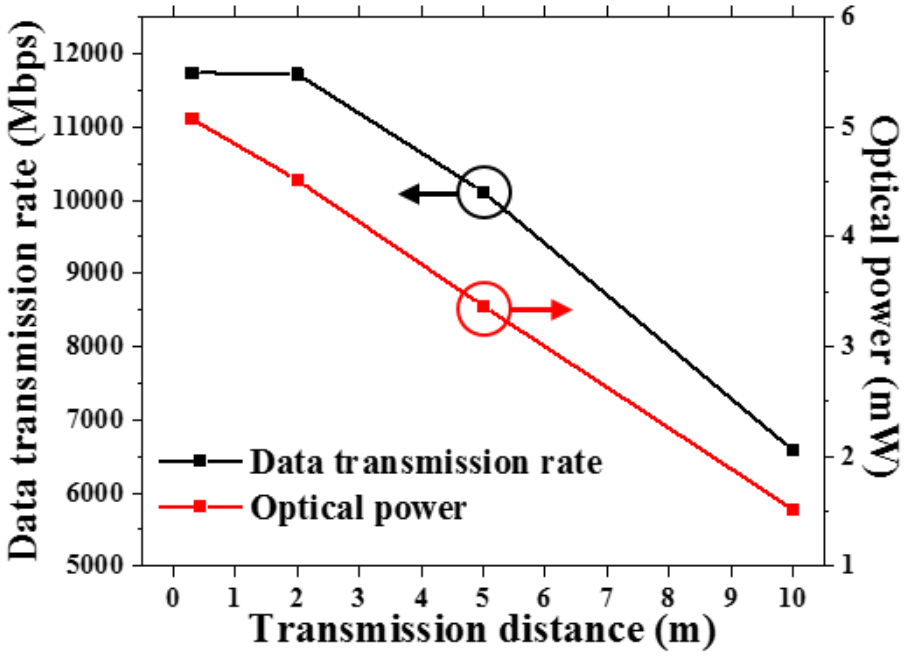

FIGURE 4.6: Data transmission rate at FEC level and received optical power against data transmission distance of the blue series-biased μLED array based VLC system. After [5].

4.2 Series-biased violet micro-structured light emitting diodes

4.2.1 Single violet μLED based VLC systems

VLC that utilizes white LEDs for both illumination and data transmission has gained great interest in recent years [7]. Besides huge energy saving on general lighting, VLC based on white LEDs also offers sufficient unlicensed bandwidth in visible light spectrum and, in turn, a solution to the wireless data traffic congestion caused by the limited availability of radio frequency spectrum [3]. The most common format of white LEDs involves the GaN-based blue LEDs and yellow-emitting phosphors. A data transmission rate up to 2.32 Gbps on VLC has been achieved using this phosphorescent white LED in the recent work [8]. However, there are several shortcomings to this implementation. It includes the poor colour rendering index (CRI) [9] and the disruption of the human circadian rhythm caused by the direct blue component [10].

An alternative method for white light generation is to combine GaN-based violet LEDs emitting at around 405 nm with multicolour colour-converters [7]. There are a number of works proposing the benefits from this implementation on the illumination aspect. For GaN-based violet LEDs themselves, their IQE and, in turn, optical power has been greatly improved in recent years [11], which is now comparable with the one of GaN-based blue LEDs. By using these violet LEDs to excite multicolour colour-converters, the generated white light also offers several advantages such as superior CRI, improved luminous efficacy, higher operating luminous flux, higher colour stability and absence of the direct blue component [12]. Nevertheless, only a few papers have investigated the VLC performance of GaN-based violet LEDs. My previous work demonstrated the first VLC application of the single violet μLEDs fabricated from commercial GaN-based LED wafers [13]. Figure 4.7 shows the structure of a violet (400nm) LED wafer used in the

work. Such III-nitride based LEDs wafers are commercially available. The LED epitaxial structure consists of a 4.5 μm thick undoped GaN buffer layer, a 1.8 μm thick n-typer GaN layer, 116 nm thick active layer, a 25 nm thick p-type AlGaN electron blocking layer, a 25 nm thick p-type GaN layer and a 2.5 nm thick n-type GaN layer.

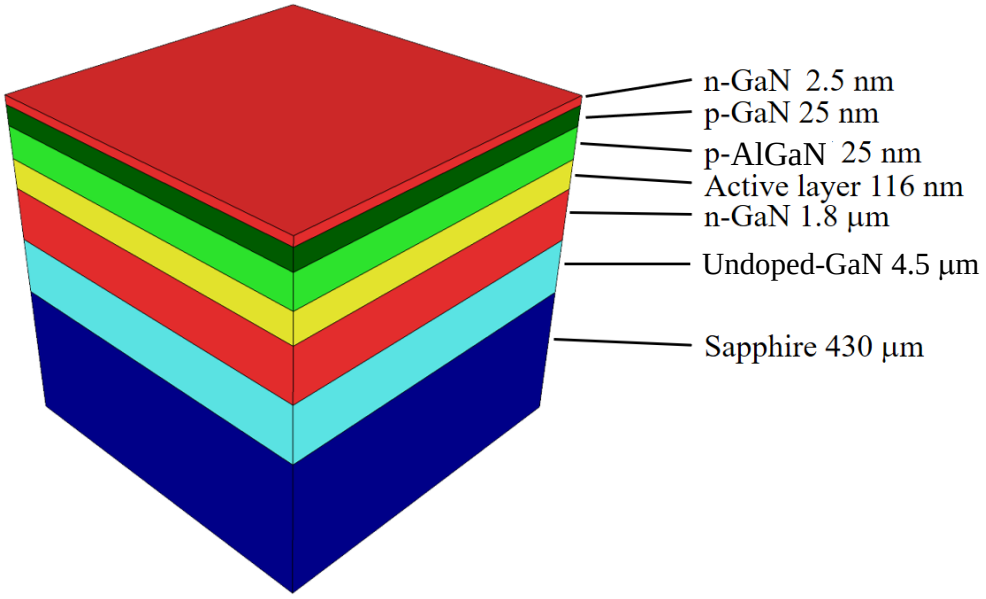

FIGURE 4.7: Schematic of a violet LED wafer structure.

Figure 4.8 illustrates the optical images of the fabricated violet μLEDs. The device structure is the same as the blue μLEDs mentioned above, which consists of two circular μLED arrays, an inner and outer. These 15 individual trapezoidal shape blue μLEDs contains 5 inner and 10 outer μLEDs with 435 μm^2 and 465 μm^2, respectively. The fabrication process for these violet μLEDs is similar with the blue μLEDs mentioned in section 4.1 as well. The wafer is firstly etched by ICP to expose n-type GaN. An annealed Pd layer is then deposited and patterned as metal contacts to p-type GaN. A 300 nm thick SiO_2 is used to isolate each μLED. A Ti/Au metal bilayer (50/300 nm) is deposited on the top of the n-type GaN to accomplish the metallization. The areas between each μLED are covered by the same metal bilayer in order to improve current spreading. Each μLED is also connected by the metal bilayer in order to individually address these μLEDs.

With this specific design, the mutual heating between μLEDs would be minimized, in turn, increasing the total output power. For inner μLEDs, the measured optical power of the single μLED is around 2.3 mW, and the measured 6-dB electrical modulation bandwidth is 655 MHz. These measurements are taken following the methods described in section 2.2.2 and 2.2.3.

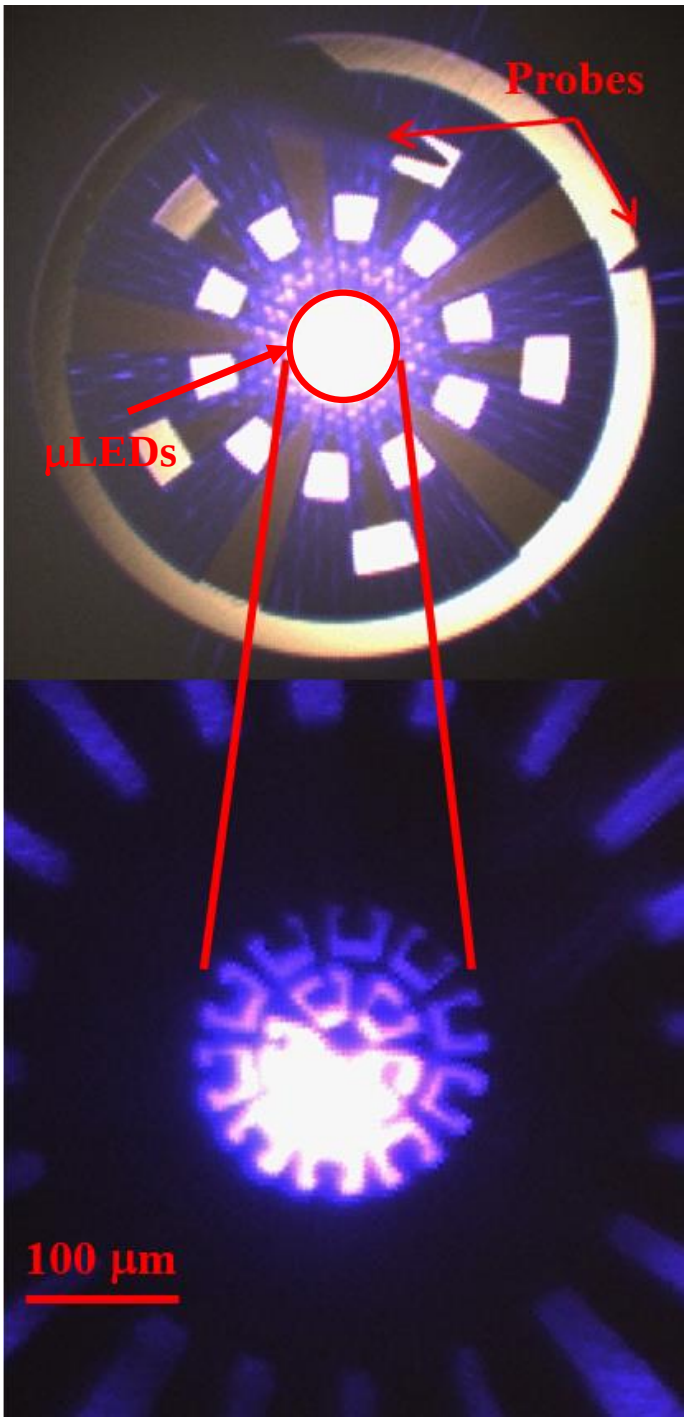

FIGURE 4.8: Top-view Optical images of violet μLEDs. After [5].

By using these single violet μLEDs, we have set up a VLC system with an OFDM modulation scheme. The VLC data transmission results of this system were measured by the following process. An OFDM signal was generated by an

arbitrary waveform generator (AWG, AWG70001A), and combined with a DC bias by using a bias-tee (Mini-Circuits ZFBT-4R2GW+). The maximum peak-to-peak voltage (V_{PP}) of the AWG is 0.5 V_{PP} . The output signal from a violet μLED was amplified by an amplifier (SHF 100AP). Three lenses were used to collect and focus the output signal from the violet μLED into a Si photoreceiver (Femto HSPR-X-I-1G4-SI). The Si photoreceiver has a 3 dB bandwidth of 1.4 GHz and a responsivity of 0.135 A/W around 400 nm wavelength. A digital oscilloscope (Keysight, MSO8104A) was used to capture the output signal. The captured signals were processed by a MATLAB program. The distance between the μLED and photoreceiver was approximately 30 cm. Figure 4.9 presents the experimental set up used in this work. For this system, with a 30 mA DC bias and 3.88 V peak to peak voltage setting, a 7.91 Gbps data transmission rate is achieved at a BER just below the FEC threshold of 3.8×10^{-3}. Although the data transmission performance of a single violet μLED based VLC system is promising, the high accurate alignment requirement between a transmitter and a receiver, short transmission distance, and low coverage area due to the low optical power provided by a single violet μLED present great challenges for achieving the system in the real world applications. In the real world VLC applications, such as indoor communication, it is difficult to apply bulky optics for both transmitter and receivers due to the size limitation of devices (for example: mobile phones). Thus, the requirements of the alignment between transmitters and receivers need to be dropped. In turn, the coverage and data transmission of this VLC system need to be improved. A straight forward solution is to apply a transmitter into the system, which needs to have higher optical power and similar modulation bandwidth compared with a single violet μLED. The details of this solution will be discussed in the following subsection.

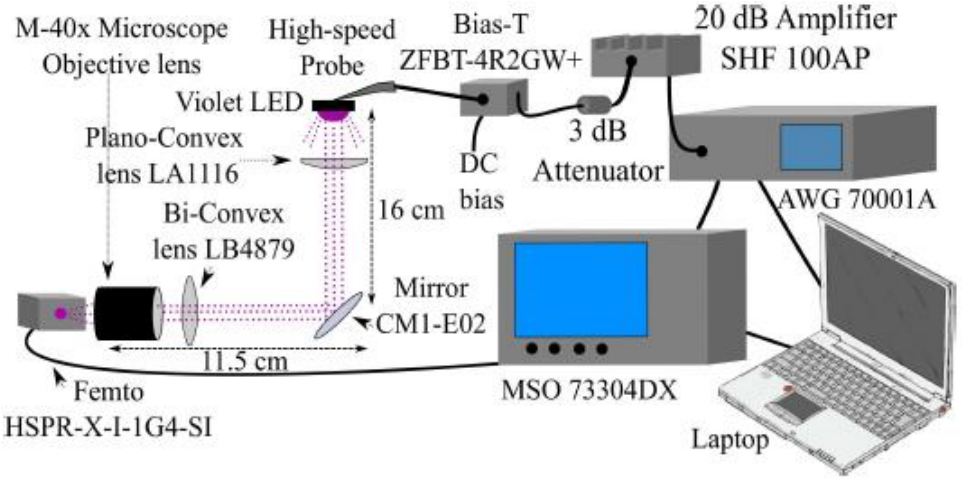

(a) Schematic

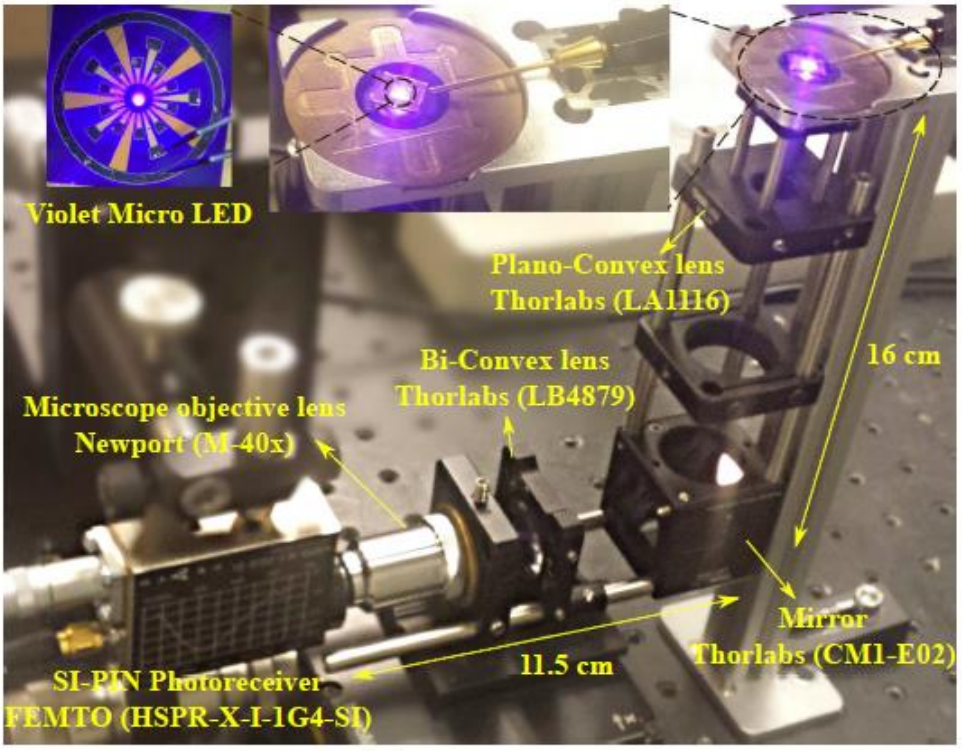

(b) Photograph

FIGURE 4.9: Experimental set up of a VLC system with a single violet μLED light source (a) Schematic of the set up, (b) image of the VLC system. After [5].

4.2.2 Development of series-biased violet micro-structured light emitting diodes for VLC applications

As mentioned above, a single violet μLED can be operated at higher current densities, enabling significantly higher modulation bandwidth. This makes violet μLEDs promising candidates for VLC. However, low optical power produced from a single violet μLED limits the data transmission distance and signal-to-noise ratio. Although a violetμLED array operating in a ganged fashion could be used to increase the optical power produced, each violet μLED element in the array needs to be individually addressed to retain fast modulation speed [14]. This leads to the complex design, fabrication and integration processes for both μLED array and driver circuit. Therefore, it is important to develop violet μLED arrays with high optical power, high modulation bandwidth and simple addressing scheme as the transmitter for VLC systems. Series-biased violet LED arrays, which are referred as high-voltage LED arrays in the references, will meet these requirements. For example, due to the series-connection configuration, series-biased LED arrays have a high optical output power and their capacitances are smaller than the one of each individual LED element in the array, which enables a large increase in modulation bandwidth. Thus, series-biased violet μLED arrays are considered to be suitable, compact and inexpensive light sources for VLC applications [15].

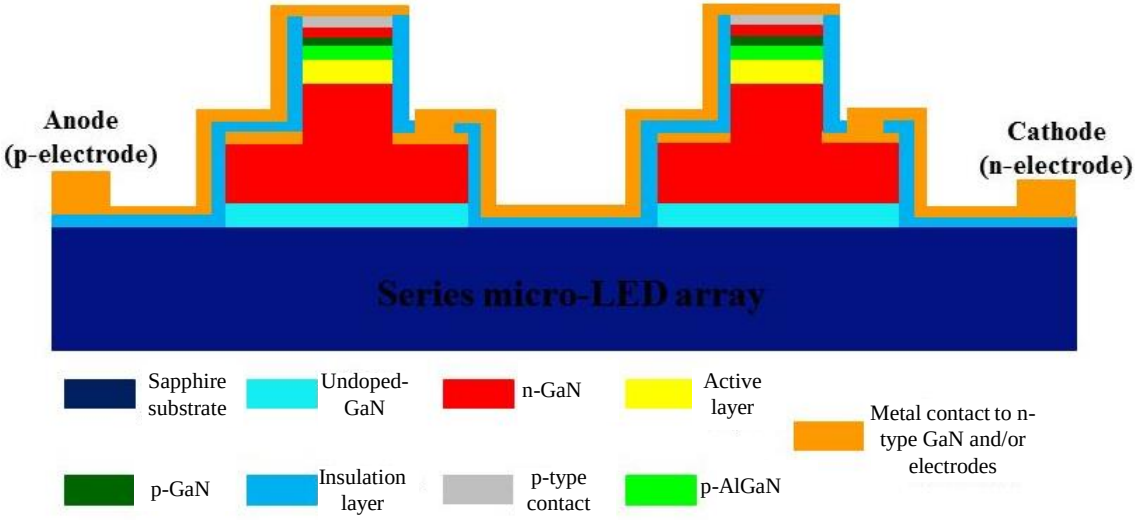

FIGURE 4.10: Schematic of the series-biased violet μLED arrays.

The series-biased violet μLED array is fabricated on a commercial III-nitride based violet LED wafer. The detailed wafer structure is given in Figure 4.7. The fabricated series-biased violet μLED array consists of 3 by 3 μLEDs in a flip-chip configuration. The diameter of a single μLED is 40 μm. The center-to-center pitch of these μLEDs is 160 μm. The area of n-GaN mesa for n-type metal contacts is 90×90 μm^2. There are 3 bonding pads with 150 μm side length, which enable us to operate 3, 6 and 9 in series violet μLEDs, respectively. Figure 4.10 presents the schematic structure of the series-biased violet μLED array . The fabrication process of the series-biased violet μLED array is the same with the series-biased blue μLED array, which is given in section 4.1. Figure 4.11 shows the fabrication process of the series-biased violet μLED array along with an image showing the array on operating status. In order to further characterize and understand the performance of the violet μLEDs, 40 μm and 120 μm single violet circle shape μLEDs, and 9×40 μm violet μLEDs connected in parallel are fabricated. The fabrication process of these μLEDs is similar to the one described in section 4.1. These fabricated μLED devices were wire-bonded to a printed circuit board for the performance characterizations and the devices were measured without any thermal management.

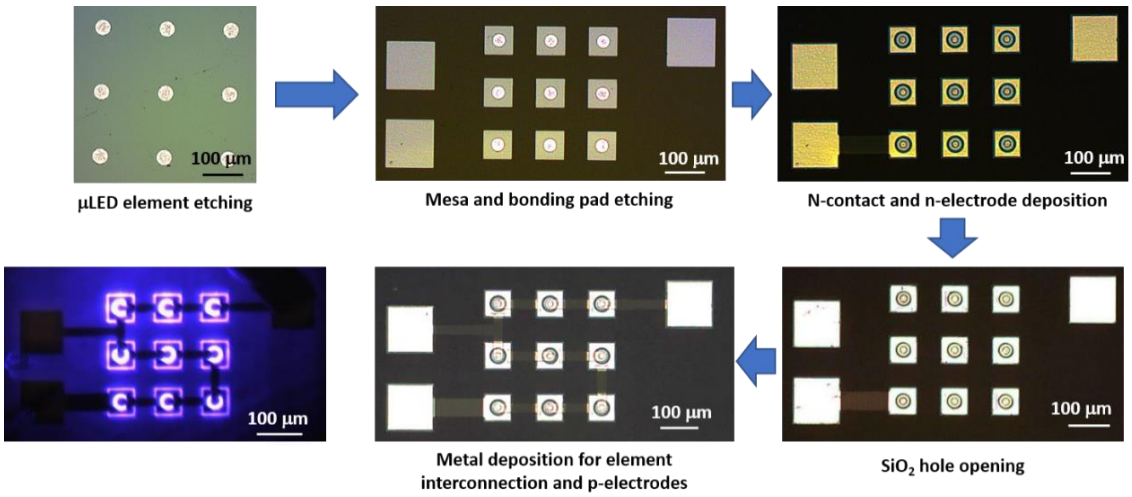

FIGURE 4.11: Optical images of the fabrication process of the series-biased violet μLED array along with an image of the array on operating status.

Figure 4.12 (a) presents the *L-J* curves of all the fabricated violet μLEDs. As the figure shows, the devices with 9, 6, 3 violet μLEDs connected in series and a single 40 μm μLED could be driven up to a higher current density (2000 A/cm^2) compared with the 9- violet μLEDs connected in parallel and 120 μm single μLED. At 2000 A/cm^2, the series-biased 9- violet μLEDs provides roughly 9 times higher optical power (about 18.06 mW) comparing with a 40 μm single μLED. Namely, the optical power of the series-biased μLED array is proportional to the total emission area of the array. To compare these μLEDs, wall plug efficiency (WPE), which is energy conversion efficiency with that the system converts electrical power into optical power, is applied. Figure 4.12 (b) presents the WPE versus J of all the μLEDs. It can be seen that, WPEs of the 40 μm single violet μLED and all the series-biased violet μLEDs show similar trend when the current density is increased. Moreover, at the same emission area, the array with 9- series-biased violet μLEDs shows much higher WPE in comparison to the array with 9- violet μLEDs connected in parallel and the 120 μm single μLED. Therefore, the array with 9- series-biased violet μLEDs has better thermal management, and in turn, provides a higher emission optical power.

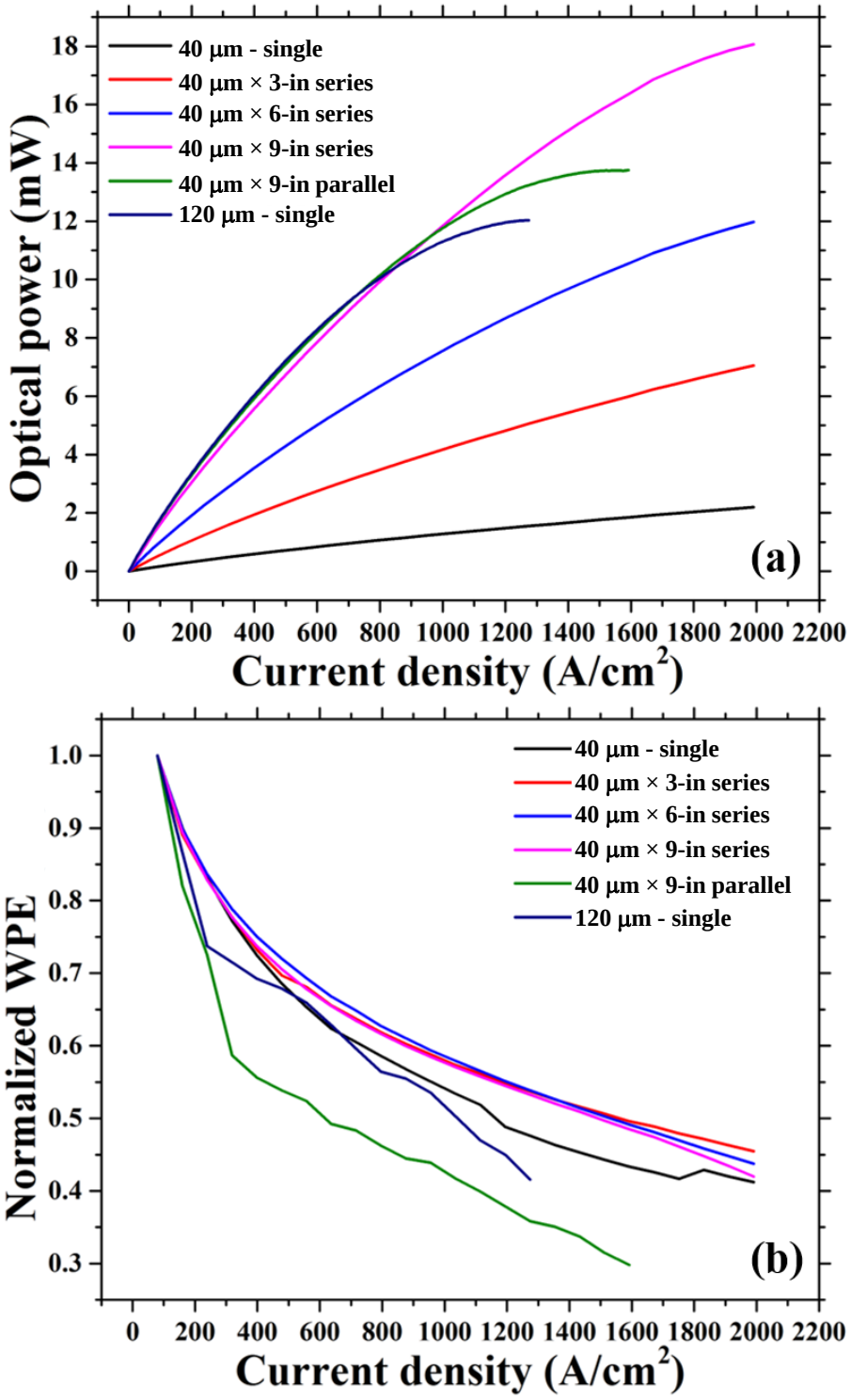

FIGURE 4.12: *L-J* and WPE of all measured μLEDs.

Figure 4.13 (a) shows the measured 6-dB electrical modulation bandwidth curves of all the violet μLED devices. It can be seen in figure 4.13 (a) that

all the series-biased μLEDs show the similar and high E-O bandwidth as a 40 μm single μLED before the current density reaches 1200 A/cm^2. The series-biased violet μLED arrays show significantly higher 6-dB electrical modulation bandwidths compared with the parallel–biased 9- μLED array and the single 120 μm LED which have the same emission area. These results can be seen clearly in figure 4.13 (a). Figure 4.13 (a) also shows that by further increasing the current density from 1200 A/cm^2, the 6-dB electrical modulation bandwidth of a 40 μm single violet μLED becomes higher than those of all the series-biased violet μLEDs. This may be due to the superior thermal management property of the single 40 μm violet μLED at high current densities. As a demonstration, the data transmission with OFDM modulation scheme was only measured with a series-biased 6-violet μLED array. The measurement was performed in the same way as the one described in section 4.1. Figure 4.13 (b) presents the measured data transmission result. As shown, the maximum data rate of 3.37 Gbps is achieved with BER under the FEC level at 3.8×10^{-3}.

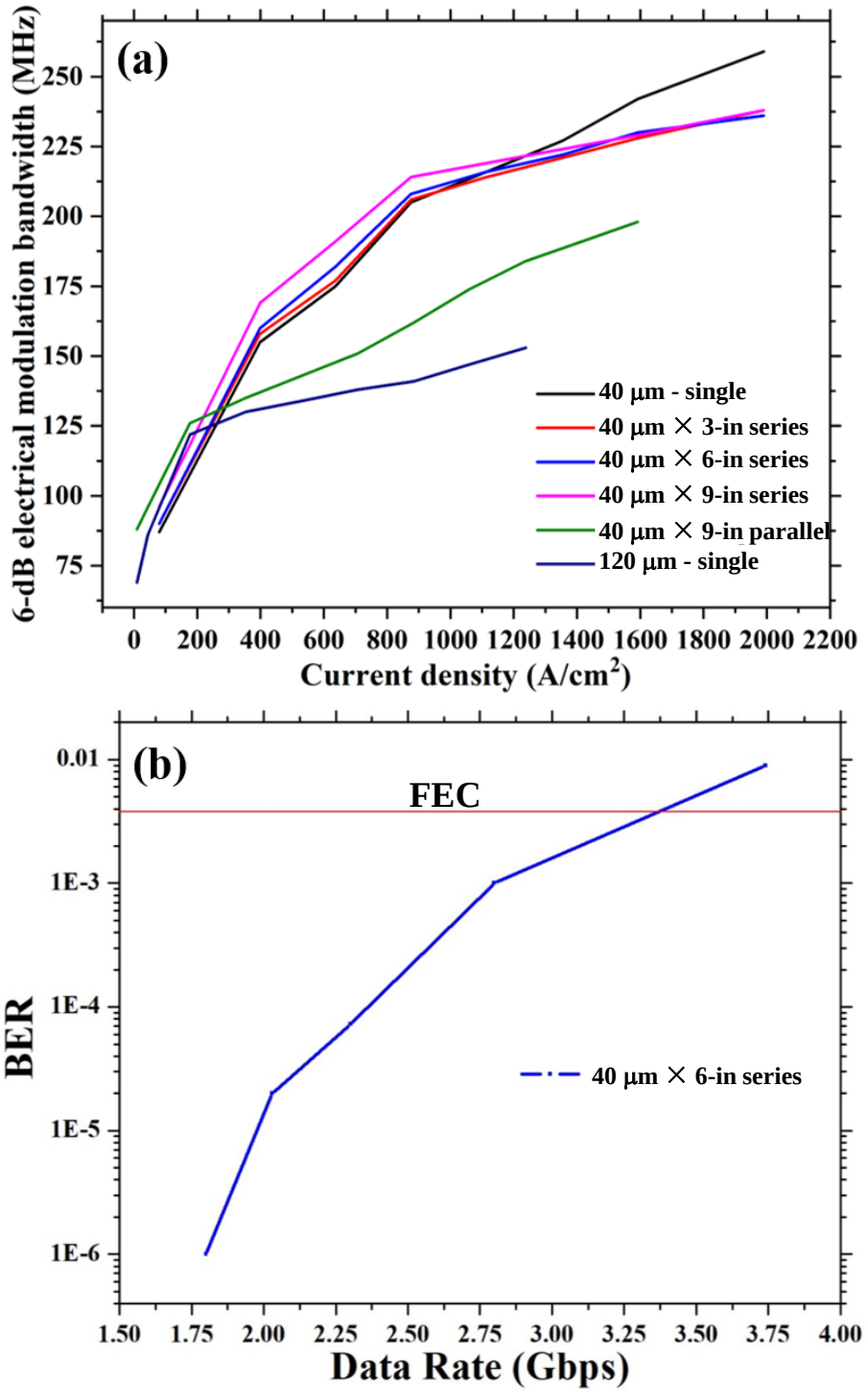

FIGURE 4.13: (a) 6-dB electrical modulation bandwidth of all measured μLEDs, and (b) measured data transmission rate of the VLC system with a series-biased 6- violet μLED array.

This measured data transmission rate is much lower than expected. The reason

for this unexpected result is that the center-to-center pitch of this violet series-biased μLEDs is too wider (160 μm). Therefore, only part of light emitted by the μLEDs can be collected and focused into the photoreceiver. This caused a significantly low BER in the VLC system, thus a low data transmission rate. To overcome this issue, I reduced the center-to-center pitch (80μm) of the series-biased violet μLED array to make sure all the emitted light can be collected. Furthermore, in order to maximize the performance of the series-biased violet μLEDs, I also reduced the diameter of the μLEDs to 20 μm. After these optimizations, new series-biased 9- violet μLED arrays were fabricated. For comparison, a series-biased 6- violet μLED array is applied in the measurement. These array devices were used as the light source for the same VLC system. The data transmission rates at different transmission distances of this VLC system under OFDM modulation scheme were measured. Figure 4.14 shows the data transmission rates versus BER of this VLC system at 0.3, 2, 5, and 10 m free space data transmission distances. As figure shows, an over 12 Gbps data transmission rate is achieved at the FEC level of 3.8×10^{-3} at 0.3 m data transmission distance. At data transmission distances of 2, 5, and 10 m, 11.8, 9.9, and 6 Gbps data transmission rates are achieved, respectively. To the best of my knowledge, these are highest data transmission rates for violet μLED based VLC systems. Therefore, there series-biased violet μLED arrays are a suitable light source for high speed and long distance visible light communications.

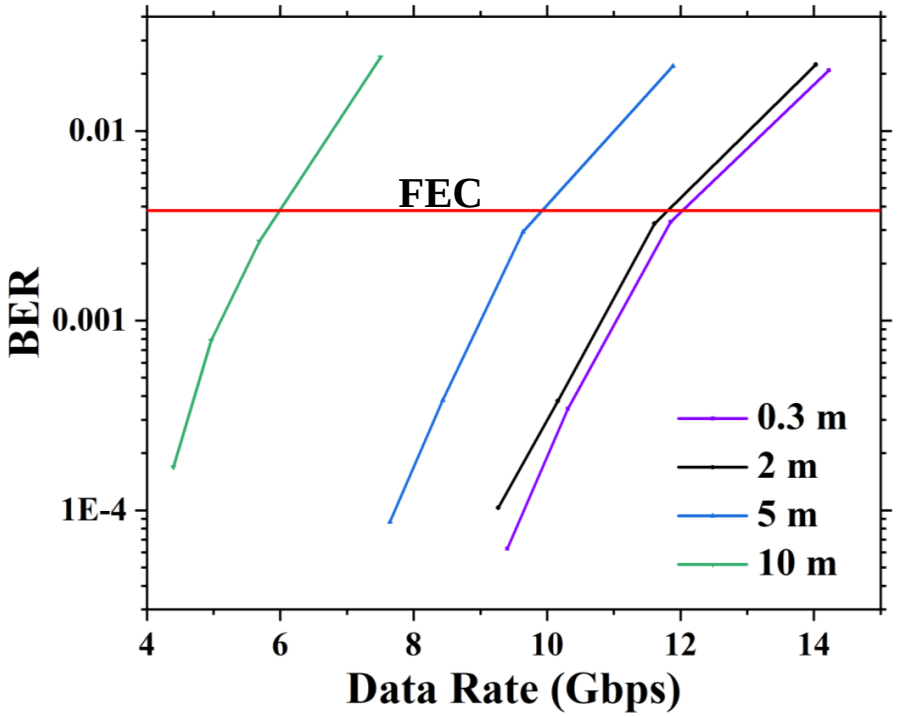

FIGURE 4.14: Data transmission rate versus BER of the VLC system with series-biased violet μLED array at 0.3, 2, 5, and 10 m data transmission distances.

4.3 Summary

In summary, this chapter presents the developments and VLC applications of blue and violet μLED devices. For each colour, single μLED fabrication and its VLC applications are given first. Then, new series-biased μLED arrays were developed. The design and fabrication process of these series-biased μLED arrays are given in detail. These series-biased μLED showed higher optical power and 6-dB electrical modulation bandwidth compared with the parallel–biased μLED array and the single LED which have the same emission area. The WPEs of the violet μLEDs have been measured and the enhanced performances of series-biased μLEDs were demonstrated. By using these series-biased μLED arrays, high VLC data transmission rates at long transmission distances (10 m) have been achieved.

References

[1] H. Burchardt, N. Serafimovski, D. Tsonev, S. Videv, and H. Haas. VLC: Beyond point-to-point communication. *IEEE Communications Magazine*, 52(7):98–105, 2014.

[2] S. Rajbhandari, J. J. D. McKendry, J. Herrnsdorf, H. Chun, G. Faulkner, H. Haas, I. M. Watson, D. O'Brien, and M. D. Dawson. A review of gallium nitride LEDs for multi-gigabit-per-second visible light data communications. *Semiconductor Science and Technology*, 32(2):023001, jan 2017.

[3] R. X. G. Ferreira, E. Xie, J. J. D. McKendry, S. Rajbhandari, H. Chun, G. Faulkner, S. Watson, A. E. Kelly, E. Gu, R. V. Penty, I. H. White, D. C. O'Brien, and Dawson. M. D. High bandwidth GaN-based micro-LEDs for multi-Gb/s visible light communications. *IEEE Photonics Technology Letters*, 28(19):2023–2026, 2016.

[4] D. Tsonev, H. Chun, S. Rajbhandari, J. J. D. McKendry, S. Videv, E. Gu, M. Haji, S. Watson, A. E. Kelly, G. Faulkner, M. D. Dawson, H. Haas, and D. O'Brien. A 3-Gb/s Single-LED OFDM-Based Wireless VLC Link Using a Gallium Nitride μLED. *IEEE Photonics Technology Letters*, 26(7):637–640, 2014.

[5] E. Xie, R. Bian, X. He, M. S. Islim, C. Chen, J. J. D. McKendry, E. Gu, H. Haas, and M. D. Dawson. Over 10 Gbps VLC for Long-Distance Applications Using a GaN-Based Series-Biased Micro-LED Array. *IEEE Photonics Technology Letters*, 32(9):499–502, 2020.

[6] E. F. Schubert. *Light-Emitting Diodes*. Cambridge University Press, 2006.

[7] J. J. D. McKendry, D. Tsonev, R. Ferreira, S. Videv, A. D. Griffiths, S. Watson, E. Gu, A. E. Kelly, H. Haas, and M. D. Dawson. Gb/s single-LED OFDM-based VLC using violet and UV gallium nitride μLEDs. In *Summer Topicals Meeting Series (SUM), 2015*, pages 175–176. IEEE, 2015.

[8] Y. Zhou, J. Zhao, M. Zhang, J. Shi, and N. Chi. 2.32 Gbit/s phosphorescent white LED visible light communication aided by two-staged linear software equalizer. In *2016 10th International Symposium on Communication Systems, Networks and Digital Signal Processing (CSNDSP)*, pages 1–4, 2016.

[9] P. J. Yadav, C. P. Joshi, and S. V. Moharil. Two phosphor converted white LED with improved CRI. *Journal of Luminescence*, 136:1–4, 2013.

[10] Q. Dai, Q. Shan, H. Lam, L. Hao, Y. Lin, and Z. Cui. Circadian-effect engineering of solid-state lighting spectra for beneficial and tunable lighting. *Opt. Express*, 24(18):20049–20059, Sep 2016.

[11] M. J. Cich, R. I. Aldaz, A. Chakraborty, A. David, M. J. Grundmann, A. Tyagi, M. Zhang, F. M. Steranka, and M. R. Krames. Bulk GaN based violet light-emitting diodes with high efficiency at very high current density. *Applied Physics Letters*, 101(22):223509, 2012.

[12] Y. Narukawa, I. Niki, K. Izuno, M. Yamada, Y. Murazaki, and T. Mukai. Phosphor-Conversion White Light Emitting Diode Using InGaN Near-Ultraviolet Chip. *Japanese Journal of Applied Physics*, 41(Part 2, No. 4A):L371–L373, Apr 2002.

[13] M. S. Islim, R. X. Ferreira, X. He, E. Xie, S. Videv, S. Viola, S. Watson, N. Bamiedakis, R. V. Penty, I. H. White, A. E. Kelly, E. Gu, H. Hass, and M. D. Dawson. Towards 10 Gb/s orthogonal frequency division multiplexing-based visible light communication using a GaN violet micro-LED. *Photonics Research*, 5(2):A35–A43, 2017.

[14] E. Xie, M. Stonehouse, R. Ferreira, J. J. D. McKendry, J. Herrnsdorf, X. He, S. Rajbhandari, H. Chun, A. V. N. Jalajakumari, O. Almer, G. Faulkner, I. M. Watson, E. Gu, R. Henderson, D. C. O'Brien, and Dawson. M. D. Design, fabrication, and application of GaN-based micro-LED arrays with individual addressing by N-electrodes. *IEEE Photonics Journal*, 9(6):1–11, 2017.

[15] C. Tien, K.Chen, C. Hsu, and R. Horng. Enhanced light output power of thin film GaN-based high voltage light-emitting diodes. *Opt. Express*, 22(S6):A1462–A1468, Oct 2014.

Chapter 5

III-nitride based micro-structured light emitting diode arrays with individual addressable n-electrodes

The work presented in this chapter focuses on the development, performance and application of the III-nitride μLEDs with individual addressable n-electrodes. Previous research has demonstrated a p-type metal-oxide-semiconductor (PMOS) driver controlled μLED array, and its application on VLC. Although such device has shown a high capability to VLC systems, its drawbacks are also considerable. For the VLC system based on a PMOS driver controlled μLED array, the poor μLED element-to-element uniformity, high element crosstalk, and low operating speed of PMOS transistors limit the performance of the entire VLC system. To overcome these issues, a new n-type MOS(NMOS) driver controlled μLED array is developed. The structure and performance of such a μLED array and its application to VLC systems are presented in this chapter.

5.1 Micro-structured light emitting diode arrays with individually addressable p-electrodes

With the development of the μLED fabrication techniques, different addressing schemes for μLED arrays have been reported in recent years [1–3]. In order to accomplish an active driving scheme, μLED arrays integrated with complementary MOS (CMOS) electronics by flip-chip bonding have been developed and reported [4]. These integrated μLED arrays are of great benefit to displays and VLC systems. Due to the standard III-nitride LED epitaxial structures, the μLED arrays normally share a common n-electrode (cathode) with individually addressable p-electrodes (anodes). This device configuration requires a PMOS driver. In 2012, our group reported a PMOS driver controlled blue μLED arrays [5]. Under PMOS driver control, the μLED showed a 185 MHz 3-dB modulation bandwidth and by using this integrated device, a data transmission rate of 512 Mbps was achieved under OOK modulation scheme. Figure 5.1 presents (a) an optical image of a portion of the μLED array and (b) a schematic of a μLED array with a common n-electrode and individually addressable p-electrodes.

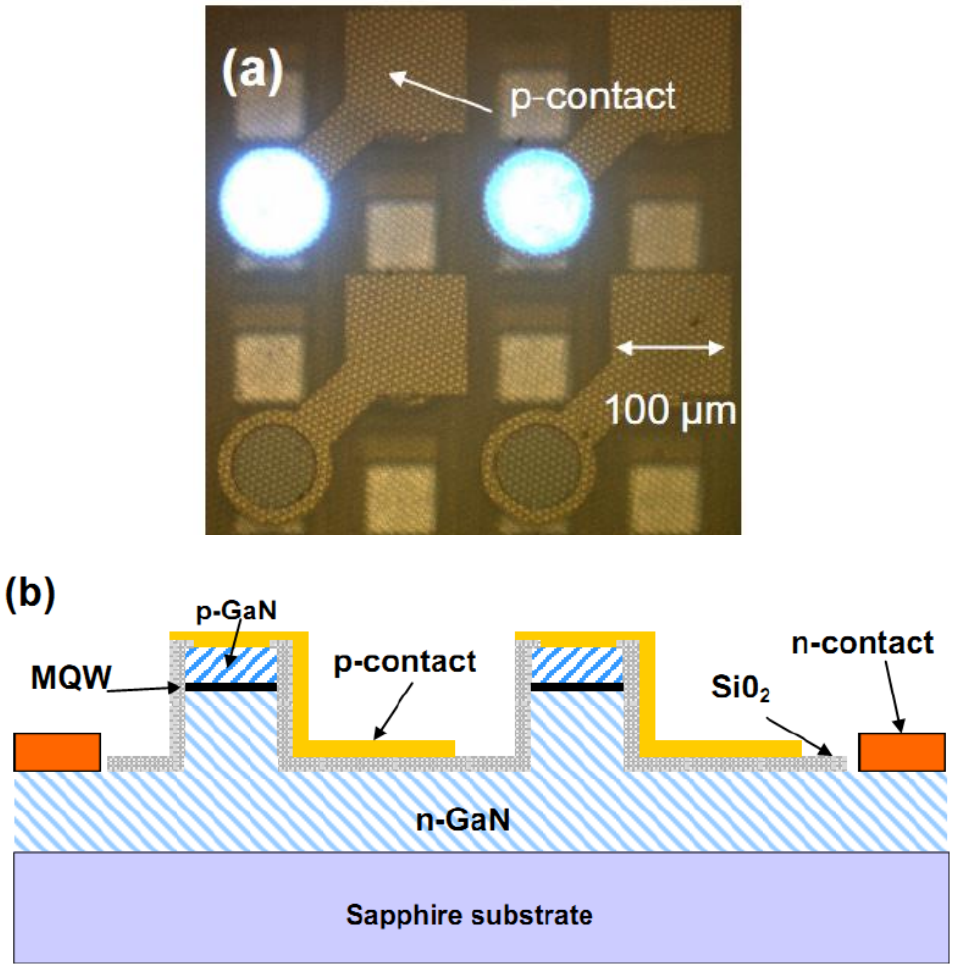

FIGURE 5.1: (a) Optical image and (b) schematic of a μLED array with a common n-electrode and individually addressable p-electrodes. After [5].

As shown in Figure 5.1 (b) in a standard III-nitride LED structure, the p-GaN layer is on the top [6] and n-GaN layer is at the bottom of the LED structure. For the μLED configuration as shown in Figure 5.1(b), the bottom n-GaN layer serves as a conductive path i.e. a common n-electrode to connect each μLED, As the n-GaN layer has a certain resistance and the distances between each μLED and n-contact are different, the series resistances of μLEDs in the array are different. This leads to non-uniform operating currents at the same applied voltage for each μLED, in turn, poor optical uniformity and high cross talk [2, 7]. These drawbacks are undesirable in practical applications. Moreover, this conventional μLED array can only be integrated with PMOS driver. Since the mobility of majority carriers

(holes) in PMOS transistors (about 450 $cm^2/(V{\cdot}s)$ in Si doped at 10^{15} cm^{-3}) is much lower than that of majority carriers (electrons) in NMOS transistors (1500 $cm^2/(V{\cdot}s)$ in Si doped at 10^{15} cm^{-3}) [6], the operating speed of PMOS transistors is slower than the one of NMOS transistors. Furthermore, the size of PMOS transistors is larger than the one of NMOS transistors at the same impedance. As a result, the capacitance of PMOS transistors is larger than the one of NMOS transistors. This will further reduce the operating speed of PMOS transistors [8]. As a result, the density of driver cells on a chip and the modulation speed of the PMOS are limited.

5.2 Micro-structured light emitting diode arrays with individually addressable n-electrodes

In order to overcome the issues caused by PMOS drivers, a new design of μLED arrays, which could be integrated with NMOS drivers, is necessarily needed. In this section, an innovative III-nitride based μLED array with a common p-electrode and individually addressable n-electrodes is presented. The various fabrication challenges to achieve this μLED array are addressed. This μLED array consists of 6×6 μLEDs. The μLED pitch is 300 μm. The diameter of a μLED is 24 μm.

5.2.1 μLED array fabrication

The μLED array is fabricated from the similar blue LED wafer which is introduced in section 4.1. As shown in figure 5.2, each μLED needs to be fully isolated from both p- and n-type GaN layers to achieve a μLED array with individually addressed n-electrodes. Therefore, two ICP etchings are required in the fabrication process.

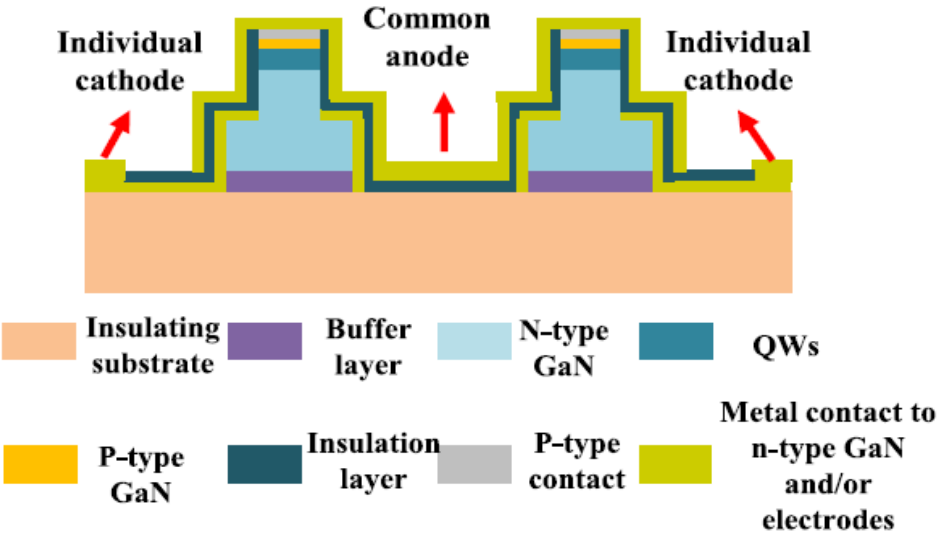

FIGURE 5.2: Cross-sectional structure of the μLED array developed in this work. After [9].

Figure 5.3 shows the main fabrication steps of this μLED array. As figure 5.3 (a) and (b) shown, a 6 $\times$ 6 array of square GaN mesas is firstly defined by the first ICP etching. Then, each μLED is defined by the second ICP etching. The GaN mesas have a square shape with sides of 130 μm. As these GaN mesas are etched down to the sapphire substrate, the μLEDs formed on the top of the mesa are isolated from each other. Meanwhile, each μLED has the same contact area of metal contacts to n-type GaN. The gap between GaN mesas is 170 μm. We have also fabricated another similar μLED array but the gap between GaN mesas in that array is reduced to 6 μm. In order to form a quasi-ohmic contact on the p-type GaN of each μLED, a 100 nm thick Pd metal layer is deposited on the top of the p-type GaN followed by 300 °C thermal annealing in a N_2 ambient. A Ti/Au (50 nm/ 300 nm) metal bilayer is then deposited and lifted off to form n-type contacts on the top of each GaN mesa and metal tracks which connect n-type contacts individually as shown in figure 5.3 (c). There are two specific lift-off photoresists used in this work, which are Dow Megaposit SPR220 4.5 (positive-resist) and Micro Resist Technology ma-N 1420 (negative-resist). Following the lift off process, the photoresist residues are removed by traditional solvent based

treatments in a non-optimized process. In the optimized process, these photoresist residues are removed by an O_2-based plasma at 200 ° C in a plasma asher (Matrix 105 system). Comparing the results on photoresist residue removing, it is found that the plasma ashing is a critical step to fabricate high quality μLED arrays, especially when the gap between the GaN mesas is small. The details of this process development and optimization will be discussed in the later part of this chapter. After the photoresist residue removing, a 300 nm-thick SiO_2 layer is deposited as an isolation layer. Then, the SiO_2 on the top of each μLED is removed by RIE as mentioned in subsection 2.1.2. and another Ti/Au (50/300 nm) metal bilayer is deposited to connect the p-type contacts of all the μLEDs to form a shared p-electrode as shown in figure 5.3 (d). Figure 5.3 (e) shows the whole layout of this μLED array.

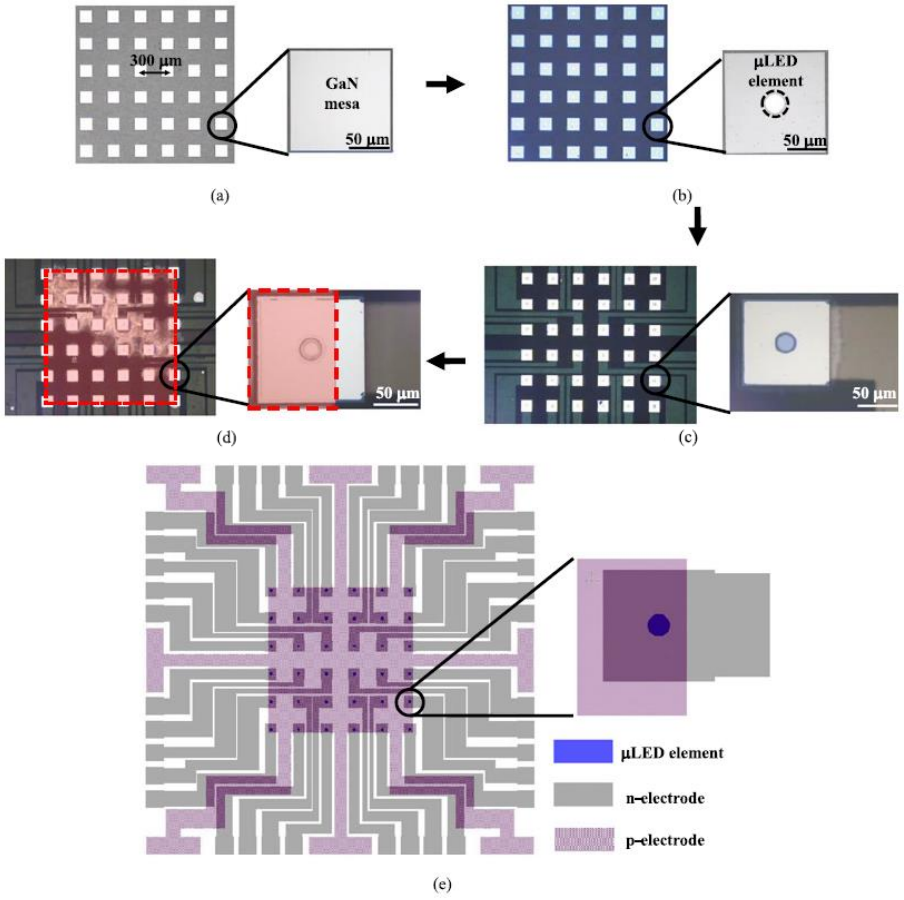

FIGURE 5.3: Optical Images of (a) GaN mesa define, (b) μLED define, (c) n-electrodes deposition, (d)p-electrode deposition, and (e) a whole layout of the μLED array. After [9].

5.2.2 μLED array characterization

The performance of μLED array is initially characterized before integrated it with a NMOS driver. The electrical, optical and modulation bandwidth properties of μLED array are measured using the same methods described in sections 2.2.2 and 2.2.3. Figure 5.4 shows the electrical, optical, and 6-dB electrical bandwidth performances of a single μLED in this μLED array. As shown in figure 5.4 (a), the operating current of the single μLED can be over 80 mA, which leads to an optical power over 2 mW. Thus, the single μLED can be driven up to 17.7 kA/cm^2 current density, and produce an optical power density of 442.3 W/cm^2. The high current density leads to a shorter differential carrier lifetime, in turn, higher electrical modulation bandwidth. A 440 MHz 6-dB electrical modulation bandwidth of a single μLED in this array has been achieved as shown in figure 5.4 (b). This value is more than 12 times higher than the one of the typical commercial LEDs in the conventional array [10].

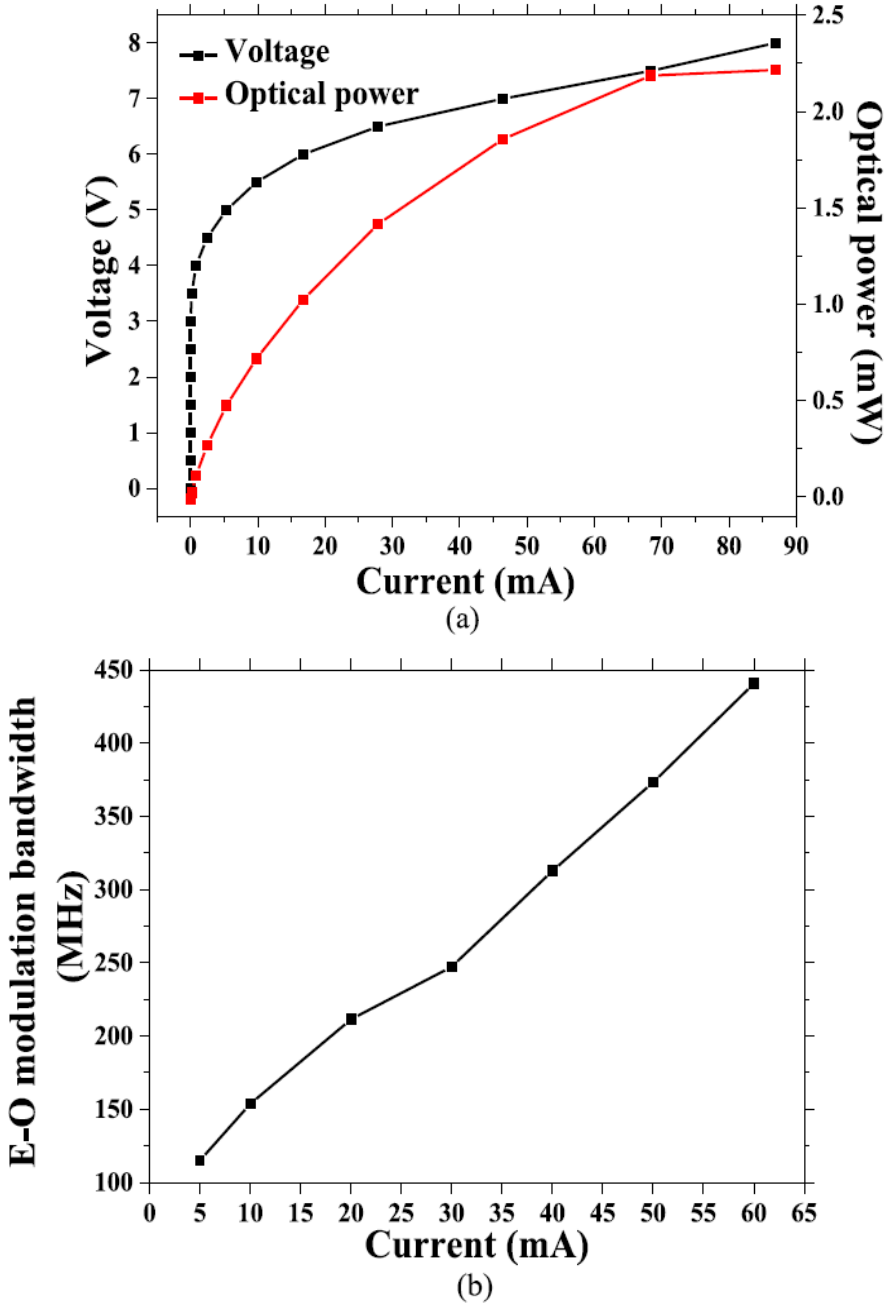

FIGURE 5.4: (a) electrical and optical, and (b) 6-dB electrical modulation bandwidth of the individual-n-addressable μLED array with NMOS driver. After [9].

For the VLC applications, the μLED yield and uniformity of the electrical and optical characteristics on the whole array are essential. It is found that the microstructure and fabrication process of the μLED array play an important role in μLED yield and uniformity. As mentioned above, there are deep gaps between

the GaN mesas in the μLED array. Since the dielectric and metal layers must be deposited over them, these gaps have a huge influence on the μLED yield. For the μLED array with a gap of 170 μm, the μLED yield is around 90 % by using the non-optimized fabrication process. However, it is found that the μLED yield decreases to 67 % when the gap between the GaN mesas is reduced to 6 μm. The reason for the yield decrease has been investigated. Our results show that the incomplete removal of photoresist residues at the mesa gaps is the main reason for the short circuit and low yield. Such photoresist residues can be seen in figure 5.5. The remaining photoresist will cause the degradation of the SiO_2 layer deposited in the following step. As a result, adjacent μLEDs are shorted producing a low yield. In the optimized process, by introducing an O_2 based plasma ashing step (200 °C, 10 mins), the photoresist residues are almost completely removed. Thus, the μLED yield of the μLED array with a mesa gap of 170 μm increases to 100 % and the μLED yield of the μLED array with a mesa gap of 6 μm increases to 95 %.

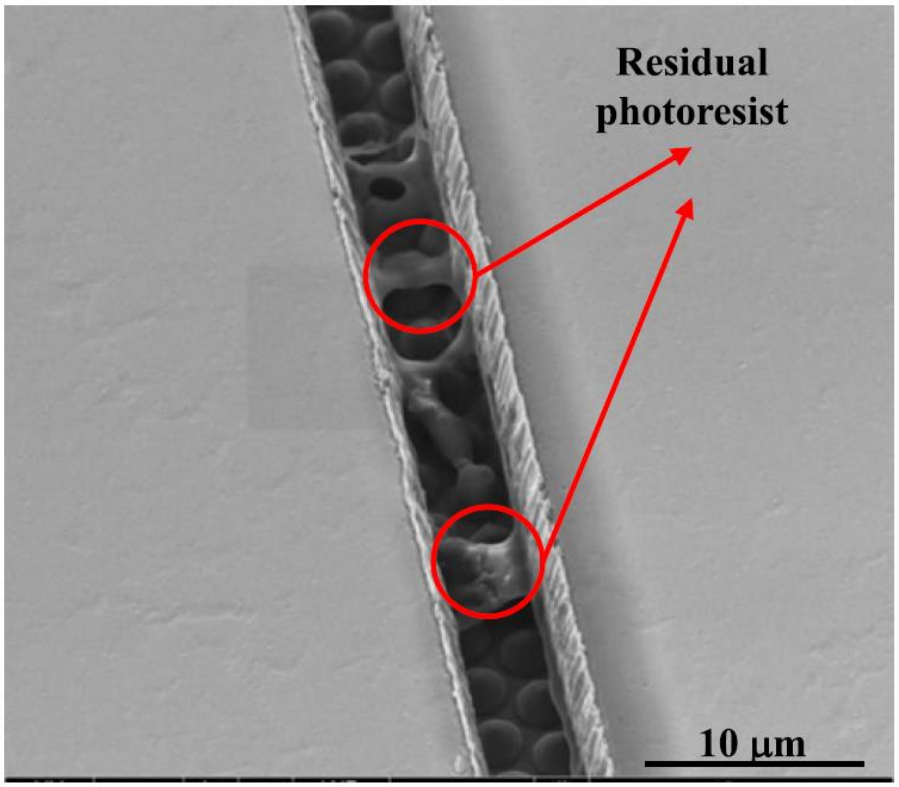

FIGURE 5.5: SEM image of photoresist residues in a 6 μm gap between two adjacent GaN mesas. The photoresist residues are highlighted by red circles. The lenticular features visible in the gap are PSS pattern as mentioned in subsection 1.3.1. After [9].

Figure 5.6 presents the variations of the applied voltage and optical power at a fixed injection current of 60 mA for 5 randomly selected μLEDs in the μLED arrays fabricated by the non-optimized and the optimized processes respectively. As figure shows, one of the μLED in the non-optimized device presents a significantly lower voltage at 60 mA than the others due to the poor metal contact. It is an undesired data to do an average or variation analyse. However, to ensure a fair comparison, this data will still take in count since these μLEDs were randomly selected. The variation for applied voltage is defined by using standard sample deviation (s) formula:

$$s = \sqrt{\frac{1}{N-1}\sum_{i=1}^{N}(x_i - \overline{x})^2} \tag{5.1}$$

Where N is the number of values in the sample, x_i is the each value, and $\overline{x}$ is sample mean. As shown in figure 5.6 (a), the variations of the applied voltage and output power of the μLEDs fabricated by non-optimized process are 0.489 and 0.042, respectively. Figure 5.6 (b) shows the variations of the applied voltage and output power of the μLEDs fabricated by optimized process, which are 0.261 and 0.044, respectively. Compared with the one fabricated by non-optimized process, the voltage variation of the optimized device improved about 47 %. The optical power variation of the optimized device is nearly the same with the one fabricated by non-optimized process. Moreover, compared with the one fabricated by non-optimized process, the average optical power of the optimized device is 11 % higher, while the average voltage at 60 mA of optimized device is 7 % lower. Therefore, the plasma ashing step is not only increasing the μLED array yield, but also raising the uniformity of the μLED array on voltage and its LEE.

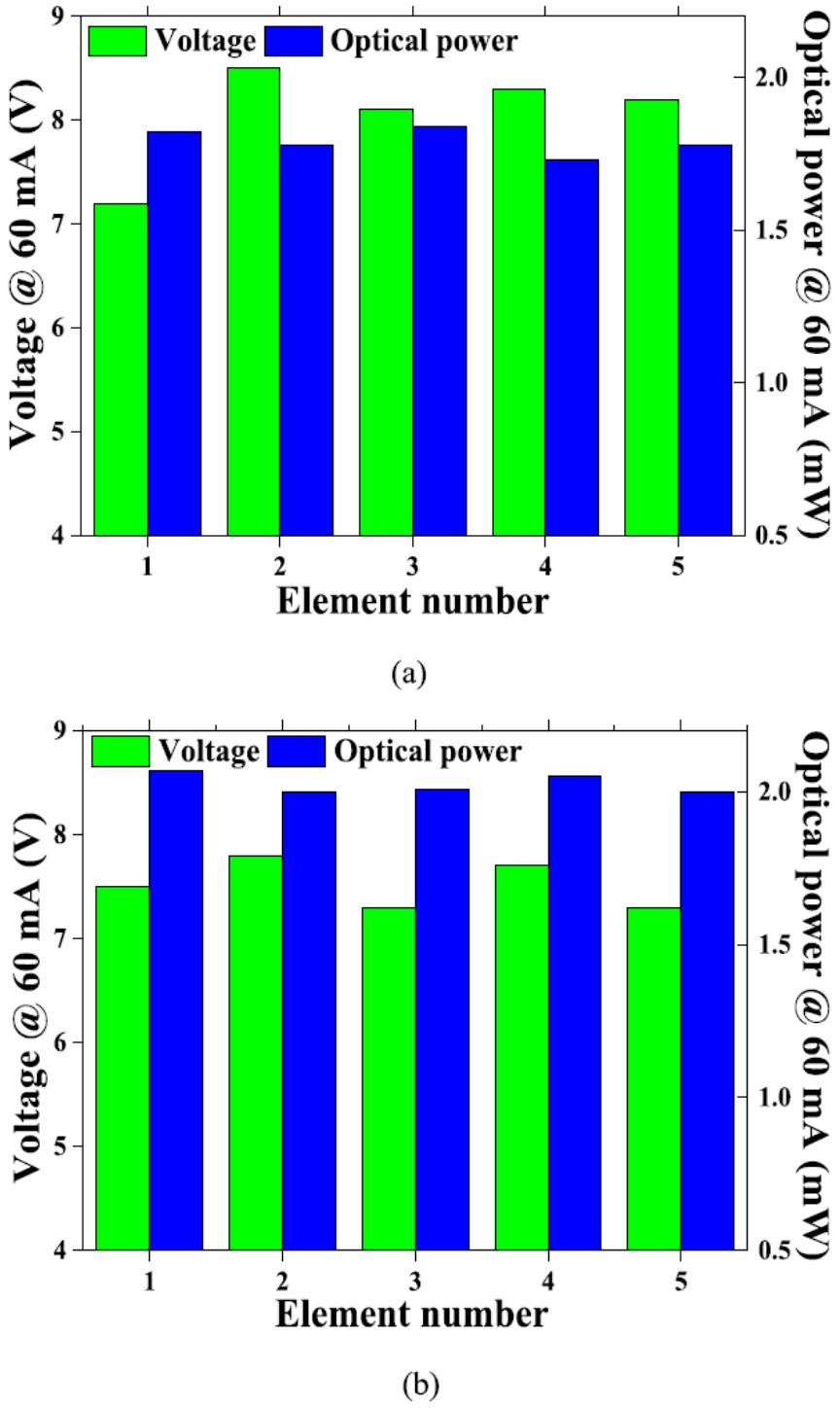

FIGURE 5.6: Voltage and optical power uniformities of 5 randomly selected μLEDs in the μLED arrays fabricated by (a) non-optimized process and (b) optimized process. After [9].

5.2.3 Driver integration and VLC application

A custom NMOS driver is used in this work. The driver contains four independent current-steering digital-to-analog converter (DAC) driver channels with 8-bit resolution. The operating current of each driver channel is up to 255 mA. The 3-dB electrical modulation bandwidth of each driver channel is 250 MHz. The μLED array chip is wired-bonded to a ceramic package which is soldered to a daughter card. The daughter card is then connected to a motherboard through four high-speed connectors. There are 40 SubMiniature Version A (SMA) connectors at the edges of the motherboard. Four of these SMA connectors are used to supply power to the motherboard. The μLED array is connected to the NMOS driver by the rest of the SMA connectors. Figure 5.7 shows the μLED array assembled on a mother board.

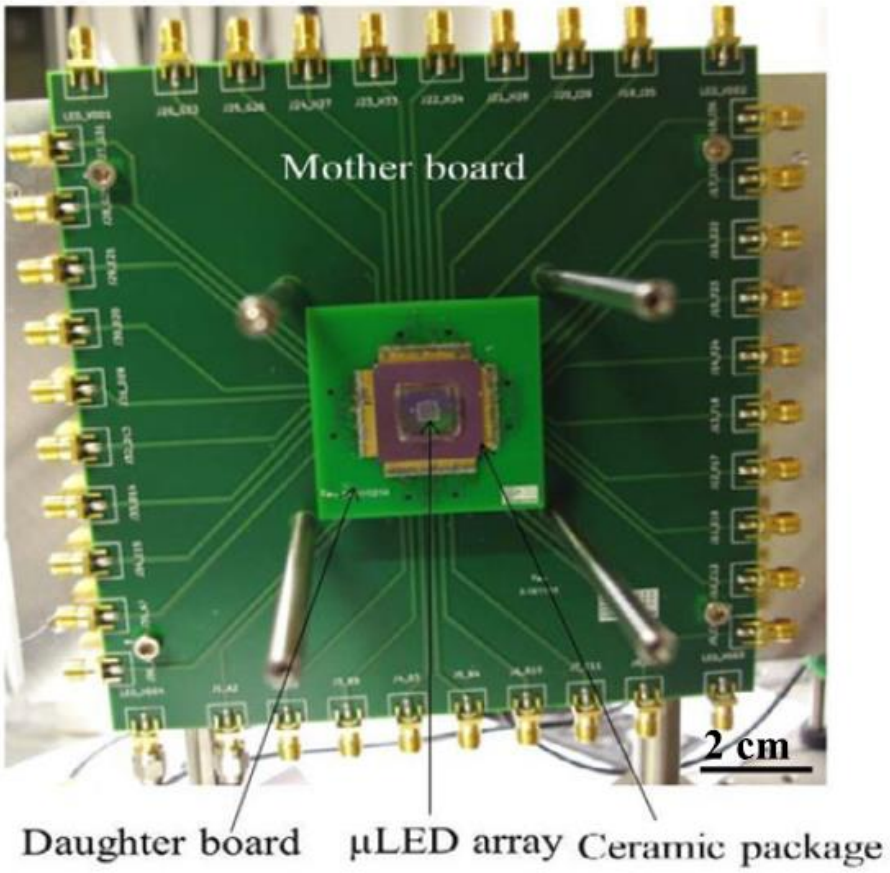

FIGURE 5.7: Optical image of the individual-n-addressable μLED array assembled on a mother board. After [9]

The VLC performance of the μLED array with integrated NMOS driver is demonstrated assuming OOK modulation scheme. The NMOS driver sends arbitrary waveforms generated by MATLAB interface to μLEDs. The waveforms are created as a 1 $\times$ X array. The signal levels correspond to integers ranging from 0-255 on an 8-bit DAC. The corresponding output current of the NMOS drivers was proportional to the received integer value for each sample period. Then the Matlab interface is used to control the clock speed of the NMOS driver to determine the symbol rate. The μLED array is connected with a power supply which was set to 9 V and limited to 70 mA for each active μLED. A Hamamatsu C5658 APD with 1 GHz bandwidth is used to collect the output responses. The data transmission distance is around 50 cm. In order to demonstrate the VLC application of the integrated devices, a pseudo-random OOK data stream was generated and

sent to the μLED though the NMOS driver. 1 and 4 μLEDs have been operated synchronously with the same waveform but driven by independent DACs. Figure 5.8 presents the received waveforms and resultant eye diagrams. A clear opening eye can be observed when a single μLED operating at 300 Mbps. A similar eye diagram can be observed when four μLED operating at 180 Mbps. Thus, a single and four μLEDs can be operated at 300 Mbps and 180 Mbps without observable bit error. The drop of data transmission rate between a single and four μLED may be caused by the heating effect. The four operating μLEDs are in close proximity to each other, which would reduce the heat dissipation since no heat sink is attached to the μLED chip.

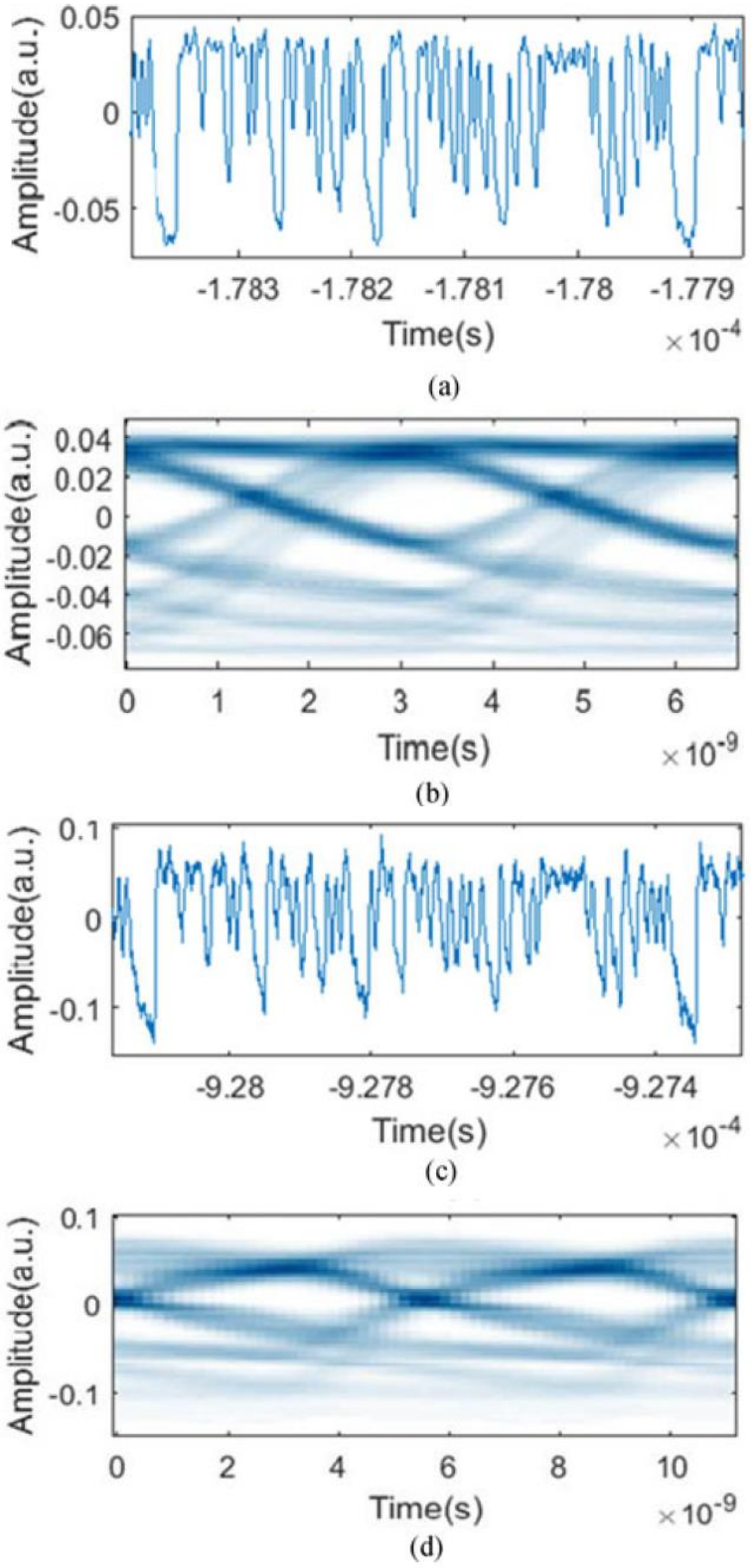

FIGURE 5.8: Received waveforms and resultant eye diagrams of (a) a single μLED operated at 300 Mbps and (b) four μLED operated at 180 Mbps. After [9].

5.3 Summary

A brief summary of the previous work about a PMOS driver controlled μLED array based VLC system is given in section 5.1. The section 5.2 presents the design, process flow development, performance characterization and VLC application of an innovative μLED array. Each μLED on the μLED array shares a common p-electrode with individually addressable n-electrodes. Therefore, it is capable with an NMOS transistor-based CMOS driver, which enables a faster modulation speed. To improve the yield and uniformity of each μLED, an optimized fabrication process with extra O_2 plasma treatment is introduced. The VLC performance of this μLED integrated with a custom NMOS transistor based CMOS driver is presented in the last section.

References

[1] H. X. Jiang, S. X. Jin, J. Li, J. Shakya, and J. Y. Lin. III-nitride blue microdisplays. *Applied Physics Letters*, 78(9):1303–1305, 2001.

[2] Z. Gong, H. X. Zhang, E. Gu, C. Griffin, M. D. Dawson, V. Poher, G. Kennedy, P. M. W. French, and M. A. A. Neil. Matrix-Addressable Micropixellated InGaN Light-Emitting Diodes With Uniform Emission and Increased Light Output. *IEEE Transactions on Electron Devices*, 54(10):2650–2658, 2007.

[3] J. J. D. McKendry, B. R. Rae, Z. Gong, K. R. Muir, B. Guilhabert, D. Massoubre, E. Gu, D. Renshaw, M. D. Dawson, and R. K. Henderson. Individually Addressable AlInGaN Micro-LED Arrays With CMOS Control and Subnanosecond Output Pulses. *IEEE Photonics Technology Letters*, 21(12):811–813, 2009.

[4] J. Day, J. Li, D. Y. C. Lie, C. Bradford, J. Y. Lin, and H. X. Jiang. III-Nitride full-scale high-resolution microdisplays. *Applied Physics Letters*, 99(3):031116, 2011.

[5] J. J. D. McKendry, D. Massoubre, S. Zhang, B. R. Rae, R. P. Green, E. Gu, R. K. Henderson, A. E. Kelly, and M. D. Dawson. Visible-Light Communications Using a CMOS-Controlled Micro-Light- Emitting-Diode Array. *Journal of Lightwave Technology*, 30(1):61–67, 2012.

[6] E. F. Schubert. *Light-Emitting Diodes*. Cambridge University Press, 2006.

[7] J. Herrnsdorf, J. J. D. McKendry, S. Zhang, E. Xie, R. Ferreira, D. Massoubre, A. M. Zuhdi, R. K. Henderson, I. Underwood, S. Watson, A. E. Kelly, E. Gu, and M. D. Dawson. Active-Matrix GaN Micro Light-Emitting Diode Display With Unprecedented Brightness. *IEEE Transactions on Electron Devices*, 62(6):1918–1925, 2015.

[8] S. M. Sze, Y. Li, and K. K. Ng. *Physics of semiconductor devices*. John Wiley & Sons, 2021.

[9] E. Xie, M. Stonehouse, R. Ferreira, J. J. D. McKendry, J. Herrnsdorf, X. He, S. Rajbhandari, H. Chun, A. V. N. Jalajakumari, O. Almer, G. Faulkner, I. M. Watson, E. Gu, R. Henderson, D. C. O'Brien, and Dawson. M. D. Design, fabrication, and application of GaN-based micro-LED arrays with individual addressing by N-electrodes. *IEEE Photonics Journal*, 9(6):1–11, 2017.

[10] J. Vučić, C. Kottke, S. Nerreter, K. Langer, and J. W. Walewski. 513 Mbit/s visible light communications link based on DMT-modulation of a white LED. *Journal of Lightwave Technology*, 28(24):3512–3518, 2010.

Chapter 6

Development and application of deep ultraviolet micro-structured light emitting diodes

In this chapter, the development of novel deep ultraviolet (DUV) μLEDs and their applications on deep UV communications are presented. In comparison with VLC, deep UV optical communications have some advantages such as very low background noise and the capability of achieving NLOS communications due to the strong scattering of deep UV light in the air. As summarized in section 6.1, previous studies on deep UV communications have been performed and reported. However, due to the low modulation bandwidth of the light sources used in these previous works, the reported data transmission rates of the deep UV communications are still quite low [1–4]. In this work, a deep UV μLED device emitting at 262 nm was developed. The characterization of this deep UV μLED and its application on deep UV communications are presented in section 6.2. The deep UV data transmission rate achieved in this work is more than 15 times higher than the previously reported results in UV-C wavelength band, which demonstrates the great potential of the μLEDs for deep UV communications.

6.1 Review of deep UV communications

As presented in chapter 4, the developments of LED wafer growth technologies in visible region and μLED fabrication techniques have enabled us to achieve LED based VLC systems with fast data transmission rates and long data transmission distances. However, as mentioned in section 1.4, there are some issues in free space visible light communications. For example, the solar radiation in visible region has a strong influence on the outdoor VLC links due to the high background noise. Moreover, the VLC links are point to point links, which have high pointing, acquisition and tracking requirements. Deep UV communication provides promising solution to such issues. As summarised in section 1.4, most of the solar UV radiation especially in the UV-C band between 200 nm and 280 nm is absorbed by the ozone layer in Earth's stratosphere. The deep UV radiation at ground level is negligible [5]. Thus, both indoor and outdoor deep UV wireless communication have negligibly low background noise [6]. Meanwhile, a NLOS communication link can be constructed by using deep UV light sources due to the strong scattering of the deep UV light in the air [7, 8], reducing the pointing, acquisition and tracking requirements. Furthermore, deep UV communication links on outer space would be highly secure since deep UV radiation is strongly absorbed by the ozone layer in Earth's stratosphere. It enables safe communication links between satellites which would be hardly traceable at ground level. Due to the fast development of deep UV light sources, filters and detectors [1, 2], many research efforts concentrated on deep UV communication have been made recently. In 1985, a Pulse modulating based deep UV NLOS communication system with a data transmission rate of 10 kbps at 0.5 km distance was reported by using a 253 nm mercury-argon lamp as a light source [4]. A 1.2 Mbps data transmission rate at 1.6 km was demonstrated in 1990 by using a 265 nm mercury-xenon lamp in a deep UV NLOS communication system [3]. A custom-made electro-optic modulator with 400 kHz was used to modulated the light source. In 2007, a report showed a 1.2 kbps data transmission rate at 6 m by using a 254 nm low pressure mercury lamp as a light source

in a digital NLOS communication system [1]. In 2012, 265 nm LED arrays were used for a Pulse modulating based deep UV NLOS communication system, which achieved a 2.4 kbps data transmission rate at 10 m [2]. A 71 Mbps data transmission rate was achieved in a OFDM based light-of-sight deep UV communication in 2017 by using a 294 nm LED [9]. In 2018 European Conference on Optical Communication, a 1.6 Gbps data transmission rate was claimed at 1.5 m by using a 280 nm LED in a PAM based deep UV communication system[6]. However, the FEC level using in the report is different from the standard one, which was 2.0 $\times$ 10 $^{-2}$. Therefore, this reported data transmission rate at the standard FEC level of 3.8 $\times$ 10 $^{-3}$ is still quite low [10]. The low modulation bandwidths of the deep UV light sources used in these systems would be the main reason for the low data transmission rates. As mentioned above, deep UV flashtubes or lamps were used in the early works, which have very low modulation bandwidths, typically less than 40 kHz [3]. Based on the reported data, such light sources can only offer modulation bandwidths less than 40 kHz. In recent works, semiconductor UV LEDs have been used as light sources for deep UV communication. These semiconductor UV LEDs can provide much higher modulation bandwidth than the one from UV flashtubes or lamps. However, due to the large chip size of the conventional LEDs, the resistance-capacitance time constant in these LEDs would dominate the performance of their modulation bandwidth instead of the carrier life time. Therefore, the further increase in modulation bandwidth of these LEDs is limited. A recent reported modulation bandwidth of a deep UV LED was 29 MHz [9]. Thus, it is of paramount importance to develop novel deep UV light sources with high modulation bandwidths for high-speed deep UV communications. As mentioned in chapter 4, μLEDs can provide high modulation bandwidths and thus are promising light sources for deep UV communications. In the following sections, the design, fabrication, characterization and communication application of the deep UV μLEDs are given.

6.2 Fabrication, characterization and communication application of deep UV micro-structured light emitting diodes

6.2.1 Fabrication and characterization of deep UV micro-structured light emitting diodes

In this work, the deep UV or UV-C μLEDs are fabricated from a commercial AlGaN-based LED wafer, which grown on a c-plane sapphire substrate with a 262 nm emission wavelength. The epitaxial structure of this wafer includes a 2 μm-thick AlN buffer layer, a 2 μm thick n-doped $Al_{0.6}Ga_{0.4}N$ layer, an active region consisting of 6-period AlGaN-based QWs with a 2.5 nm thick well and 13 nm thick barrier, a 50 nm thick $Al_{0.6}Ga_{0.4}N$ electron blocking layer (EBL) and finally a 310 nm thick p-doped GaN layer. The Al compositions in the wells and barriers are estimated as 45 % and 55 %, respectively.

The design and structure of the deep UV μLED array fabricated in this work are similar to the one mentioned in section 4.1. Figure 6.1 presents the schematic cross-sectional structure of a single UV-C μLED. Figure 6.2 (a) and (b) show the optical image of the fabricated UV-C μLED array and a high-magnification image of the μLEDs, respectively. The fabricated UV-C μLED array contains 15 μLEDs in a flip-chip configuration. The emission area of each trapezoidal shaped μLED is 566 μm^2. This area is equivalent to a disk-shape μLED with a diameter of 27 μm. Each μLED is individually addressed by its corresponding anode with a shared cathode. The fabrication process of the UV-C μLED array is given below. The μLED structure was created by two Cl_2-based ICP etching processes. The first etching process was used to define 15 μLEDs, which was terminated at the n-type AlGaN layer. The second etching process was used to create an n-type AlGaN mesa, which terminated at sapphire substrate. Then, an annealed Pd layer with a

thickness of 100 nm was used as the quasi-ohmic p-type metal contact (the $I-V$ characteristics of this contact is closed to linearity, but not really linearity) to p-type GaN [11]. The n-type contact and metal tracks to connect the μLEDs were constructed by a metal bilayer of Ti/Au (50 nm/300 nm). In this work, all the measurements were performed on bare, unpackaged μLED die.

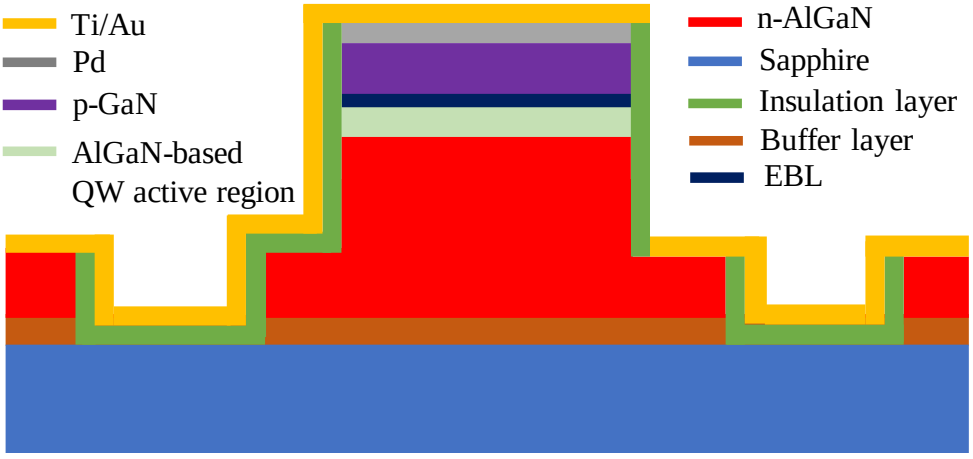

FIGURE 6.1: Schematic of single UV-C μLED used in this work. After [12].

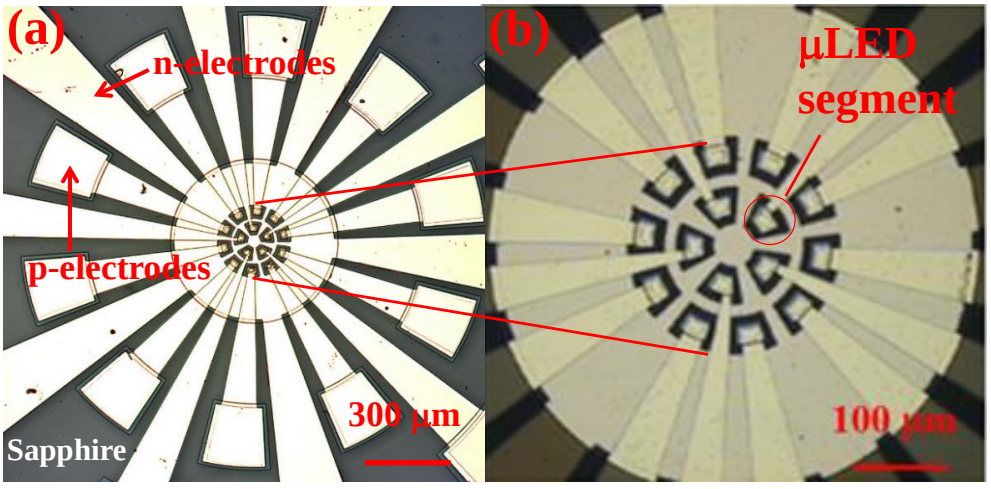

FIGURE 6.2: (a) Optical image of the fabricated UV-C μLED array (b) a high-magnification image of the μLEDs. After [12].

The typical current density-voltage (J-V) and optical power-current density (L-J) plots of a single UV-C μLED fabricated in this work are presented in figures 6.3. The emission spectrum of the UV-C μLED at 1768 A/cm^2 is shown in the

inset in figures 6.3. Both *J-V* and *L-J* data are measured at the same time by placing a UV-enhanced Si photodetector in close proximity to the polished sapphire substrate of the μLED. As the *J-V* curve shows, the turn-on voltage of the μLED is 13 V at 180 A/cm^2 (1mA), which is consistent with the reported one in previous work on broad-area UV-C LEDs [13]. The high contact resistivity of metal contact to the n-type $Al_{0.6}Ga_{0.4}N$ layer is the main reason to cause this high turn-on voltage of the UV-C μLED. The high Al composition (60 %) in this n-type $Al_{0.6}Ga_{0.4}N$ layer results in difficult to achieve high quality ohmic contact [14]. I am currently working on the optimization of the metal contact to the n-type $Al_{0.6}Ga_{0.4}N$ layer in order to reduce the turn-on voltage of these UV-C μLEDs. Several different metal schemes and annealing processes will be tested in the near future. As figures 6.3 shows, the driving current density of this μLED is up to 3400 A/cm^2 before thermal rollover, which is much higher than the current densities (125 A/cm^2) that conventional deep-UV LEDs can sustain [15]. A unidirectional optical output power of the μLED at this current density is 196 μW at the sapphire substrate surface, which corresponding to an optical power density of 35 W/cm^2.

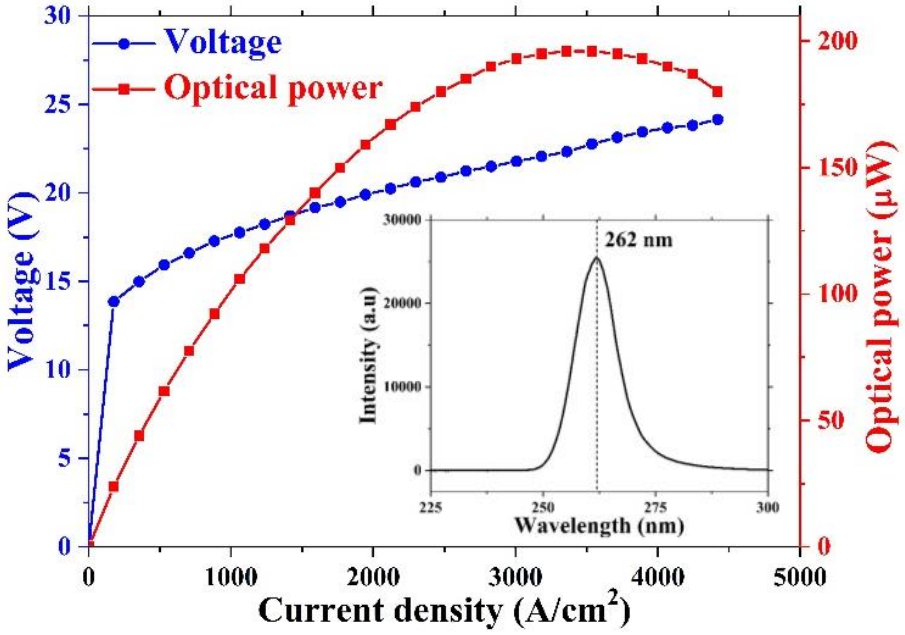

FIGURE 6.3: *J-V* and *L-J* performance of a single UV-C LED fabricated in this work. The inset shows the emission spectrum of the μLED. After [12].

For μLEDs, thanks to the small chip size, their modulation bandwidth is mainly dominated by the differential carrier lifetime rather than the RC time constant [16]. When the operating current density of a μLED increases, the differential carrier lifetime is reduced, thus, the modulation bandwidth increases. Furthermore, it has been shown that the μLEDs can sustain much high operating current densities compared with conventional LEDs. Therefore, a high modulation bandwidth is expected for the UV-C μLEDs fabricated in this work. In order to verify this, the frequency responses of these UV-C μLEDs are measured by the method mentioned in section 4.1. A bias tee (SHF BT45-D) is used to combine a DC-bias current with an alternating current frequency sweep signal generated by a network analyzer, then the combined current is sent to modulate the μLED. Two UV-enhanced optical lenses are used to collect the optical response from the μLED. The collected optical response is then focused by a UV-enhanced objective lens into a UV-enhanced Si APD detector [Thorlabs APD430A2(/M)] with a specified output 3-dB electrical bandwidth between DC to 400 MHz. The revived response was then fed back to the network analyzer. As mentioned above, the APD detector used only has 400 MHz of 3-dB electrical bandwidth. Therefore, it has a great chance to be saturated by the μLEDs since they can offer high modulation bandwidth [12]. To order to indicate such issue, a comparison between the APD detector and the μLED is needed. Thus, the frequency response of the μLED will be presented in 3-dB, which will be slightly different compared with the one in chapter 4 and 5. The measured 3-dB electrical modulation bandwidth of the UV-C μLED as a function of current density is presented in figure 6.4 (a). As shown, the measured modulation bandwidth of the μLED increases linearly when the current density increases from 18 to 71 A/cm^2. This performance is consistent with the relationship between the modulation bandwidth and current density reported in our group's early work on visible μLEDs [17]. By further increasing the current density from 71 A/cm^2, the measured modulation bandwidth becomes saturated at around 438 MHz with slight variation (less than 2 MHz). To study this saturation, I compared the measured frequency responses of the μLED at current

densities of 18 A/cm^2 and 71 A/cm^2, which are highlighted by the red and blue circles in figure 6.4 (a). Figure 6.4 (b) presents the measured frequency response of the μLED at current density of 18 A/cm^2, and figure 6.4 (c) presents the measured frequency response of the μLED at current density of 71 A/cm^2. It is clear that the frequency response at 71 A/cm^2 shows a sharp drop when increasing the modulation frequency to around 450 MHz, which is similar to the frequency response of the APD detector used in the work. It indicates that the observed saturation of the measured modulation bandwidth is actually caused by the APD rather than the μLED itself [18–20]. Therefore, I expect the real modulation bandwidth of the UV-C μLED to be much higher than 438 MHz. To test this, a deep-UV PIN detector with a high bandwidth (2GHz) has been used. However, due to the low optical power of the UV-C μLED and the low sensitivity of this PIN detector, no useful signal could be detected. Nevertheless, the measured 438 MHz 3-dB electrical modulation bandwidth of the UV-C μLED is already around 3 times higher than the one reported (153 MHz) [11]. Moreover, the UV-C μLED shows a much higher modulation bandwidth than the visible *c*-plane μLEDs used in my previous work (presented in chapter 4 and 5), even at low current densities. As mentioned before, the modulation bandwidths of μLEDs are dominated by their differential carrier lifetime. The differential carrier lifetime (τ) consists of radiative recombination lifetime (τ_r) and non-radiative recombination lifetime (τ_{nr}), which can be expressed as [16]:

$$\tau^{-1} = \tau_r^{-1} + \tau_{nr}^{-1} \tag{6.1}$$

It is well known that the quality of AlGaN-based deep-UV LED is relatively low due to the high-density defects generated in the material growth process [21]. As a result, the UV-C μLEDs have a shorter non-radiative recombination lifetime compared with the one of visible μLEDs, in turn, a large modulation bandwidth.

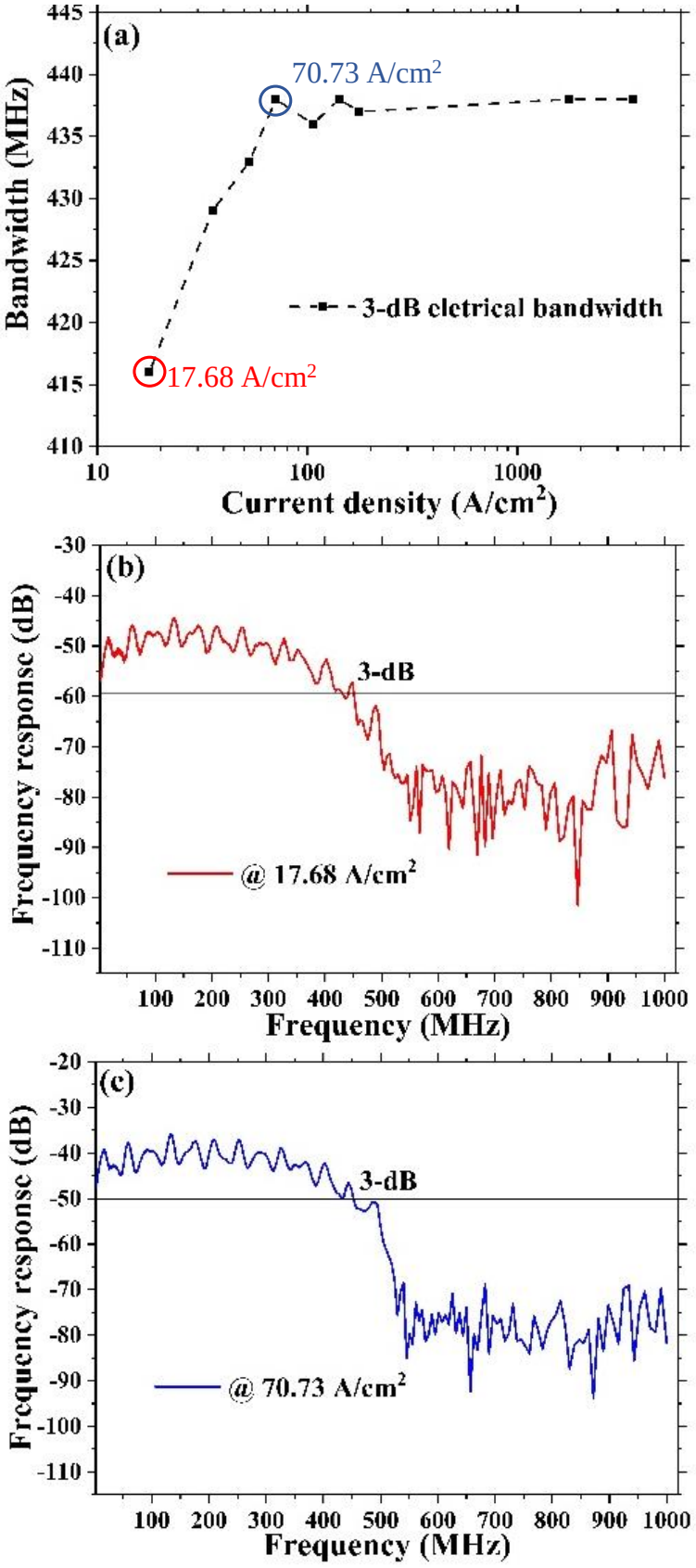

FIGURE 6.4: (a) The 3-dB electrical modulation bandwidth of the UV-C μLED as function of current density, (b) small signal frequency response of the UV-C μLED at 18 A/cm^2 (3-dB scale plotted), and (c) small signal frequency response of the UV-C μLED at 71 A/cm^2(3-dB scale plotted). After [12].

6.2.2 Deep UV communications with a UV-C μLED light source

Based on the fabricated UV-C μLED, a deep UV wireless communication system is implemented. In this experiment, both single-carrier OOK and multi-carrier OFDM modulation schemes are applied in order to demonstrate the capability of the fabricated μLED for deep UV communication. A schematic diagram and an optical image of the system developed in this work are presented in figure 6.5. As figure shown, an arbitrary waveform generator (AWG; Keysight 81180B) is used to map both OOK and OFDM waveforms generated in MATLAB. These analog signals are amplified by an amplifier (ZHL-6A-S+), and then combined with a DC bias current by using a bias tee. A high speed micro probe is used to apply these combined signals to the UV-C μLED. The modulation signal depths (V_{PP}) and DC bias current densities (J_{DC}) used in the experiments are determined by extensive tests to achieve high system performance. Based on these tests, the V_{PP} and J_{DC} are set as 2 V and 1410 A/cm^2 for the OOK modulation scheme, respectively. The V_{PP} and J_{DC} are set as 7 V and 1770 A/cm^2 for the OFDM modulation scheme, respectively. A UV enhanced lens is used to collect and focus the light emitted from the UV-C μLED to a UV-enhanced Si APD detector. The distance between the μLED and the APD detector is around 0.3 m. The output signal of the APD detector is then fed back to a digital oscilloscope (Keysight, MSO7104B) and processed offline in MATLAB. Here I must emphasize that only 20 % of the emitted light power was received by the APD detector due to a combination of light scattering and non-optimized collection optics. It means that around 26 μW and 30 μW optical powers are fed into the APD detector for the OOK and OFDM modulation schemes in the experiments, respectively. The improvement of the system is ongoing in order to increase the received power.

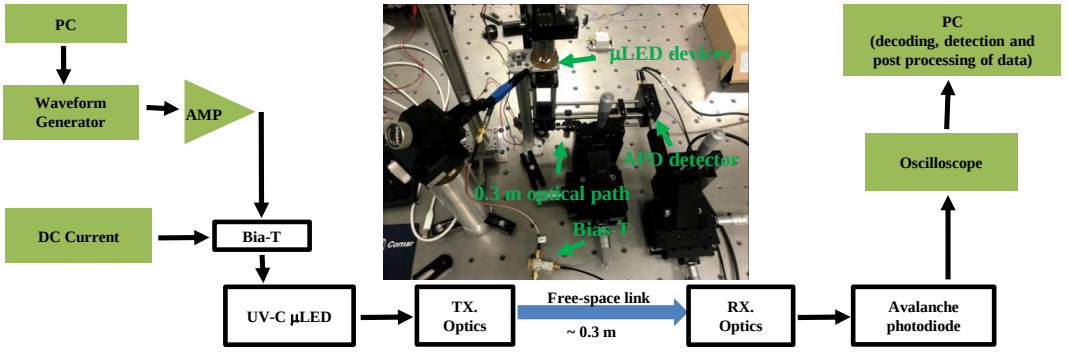

FIGURE 6.5: Schematic diagram and optical image of the experimental setup for deep UV communication based on the fabricated UV-C μLED. After [12].

For the OOK modulation scheme, two information symbols are first mapped to different amplitudes and then further referred to as transmitted symbols. Non-return-to-zero (NRZ) symbols are used, and the set of transmitted symbols is {-1,1}. Before the transmitted symbols are sent to the AWG, a root raised cosine filter is used to minimize the intersymbol interference (ISI) which is caused by the amplitude and delay distortions from the communication channel. To obtain the received symbol, the received signal was filtered by a matched filter and down-sampled. The normalized number of occurrences of transmitted and received symbols of OOK represented by histograms at 800 Mbps are shown in figure 6.6 (a). It is clear that the distribution of received symbols before the equalizer (blue parts) is negative-side heavier compared with the one of transmitted symbols (black parts). It means that the ISI still has a huge influence to the system [22]. In order to overcome this issue, a feed-forward equalizer based on the recursive least-squares updating algorithm is deployed. The received symbols which go beyond a decision threshold is estimated by the equalizer and then decoded to their nearest transmitted symbols. As shown in figure 6.6 (a), the spread of received symbols (brown parts) becomes narrow after the equalization. As a result, a low BER is achieved, which reduced the decoding errors due to the ability to distinguish the correctly transmitted symbols at the receiver. Figure 6.6 (b) demonstrates the eye diagram of the equalized received signal under the OOK modulation scheme at 800 Mbps. The open eyes can be clearly observed in the Figure, which presents a

communication link with a low BER. Due to the limitation of the bandwidth of the APD detector, higher data transmission rates cannot be measured.

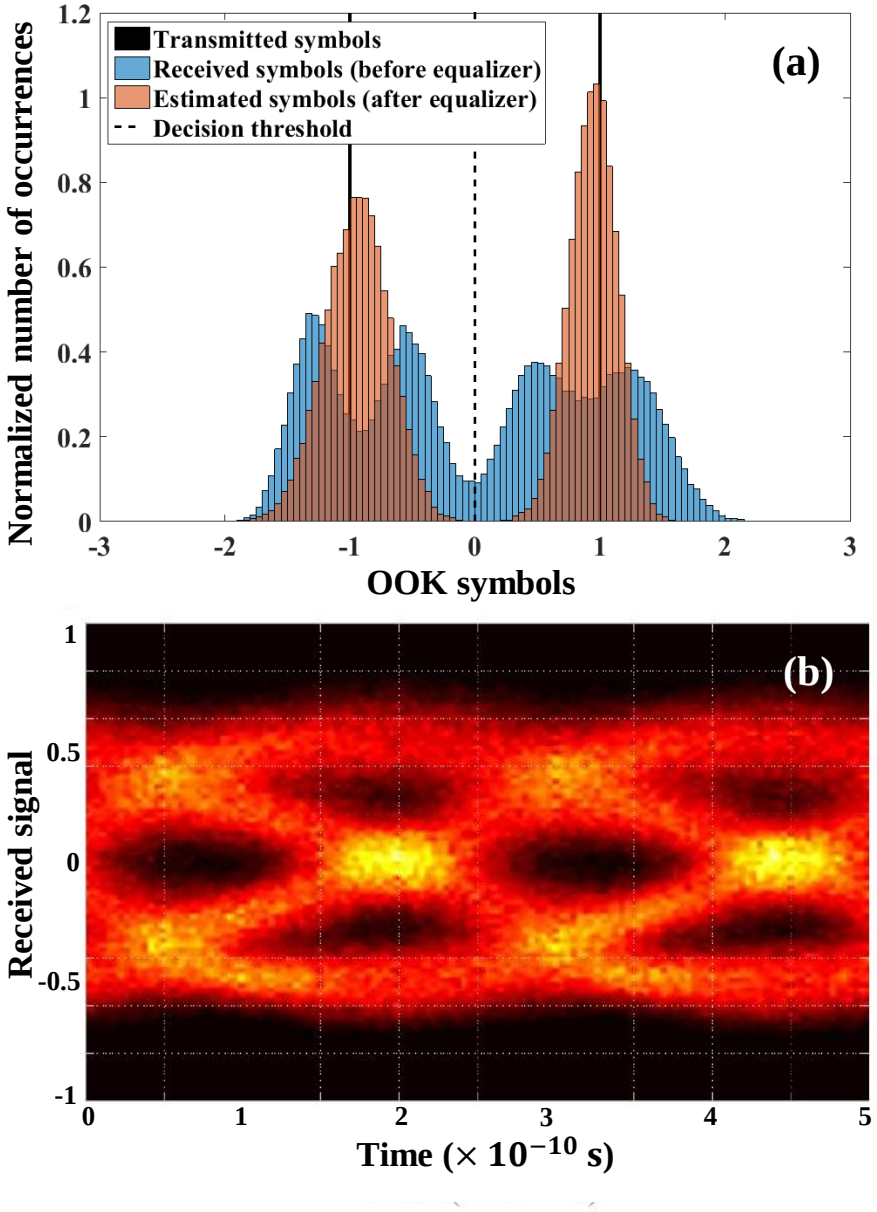

FIGURE 6.6: (a) Normalized number of occurrences of transmitted and received symbols assuming the OOK modulation scheme at 800 Mbps and (b) the eye diagram of received symbols assuming the same measurement conditions using the UV-C μLED. After [12].

It is well known that the influence of ISI on the BER in a single-carrier modulation scheme would become more pronounced with the increase of the data

transmission rate. It would make the equalizer more computationally complex for high speed communications [23]. OFDM with a single tap equalizer is a cost effective way to overcome this issue. OFDM is a method of encoding digital data on multiple carrier frequencies, which is done by modulating binary bits into (M-QAM) symbols. The M is the constellation order. Afterwards, different constellation sizes are loaded on the subcarriers using the adaptive bit and energy loading based on the available SNR. An IFFT is applied to multiplex $N_{FFT}/2$-1 QAM symbols into N_{FFT} subcarriers. A real-value output is guaranteed by introducing Hermitian symmetry on the OFDM frame. A DC bias is imposed to shift the negative OFDM samples to positive [24]. The sampling frequency of the AWG and the oversampling factor of the root raised cosine in this measurement are set as 4 GS/s (gigasamples per second, which is a measure of the digitizing rate of the scope) and 4, respectively. Fast Fourier transformation (FFT) is applied on the received signal, and the received QAM symbols are equalized using the estimated channel. Figure 6.7 (a) presents the measure SNR against bandwidth of the UV-C μLED at J_{DC} = 1770 A/cm^2 and V_{PP} = 7 V. The inset shows the recovered M-QAM constellations for M= 4, 8, 16. An over 5 dB SNR is achieved at a 480 MHz of bandwidth, which is suitable for the decoder to distinguish the transmitted symbols from M-QAM constellations for M = 4, 8, 16. This enables a high speed deep UV communication. The measured data transmission rates against BER under OFDM modulation scheme are shown in figure 6.7 (b). As shown, an over 1.1 Gbps data transmission rate is achieved at the BER of 3.8 $\times$ 10 $^{-3}$.

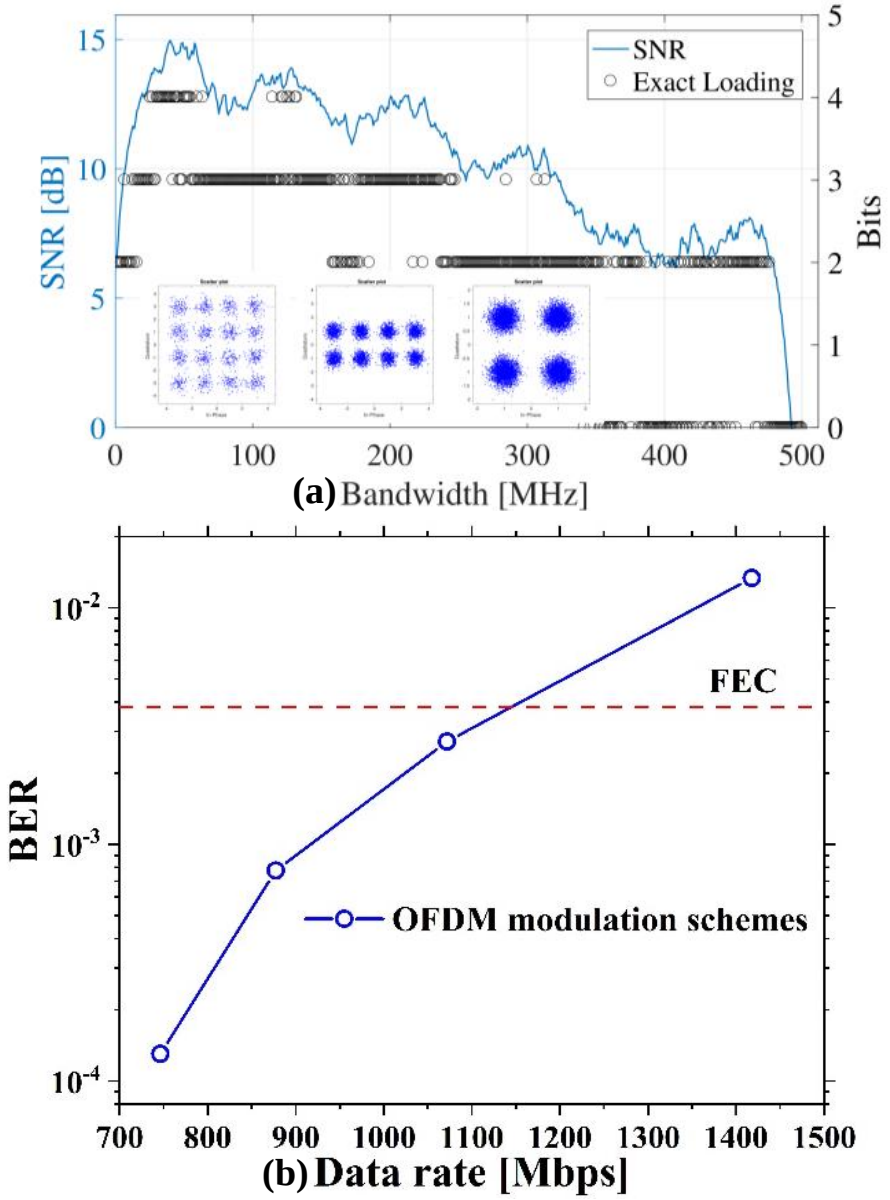

FIGURE 6.7: (a) Measured SNR against bandwidth under OFDM modulation scheme at $J_{DC} = 1770$ A/cm^2 and $V_{PP} = 7$ V. The insert is received M-QAM constellation symbols for $M = 4, 8, 16$. (b) Data transmission rate against BER under OFDM modulation scheme at $J_{DC} = 1770$ A/cm^2 and $V_{PP} = 7$ V. After [12].

As mentioned above, the bandwidth of the APD detector used in this work [Thorlabs APD430A2(/M)] is the main limitation for the performance of the deep UV communication system. To overcome this issue, a customized APD detector (Hamamatsu C5668-8867) is applied into the system. The new APD detector

has a 3-dB electrical modulation bandwidth of 1 GHz. Figure 6.8 (a) shows the measured 3-dB electrical modulation bandwidths of the UV-C μLED at different driving current densities. The measurement is performed by using the new APD detector and an upgraded network analyze (PicoVNA 106) under the same setup as mentioned above. As shown, up to 1045 MHz 3-dB electrical modulation bandwidth is achieved at a driving current density of 1060 A/cm^2. However, it can be seen that the measured modulation bandwidth doesn't increase further with increasing the driving current density. As indicated, the bandwidth of this new APD detector is 1 GHz. Thus, the measurable maximum bandwidth of the UV-C μLED is still limited by the detector. The slight decrease of the modulation bandwidth at high current densities is perhaps due to overheating of the UV-C μLED. Figure 6.8 (b) presents the data transmission rate against BER measured by using the new APD detector. The experiment setup is similar to the one mentioned above, only the data transmission distance was increased to 1.1 m. The J_{DC} and V_{PP} are 2827 A/cm^2 and 5.07 V, respectively. As shown, a new record of data transmission rate of 3.36 Gbps at the BER of 3.8 $\times$ 10 $^{-3}$ is achieved. Table 6.1 shows the comparation of my deep UV communication results and those from other published works. In the table, mercury-xenon lamp refers to MXL, mercury-argon lamp refers to MAL, and the low pressure mercury lamp refers to LPML. It can be seen that I have achieved the highest data transmission rate at the BER of 3.8 $\times$ 10 $^{-3}$, thanks to the high bandwidth character of the UV-C μLED. Currently, the data transmission distance is limited by the optical power produced from the UV-C μLED. It is expected that by further optimizing the fabrication process, the optical output power of UV-C μLEDs will increase substantially.

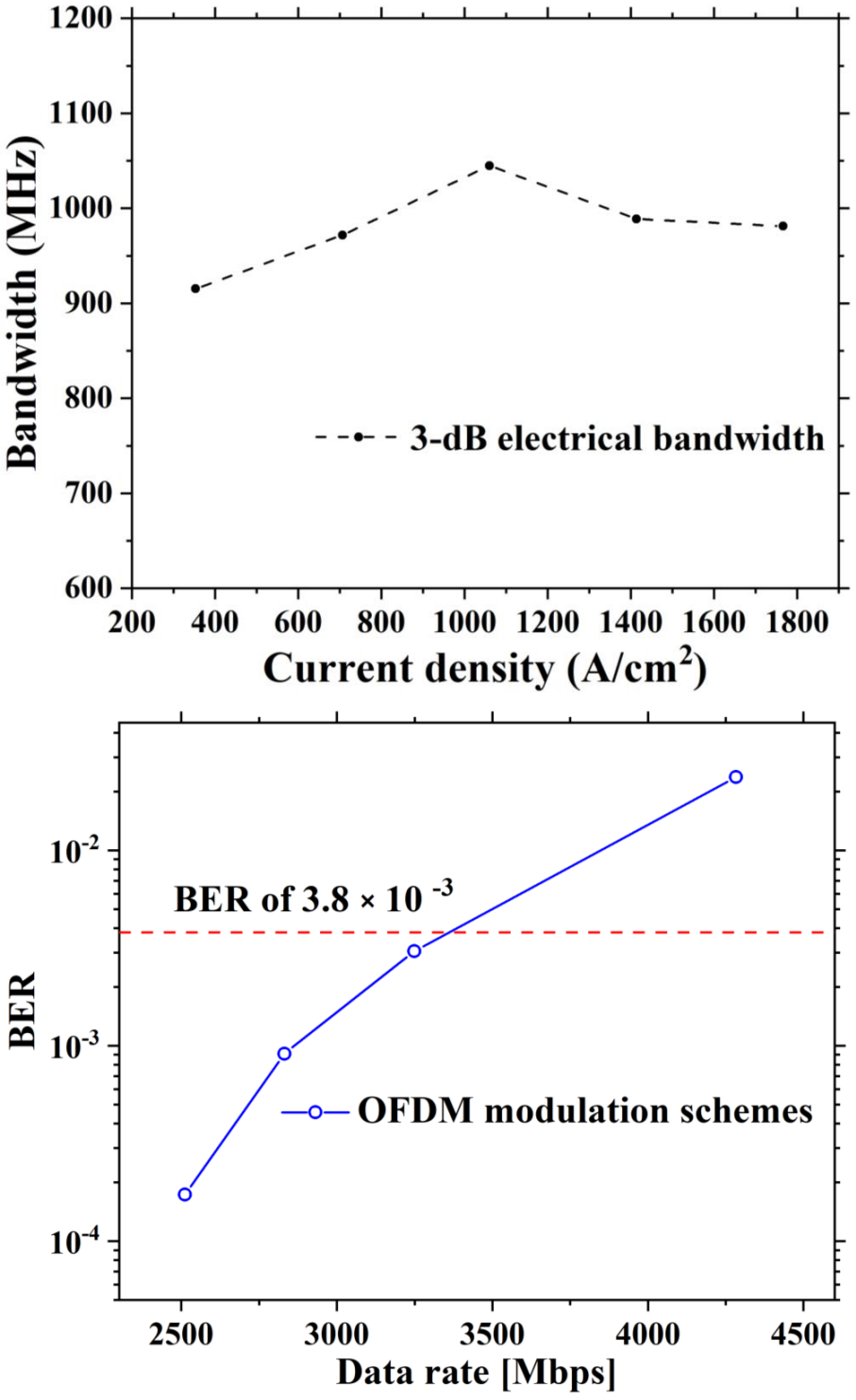

FIGURE 6.8: (a) Measured 3-dB modulation bandwidth of the UV-C μLED at different driving current densities. (b) Data transmission rate against BER under OFDM modulation scheme at J_{DC} = 2827 A/cm^2 and V_{PP} = 5.07 V.

TABLE 6.1: Comparison of deep UV communication results from the literature, compared to this work

Light source	Modulation Scheme	Transmission Power	Channel Length	Data Rate	BER	Ref
265 nm MXL	PPM	25 W	1.6 km	1.2 Mbps	-	[3]
253 nm MAL	PPM	5 W	0.5 km	10 kbps	10^{-5}	[4]
254 nm LPML	FSK	—	6 m	1.2 kbps	10^{-4}	[1]
265 nm LEDs	OOK/PPM	43 mW	10 m	2.4 kbps	10^{-4}	[2]
294 nm LED	OFDM	190 μW	0.08 m	71 Mbps	3.8×10^{-3}	[9]
280 nm LED	PAM-4	190 μW	1.5 m	1.6 Gbps	2.0×10^{-2}	[6]
262 nm μLED	OFDM	196 μW	1.1 m	3.36 Gbps	3.8×10^{-3}	This work

6.3 Summary

In summary, this chapter presents the design, fabrication, and performance of the III-nitride UV-C μLEDs. Each UV-C μLED could be driven up to a DC current density of 3400 A/cm^2 with a directed optical power up to 196 μW. The measured 3-dB electrical modulation bandwidth of the UV-C μLEDs is given, which is much higher than the reported bandwidth of conventional deep UV LEDs. The UV-C μLED is further used as a light source in a free-space deep UV communication system. The record of 3.36 Gbps data transmission rate at a BER of 3.8×10^{-3} has been achieved under OFDM modulation schemes. The high data transmission rates demonstrate the great potential of μLEDs for line-of-sight deep UV communications. Since the potential of the μLEDs for line-of-sight deep UV communications has been presented, it is of paramount importance to demonstrate the potential of the μLEDs for NLOS deep UV communication system. Generally, the transmission distance of the NLOS deep UV communication system is over few kilometres. Thus, compared with line-of-sight deep UV communication system, NLOS deep UV communication system requires higher optical power of the light sources. Therefore, in order to construct a NLOS deep UV communication system, it is clearly that the optical power of the deep UV μLEDs need to be improved. The future works will focus on improving the optical power of the deep UV μLEDs, and constructing a NLOS deep UV communication system.

References

[1] T. Feng, F. Xiong, Q. Ye, Z. Pan, Z. Dong, and Z. Fang. Non-line-of-sight optical scattering communication based on solar-blind ultraviolet light. In *Optical Transmission, Switching, and Subsystems V*, volume 6783, page 67833X. International Society for Optics and Photonics, 2007.

[2] D. Han, Y. Liu, K. Zhang, P. Luo, and M. Zhang. Theoretical and experimental research on diversity reception technology in NLOS UV communication system. *Optics Express*, 20(14):15833–15842, 2012.

[3] J. J. Puschell and R. Bayse. High data rate ultraviolet communication systems for the tactical battlefield. In *Tactical Communications Conference, 1990. Vol. 1. Tactical Communications. Challenges of the 1990's, Proceedings of the*, pages 253–267. IEEE, 1990.

[4] M. Geller, T. E. Keenan, D. E. Altman, and R. H. Patterson. Optical non-line-of-sight covert, secure high data communication system, January 8 1985. US Patent 4,493,114.

[5] Z. Xu and B. M. Sadler. Ultraviolet communications: potential and state-of-the-art. *IEEE Communications Magazine*, 46(5):67–73, 2008.

[6] K. Kojima, Y. Yoshida, M. Shiraiwa, Y. Awaji, A. Kanno, N. Yamamoto, and S. Chichibu. 1.6-Gbps LED-Based Ultraviolet Communication at 280 nm in Direct Sunlight. In *2018 European Conference on Optical Communication (ECOC)*, pages 1–3. IEEE, 2018.

[7] S. Karp, R. M. Gagliardi, S. E. Moran, and L. B. Stotts. *Optical channels: fibers, clouds, water, and the atmosphere*. Springer Science & Business Media, 2013.

[8] D. E. Sunstein. *A scatter communications link at ultraviolet frequencies.* PhD thesis, Massachusetts Institute of Technology, 1968.

[9] X. Sun, Z. Zhang, A. Chaaban, T. K. Ng, C. Shen, R. Chen, J. Yan, H. Sun, X. Li, J. Wang, J. Li, M. S. Alouini, and B. S. Ooi. 71-Mbit/s ultraviolet-B LED communication link based on 8-QAM-OFDM modulation. *Optics Express*, 25(19):23267–23274, 2017.

[10] R. X. G. Ferreira, E. Xie, J. J. D. McKendry, S. Rajbhandari, H. Chun, G. Faulkner, S. Watson, A. E. Kelly, E. Gu, R. V. Penty, I. H. White, D. C. O'Brien, and Dawson. M. D. High bandwidth GaN-based micro-LEDs for multi-Gb/s visible light communications. *IEEE Photonics Technology Letters*, 28(19):2023–2026, 2016.

[11] E. Xie, M. Stonehouse, R. Ferreira, J. J. D. McKendry, J. Herrnsdorf, X. He, S. Rajbhandari, H. Chun, A. V. N. Jalajakumari, O. Almer, G. Faulkner, I. M. Watson, E. Gu, R. Henderson, D. C. O'Brien, and Dawson. M. D. Design, Fabrication, and Application of GaN-Based Micro-LED Arrays With Individual Addressing by N-Electrodes. *IEEE Photonics Journal*, 9(6):1–11, 2017.

[12] X. He, M. S. Xie, E.and Islim, A. A. Purwita, J. J. D McKendry, E. Gu, H. Haas, and M. D. Dawson. 1 Gbps free-space deep-ultraviolet communications based on III-nitride micro-LEDs emitting at 262 nm. *Photonics Research*, 7(7):B41–B47, 2019.

[13] N. Maeda, M. Jo, and H. Hirayama. Improving the Efficiency of AlGaN Deep-UV LEDs by Using Highly Reflective Ni/Al p-Type Electrodes. *Physica Status Solidi (a)*, 215(8):1700435, 2018.

[14] M. Kneissl. A brief review of III-nitride UV emitter technologies and their applications. In *III-nitride ultraviolet emitters*, pages 1–25. Springer, 2016.

[15] G. Hao, M. Taniguchi, and S. Tamari, N.and Inoue. Enhanced wall-plug efficiency in AlGaN-based deep-ultraviolet light-emitting diodes with uniform current spreading p-electrode structures. *Journal of Physics D: Applied Physics*, 49(23):235101, 2016.

[16] E. F. Schubert. *Light-Emitting Diodes*. Cambridge University Press, 2006.

[17] S. Rajbhandari, J. J. D McKendry, J. Herrnsdorf, H. Chun, G. Faulkner, H. Haas, I. M. Watson, D. O'Brien, and M. D. Dawson. A review of gallium nitride LEDs for multi-gigabit-per-second visible light data communications. *Semiconductor Science and Technology*, 32(2):023001, 2017.

[18] Thorlabs. APD 430x operation Manual. `http://www.thorlabs.com/drawings/90bcb90dcbbce65d-E6B5D51A-F5C5-66C3-DE56D698D3E3D2D6/APD430A2_M-Manual.pdf`.

[19] R. P. Green, J. J. D. McKendry, D. Massoubre, E. Gu, M. D. Dawson, and A. E. Kelly. Modulation bandwidth studies of recombination processes in blue and green InGaN quantum well micro-light-emitting diodes. *Applied Physics Letters*, 102(9):091103, 2013.

[20] J. Cho, E. Yoon, Y. Park, W. J. Ha, and J. K. Kim. Characteristics of blue and ultraviolet light-emitting diodes with current density and temperature. *Electronic Materials Letters*, 6(2):51–53, 2010.

[21] M. Shatalov, W. Sun, A. Lunev, X. Hu, A. Dobrinsky, Y. Bilenko, J. Yang, M. Shur, R. Gaska, C. Moe, G. Garrett, and M. Wraback. AlGaN deep-ultraviolet light-emitting

diodes with external quantum efficiency above 10%. *Applied Physics Express*, 5(8):082101, 2012.

[22] J. G. Proakis. Digital communications. 1995. *McGraw-Hill, New York*.

[23] M. S. Islim, R. X. Ferreira, X. He, E. Xie, S. Videv, S. Viola, S. Watson, N. Bamiedakis, R. V. Penty, I. H. White, A. E. Kelly, E. Gu, H. Hass, and M. D. Dawson. Towards 10 Gb/s orthogonal frequency division multiplexing-based visible light communication using a GaN violet micro-LED. *Photonics Research*, 5(2):A35–A43, 2017.

Chapter 7

Conclusion and perspectives

The research work presented in this thesis focuses on the development and optimization of III-nitride μLEDs for optical communication applications in free space, including visible light communication and deep UV communication. The main work contains: (1) development, optimization and application of blue and violet series-biased μLEDs, (2) integration of individual n-electrode addressed blue μLEDs arrays with electronics for VLC, and (3) development of deep UV μLEDs and their application in free space deep UV communication.

Chapter 1 presents a general introduction and overview of LEDs, in particular, the LEDs based on III-nitride materials. As presented, the development of LEDs has achieved great success. In our daily life, high performance commercial LEDs emitting at a wide spectral range has been used for various applications. In chapter 1, the difference between intrinsic and extrinsic semiconductors were given. The p-n junction operating principles were described. Moreover, the principles of double heterostructures and quantum wells were introduced, along with their roles in increasing LED's quantum efficiency. The recombination processes were also described, including radiative and non-radiative recombination processes. The following sections were mainly focused on III-nitride materials and related LEDs. Due to the wide bandgap, III-nitride materials offer superior properties for the

development of LEDs. For example, the emission wavelength of the LEDs made from III-nitride materials ranges from deep UV to infrared. The growth and doping conditions of III-nitride LED wafer were introduced in Chapter 1. The problems created in growth and doping processes are also given in detail, such as dislocation and polarization effects. The drawbacks of commercial LEDs were addressed, followed by an introduction of μLEDLEDs. In the end, LEDs based free space optical communication was described, including VLC and deep UV communication systems.

Chapter 2 focuses on the introduction of tools and techniques that were used for the fabrication and characterization of III-nitride μLEDs. The fabrication processes of III-nitride μLEDs contained three main steps, which are pattern definition, pattern transfer and formation of metal contacts. Photolithography technique was introduced, which was used for pattern definition. For pattern transfer, dry (plasma) etching was used. The mechanisms of dry (plasma) etching and related facilities were presented, along with the recipes used for the etching processes in different materials. For the formation of metal contacts, metal deposition and thermal annealing are the important processes. The working principles and tools of these techniques are introduced. In the following sections, the characterization techniques of μLEDs were described, including the techniques for the characterizations of electroluminescence (EL) spectrum, electrical and optical properties, and modulation bandwidth.

Chapter 3 presents the free space optical communication systems developed in this work. The setup of a free space optical communication system is introduced first. The difference between a PIN photodiode detector and an APD detector were described, along with a brief introduction of the operation principle of an APD detector. In order to understand the relationship between optical power, modulation bandwidth and data transmission rate, Shannon-Hartley theorem was introduced. A brief description of three different modulation schemes is also given,

i.e. OOK, PAM, and OFDM modulation schemes. The advantages and disadvantages of each modulation scheme are addressed.

Chapter 4 focuses on the development of blue and violet series-biased μLEDs and their applications in free space VLC application. The design and fabrication process of the series-biased μLEDs are given in detail. As presented, the series-biased μLEDs in both wavelengths showed high optical power and electrical modulation bandwidth.The reasons behind enhanced performance on these μLEDs were explained by using the normalized wall plug efficiencies of them. In VLC application, a 11.74 Gbps data transmission rate was achieved at the FEC level of 3.8×10^{-3} by using a blue series-biased μLED array under OFDM modulation scheme at 0.3 m data transmission distance. By further extended the data transmission distance to 10 m, a 6.58 Gbps data transmission rate was achieved at the FEC level of 3.8×10^{-3}. Meanwhile, an over 12 and 6 Gbps data transmission rates were achieved at the FEC level of 3.8×10^{-3} by using violet series-biased μLED under OFDM modulation scheme at 0.3 m and 10 m data transmission distances, respectively. These results demonstrated the huge potentials of the series-biased μLEDs for high speed VLC in long distance.

Chapter 5 presents the development, performance and application of the III-nitride μLED array with individually addressable n-electrodes. The design and fabrication processes of these μLED arrays were given in detail. In order to improve the μLED array yield and the electrical and optical uniformities on the whole array, a plasma ashing step was introduced into the fabrication processes. A significantly improved μLED array yield and uniformity were achieved after applied this plasma ashing step. Then, a custom NMOS driver was introduced. In this driver, the operating current of each driver channel is up to 255 mA and the 3-dB electrical modulation bandwidth of each driver channel is 250 MHz. The fabricated μLED array was then integrated with the NMOS driver for further VLC application. The VLC performance of the integrated devices was demonstrated with 1 and 4 μLEDs operating under OOK modulation scheme. At a data transmission distance of 50

cm, the data transmission rates for single and four μLEDs were 300 Mbps and 180 Mbps without observable bit error.

Chapter 6 presents the development of novel III-nitride based deep UV μLEDs for deep UV communications. Due to the intrinsic property of deep UV light, the deep UV communication offered not only a highly secured communication link between satellites upon atmosphere, but also a low background noise non-line-of-sight communication link at the ground level. In this work, novel UV-C μLEDs were demonstrated with outstanding performances. Each UV-C μLED could be driven under high DC current densities with superior 3-dB electrical modulation bandwidth performances. A free space deep UV communication system was established using the UV-C μLED as a light source. A record of 3.36 Gbps data transmission rate at the FEC level of 3.8×10^{-3} is achieved using UV-C μLED under OFDM modulation scheme. Such high data transmission rates showed the great potential of μLEDs for deep UV communications.

7.1 Further work

There are two future research topics that can be followed according to work developed in this thesis. The first one is to further improve the thermal management of the μLEDs developed in this work. The second one is to reduce the turn-on voltage of the deep UV μLED to improve its performance in deep UV communication application.

7.1.1 Thermal management

As introduced in chapters 4, 5 and 6, all the μLEDs used in this work are bare chips, which do not have any heat sink. As a result, the performances of these μLEDs are influenced by the heat created by themselves. In order to overcome this issue, a heat sink can be introduced. However, as all the μLEDs used in this work

is at flip-chip configuration, the common commercial heat sinks are not able to be applied to these μLEDs. Therefore, it is necessary to develop a method to manage the thermal influences of these μLEDs. There are two possible approaches that can be investigated. The first one is to develop a heat sink that can be applied to flip-chip μLEDs. Since the μLEDs are at flip-chip configuration, the GaN side of the μLEDs needs to be connected with power supplier, and cannot bond with any hear sink. Therefore, the heat sink for these μLEDs can only be applied on the sapphire substrate. However, since most of light of the flip-chip μLEDs is emitting from the sapphire substrate, it is relatively difficult to apply the heat sink on the sapphire substrate of the μLEDs without sacrificing some emitted light. The second approach is to fully isolate the μLEDs using insulation thin films, and then place the devices into water or other liquids to cool the μLEDs. The difficulty of this approach is to find suitable insulation thin films, which need to have high transparency and good thermal conductivity.

7.1.2 Reducing the turn-on voltage of the deep UV μLEDs

As presented in Chapter 6, the turn-on voltage of the UV-C μLEDs fabricated in this work is high. This high turn-on voltage is due to the formation of Schottky contacts and high contact resistance. In order to reduce the turn-on voltage, a new n-type metal contact needs to be investigated along with a redesigned fabrication process flow. Ti/Al/Ti/Au metal layer is a strong candidate for the new n-type metal contact of UV-C LEDs. Based on the reference, this metal layer needs to be annealed at a very high temperature. However, the p-type metal contact (Pd) would be degraded if the annealing temperature is too high. Thus, the fabrication process flow of the UV-C μLEDs needs to be redesigned. The n-type metal contact layer needs to be deposited and annealed before depositing and annealing the p-type contact layer. It is expected that the performance of UV-C μLEDs will be greatly enhanced by reducing their turn on voltage.

List of publications

Journals

[1] E. Xie, R. Bian, X. He, M. S. Islim, C. Chen, J. J. D. McKendry, E. Gu, H. Haas, and M. D. Dawson, *Over 10 Gbps VLC for long-Distance application Using a GaN-Based Series-Biased Micro-LED Array*, IEEE photonics Technology Letters **32** (9), 499-502 (2020) [Co-first author]

[2] E. Xie, X. He, M. S. Islim, A. A. Purwita, J. J. D. Mckendry, E. Gu, H. Haas, and M. D. Dawson, *High-speed visible light communication based on a III-nitride series-biased micro-LED array*, IEEE Journal of Lightwave Technology **37** (4), 1180-1186 (2019) [Co-first author]

[3] X. He, E. Xie, M. S. Islim, A. A. Purwita, J. J. D. McKendry, E. Gu, H. Haas, and M. D. Dawson, *1 Gbps Free-Space deep-ultraviolet communications based on III-nitride micro-LEDs emitting at 262 nm*, Photonics Research **7** (7), B41-B47 (2019)

[4] E. Xie, M. Stonehouse, R. Ferreira, J. J. D. McKendry, J. Herrnsdorf, X. He, S. Rajbhandari, H. Chun, A. V. Jalajakumari, O. Almer and et al., *Design fabrication and application of GaN-Based micro-LED arrays with individual addressing by N-electrodes*, IEEE Photonics Journal **9** (6), 1-11 (2017)

[5] M. S. Islim, R. Ferreira, X. He, E. Xie, S. Videv, S. Viola, S. Watson, N. Bamiedakis, R. V. Penty, I. H. White, and et al., *Towards 10 Gb/s OFDM-based visible light communication using a GaN violet micro-LED*, Optics Express **5** (2), A35-A43 (2017) [Co-first author]

[6] G.N Arvanitakis, R. Bian, J. J. D. Mckendry, C. Chen, E. Xie, X. He, G. Yang, M. S. Islim, A. A. Purwita, E. Gu, H. Haas, and M. D. Dawson, *Gb/s underwater wireless optical communications using series-connected GaN micro-LED arrays*, IEEE Photonics Journal **12** (2), 1-10 (2020)

Conferences

(Presenters are underlined)

[7] D. M. Maclure, J. J. D. Mckendry, J. Herrnsdorf, X. He, E. Xie, E. Gu, and Martin D. Dawson, *Size-dependent characterisation of deep UV micro-light-emitting diodes* (oral), IEEE Photonics Conference, 2020, Canada

[8] X. He, E. Xie, M. S. Islim, A. A. Purwita, J. J. D. McKendry, E. Gu, H. Haas, and M. D. Dawson, *Deep UV micro-LED arrays for optical communications* (oral), The UK Nitrides Consortium winter meeting, 2019, United Kingdom

[9] X. He, E. Xie, M. S. Islim, A. A. Purwita, J. J. D. McKendry, E. Gu, H. Haas, and M. D. Dawson, *1 Gbps free-space deep ultraviolet communications based on III-nitride micro-LEDs emitting at 262 nm* (oral), The International Conference on UV LED technologies & applications, 2018, Germany

[10] E. Xie, M. Stonehouse, R. Ferreira, J. J. D. McKendry, J. Herrnsdorf, X. He, S. Rajbhandari, H. Chun, A. V. Jalajakumari, O. Almer and et al., *Design fabrication and application of GaN-Based micro-LED arrays with individual addressing by N-electrodes*, (oral), The UK Nitrides Consortium winter meeting, 2018, United Kingdom

[11] X. He, E. Xie, M. S. Islim, M. Stonehouse, S. Videv, Jonathan J. D. McKendry, I. M. Watson, Erdan Gu, H. Haas and Martin D. Dawson, *GaN-based series micro-light emitting diode arrays for visible light communication* (poster), UK Nitrides Consortium, 2018, United Kingdom